POLITECNICO DI TORINO

Dipartimento di Ingegneria Meccanica e Aerospaziale

Master's Degree in Biomedical Engineering

Master's Degree Thesis

Realization and Validation of a Wearable Prototype for sEMG-based Facial Expressions Recognition

Supervisors
Prof. Danilo DEMARCHI
Ph.D. Fabio ROSSI
M.Sc. Andrea MONGARDI

Candidate
Letizia CANTORE

Torino, March 2024

Abstract

Facial expressions form a rich communication code, enabling the conveyance of emotions and intentions. Their classification has garnered increasing attention in research, as it has yielded promising results in various applications, such as psychological state assessment, control of human-machine interfaces, and rehabilitation of facial muscle impairments.
Facial Expression Recognition (FER) can be performed through several techniques. The approach based on the surface ElectroMyoGraphic (sEMG) signal, distinct from the more commonly used computer vision strategies, offers direct insights into muscle activity, holding great potential for rehabilitative and diagnostic purposes. Preliminary studies, from a research team's prior thesis work, have shown high average accuracy in real-time recognition of 11 facial expressions, thanks to the implementation of an Artificial Neural Network (ANN). The classifier receives 5 inputs corresponding to the Average Threshold Crossing (ATC) parameter, which is computed for the selected muscles and is proportional to their activation.
This thesis project has aimed to propose an evolution of the previous prototype by implementing a low-consumption, battery-powered wearable system, inspired by the acquisition devices developed by the research team. The initial phase of the work focused on conducting preliminary tests to assess two primary aspects. Firstly, it involved testing various configurations of gold-coated dry electrodes to find a setup that offered an optimal balance between electrode size and signal quality, which is crucial for achieving high classification accuracy. Secondly, it included evaluating the most appropriate amplification levels for the programmable gain amplifier integrated into the system. The core of the work involved the realization of two Printed Circuit Boards (PCBs): one for active probes, intended to be placed directly on the skin in correspondence of the selected 5 facial muscles, and the other for a main board, integrated into a mechanical support and worn on the head. The active probes were realized with a rigid-flex stack-up and provide initial conditioning of the sEMG signal, which is acquired by the gold-coated electrodes. The main PCB, which is based on the AmbiqMicro Apollo3 Blue microcontroller, was designed to include further signal conditioning, power management, and serial communication circuits, as well as a Flash memory and an Inertial Measurement

Unit (IMU), for further research applications. Subsequently, the mechanical support, a key element to ensure the wearability of the system, was designed and 3D printed, to offer a good fit for different subjects, while ensuring proper allocation for the main PCB, the battery, and all the system components. Finally, the work has focused on adapting firmware and software for user-friendly system operation, allowing visualization of sEMG signals, ATC values, and expression prediction.
The evaluation of the sEMG Signal to Noise Ratio (SNR), acquired from facial muscles, yielded an average value of 25 dB. Ultimately, the performance of the classifier was assessed, showing average accuracy exceeding 90% in the classification of 11 facial expressions. These results reinforce the prototype's suitability for future rehabilitative applications leveraging biofeedback and serious games for facial muscle impairment treatment.

Acknowledgements

Un grazie a Danilo Demarchi per avermi dato l'opportunità di intraprendere questo progetto di tesi e ai miei supervisori, Fabio Rossi e Andrea Mongardi, per tutto ciò che ho imparato con loro.

Grazie anche agli amici di sempre, ai compagni del corso di biomedica e a quelli del laboratorio Hardware, per essere stati una parte importante di questo percorso.

Un pensiero va a Simone e alla mia famiglia, per il loro sostegno e amore costanti. Grazie di cuore per avermi sempre sostenuto in questa avventura.

Contents

List of Figures

List of Tables

Chapter 1

Introduction

1.1 Musculoskeletal system

The skeletal and muscular systems together form the musculoskeletal system, which serves as the foundation for both mechanical and metabolical functionality. It comprises bones, muscles, cartilage, tendons, ligaments, joints, and other connective tissues, that support and bind tissues and organs together. From a muscular perspective, three types of muscles can be distinguished: skeletal muscles, responsible for voluntary movements and posture; smooth muscles, which compose the walls of internal organs and vessels, managing involuntary movements; and cardiac muscles, found exclusively in the heart, pumping blood through involuntary contractions. This system not only enables movement and allows to maintain posture, but also safeguards internal organs, with bones protecting vital structures and serving as stores for minerals and blood cell production sites. Skeletal muscles are also fundamental in energy storage and metabolism, converting glycogen to energy, and aiding in heat generation, crucial for maintaining body temperature [1].

1.1.1 Skeletal Muscles Anatomy

Skeletal muscles enable voluntary movements by connecting to the skeleton through tendons, which transmit the generated force necessary to allow movement. Voluntary striated muscles are uniquely characterized by their capacity for conscious control, setting them apart from cardiac and smooth muscles. The architecture of skeletal muscles features multiple layers, starting from the macroscopic level where muscles attach to bones via tendons, descending into the microscopic realm of muscle fibers and sarcomeres, as illustrated in Figure 1.1.

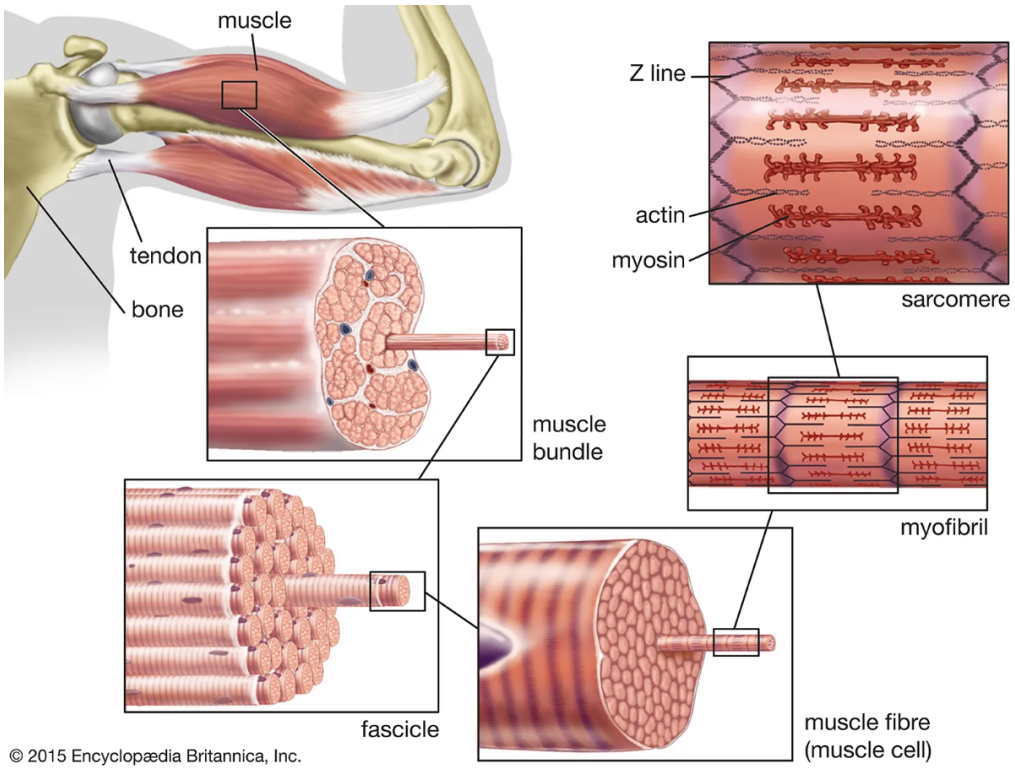

Figure 1.1. Skeletal muscle anatomy [2].

The structural hierarchy begins with muscle fascicles, bundles of muscle fibers encased by the epimysium, a connective tissue membrane linking the entire muscle to tendons (Figure 1.1). Fascicles are further divided by the perimysium, which surrounds individual muscle fibers protected by the endomysium. This innermost layer provides essential nutrients and extracellular fluid for the fibers, each containing multinucleated cells, sarcolemma, and sarcoplasm. The sarcoplasm is rich in mitochondria, responsible for converting substances from the circulatory system into Adenosine TriPhosphate (ATP), fueling muscle contraction [4]. At the core of muscle fibers are myofibrils, constituted by serially-arreanged sarcomers, that consist of thick and thin filaments made of myosin and actin proteins, respectively. These filaments, as shown in Figure 1.2, are organized into five distinct zones crucial for muscle contraction:

- M-line: It is located at the center of the sarcomere and serves as an anchoring site for thick filaments. The M-line contains proteins that hold the thick filaments together, ensuring they are properly aligned during muscle contraction and relaxation.
- H-zone: This area is located within the A-band and consists exclusively of thick filaments. The H-zone becomes narrower during muscle contraction because

the thin filaments slide past the thick filaments, reducing the region where only thick filaments are present.

- A-band: This region spans the length of the thick filaments and includes areas where thick and thin filaments overlap. The A-band does not change its length during muscle contraction; Instead, it is the sliding of the thin filaments along the thick filaments that facilitates contraction.

- I-band: This region contains only thin filaments and is located on either side of the Z-line. The I-band shortens during muscle contraction, reflecting the sliding filament mechanism where thin filaments move towards the sarcomere's center, thus shortening the sarcomere itself.

- Z-line: This structure marks the boundary between adjacent sarcomeres. It is the attachment point for thin filaments and is crucial for maintaining the alignment of the sarcomere's structural components. During muscle contraction, Z-lines move closer together as sarcomeres shorten, contributing to muscle fiber shortening and thus muscle contraction [3].

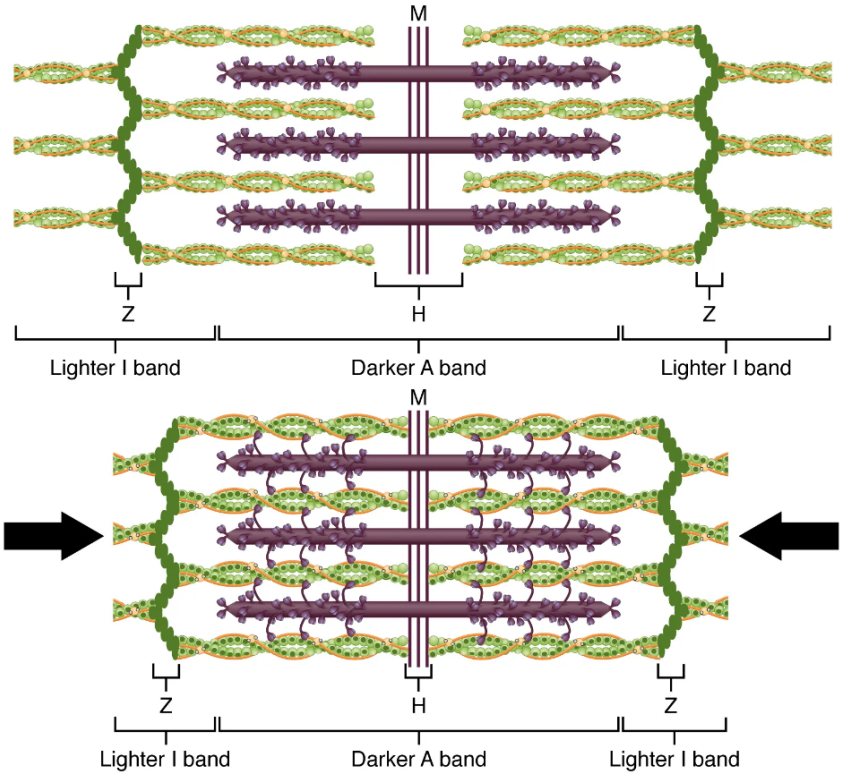

Figure 1.2. Skeletal muscle contraction mechanism mediated by Actin-Myosin complex [5].

1.1.2 Skeletal Muscles Contraction Mechanism

As described earlier, thick and thin filaments slide past each other during contraction, causing the sarcomere, and thus the muscle, to shorten and generate force (Figure 1.2). This process is enabled by ATP hydrolysis, transforming chemical energy into mechanical energy. The sarcoplasmic reticulum, surrounding myofibrils, acts as a calcium ion reservoir, essential for activating muscle contraction. The precise alternation of light and dark bands within myofibrils, observed as sarcomeres contract, highlights the complexity of muscular structure and function [1, 3, 4]. The maximum strength a muscle unit can exert is influenced by the average cross-sectional area of its muscle fibers, the force produced by these fibers, and the count of nerve connections. Among these factors, the quantity of fibers within the muscle unit plays the most important role [8].
Muscular contraction is orchestrated through a complex interaction between the Central Nervous System (CNS), motor neurons, and muscle fibers. The basic functional unit of the neuromuscular system is the motor unit, which is made up of a motor neuron and the muscle fibers it innervates. The process begins in the CNS, where signals are sent to motor neurons located in the spinal cord or brain stem. The activation of these neurons results in the generation of action potentials, which propagate along the axon to the neuromuscular junctions, the interfaces between the nerve terminals and muscle fibers. At the neuromuscular junction, the arrival of an action potential triggers the release of the neurotransmitter acetylcholine into the synaptic cleft. Acetylcholine binds to receptors on the sarcolemma (muscle fiber membrane), leading to the opening of sodium ion channels. This influx of sodium ions causes a rapid depolarization of the sarcolemma, up to 30 mV generating an action potential that spreads along the muscle fiber and through its T-tubules. This electrical signal triggers the release of calcium ions from the sarcoplasmic reticulum into the sarcoplasm. The increase in sarcoplasmic calcium concentration is the key to muscle contraction. Calcium ions bind to troponin, causing a conformational change that moves tropomyosin away from actin's binding sites, allowing actin and myosin filaments to interact [9]. This interaction, powered by ATP hydrolysis, results in the sliding of actin over myosin filaments, producing muscle contraction. When the stimulus ends, acetylcholine release ceases, the sarcoplasmic reticulum reabsorbs calcium ions, and the muscle fiber relaxes, returning to its resting state at -70mV. The entire process is highly regulated, ensuring precise control over muscle contraction and relaxation necessary for movement and force generation [11].

1.1.3 Head and Neck Muscles

The muscles of the head and neck play a key role in a wide range of vital functions, including structural support, sensory perception, and movement, such as facial expressions, swallowing, and speech. Knowledge of their anatomy, along with the physiology outlined above, is critical to accurately determine the proper placement of electrodes to record their activation and to interpret the results.

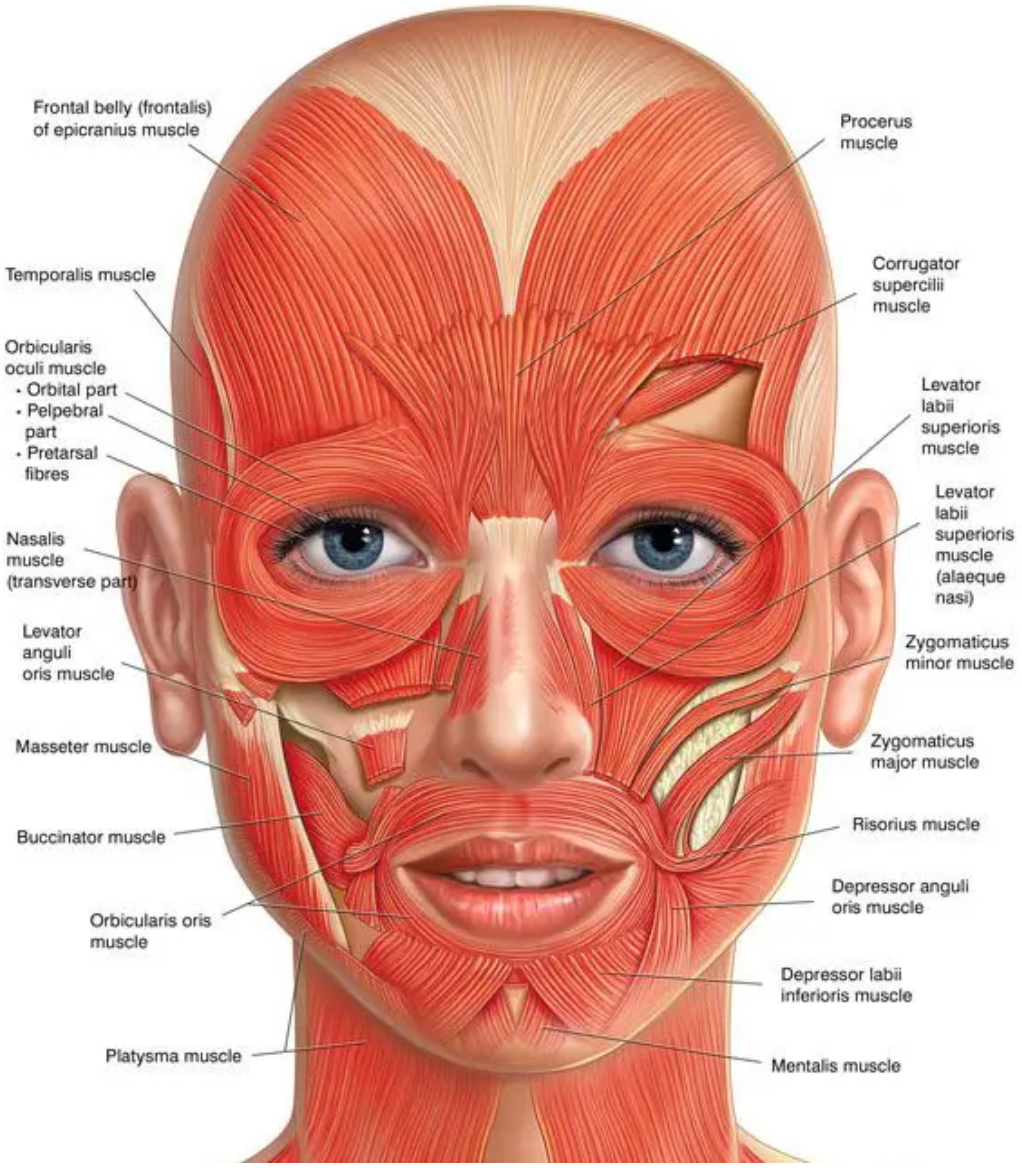

Figure 1.3. Representation of Facial Muscles Anatomy [12].

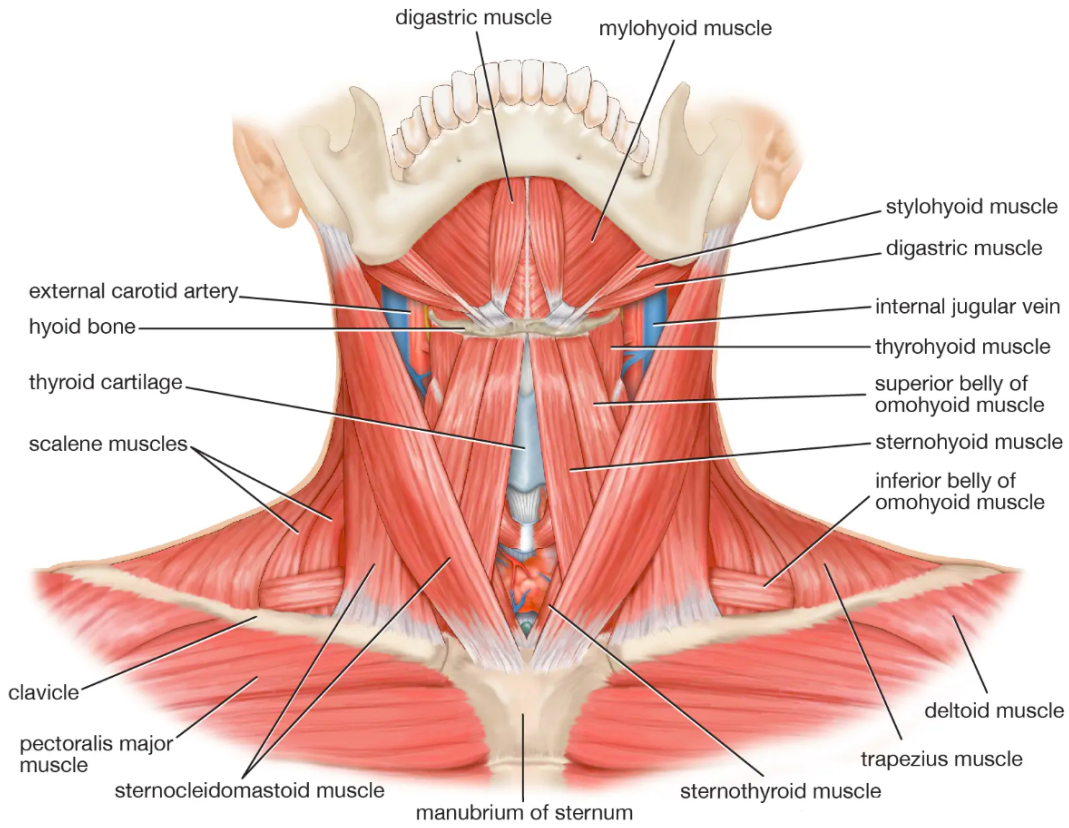

Figure 1.4. Representation of Neck Muscles Anatomy, adapted from [13].

Facial Muscles, also known as mimic or mimetic muscles, are largely innervated by the facial nerve and insert directly into the skin, unlike most other skeletal muscles. Their functions primarily involve conveying emotions through facial expressions and facilitating non-verbal communication [7]. In the subsequent pages, a concise description of the muscles pertinent to this thesis is provided, complemented by Figure 1.3, which offers a comprehensive visual overview.

- The **Zygomaticus**, consisting of the *Zygomaticus Major* and *Zygomaticus Minor*, originates from the zygomatic bone and runs obliquely to the mouth corner. It contributes to elevating the corners of the mouth upwards and outwards, forming dynamic wrinkles in the cheek and nasolabial area. Functionally, the *Zygomaticus Major* pulls the mouth into a smiling expression, while the *Zygomaticus Minor* deepens the nasolabial groove, as seen in expressions of sadness [6, 7].
- The **Corrugator Supercilii** has a small pyramidal shape. It originates from the medial end of the eyebrow arch and inserts above the mid-region of the

orbital arch. It moves the eyebrows inferiorly and medially towards the nose and inner corner of the eye in a frowning expression, forming vertical wrinkles on the forehead[6, 7].

- The **Frontalis** has a broad and fan-like shape. It originates from the connective tissue covering the top of the skull, spans across the frontal bone, and extends from the eyebrows to the hairline. Functionally, it elevates the eyebrows, creating horizontal wrinkles on the forehead and producing a wide-eyed expression, indicative of surprise or interest. Conversely, relaxation of the *Frontalis* muscle allows the eyebrows to descend, contributing to a more neutral or relaxed facial appearance [6, 7].

TemporoMandibular Joint (TMJ) muscles play a crucial role in the movement and functionality of the mandible, the lower movable bone of the jaw. Together, they enable a wide range of jaw movements, including lowering, protrusion, retrusion, and lateral motion. These actions allow the execution of crucial functions, such as chewing, speaking, swallowing, and even maintaining head and neck posture [7]. Below it is provided a brief introduction to the TMJ muscles relevant to this thesis project:

- The **Masseter** is a paired rectangular-shaped muscle. It originates from the zygomatic process of the maxilla and the zygomatic arch, respectively, and inserts into the mandible. This muscle plays a crucial role in the masticatory system, supporting the articular capsule of the temporomandibular joint. It also contributes to the closing, clenching, elevation, and protrusion of the mandible for speaking, biting, or chewing [6, 7].

- The **Digastric** originates from the lower edge of the mandible near the symphysis and inserts onto the intermediate tendon of the hyoid bone, in the neck region (Figure 1.4). It's a paired muscle, consisting of two bellies: the anterior one elevates the hyoid bone, while the posterior belly opens the jaw by pulling the mandible downwards. It coordinates with other jaw muscles, playing a pivotal role in the execution of the complex movements required for speaking, chewing, swallowing, and facilitating the passage of food through the digestive system [7, 13].

1.1.4 Facial Expressions

Facial expressions play a critical role in social interactions, serving as a universal language for communicating emotions and intentions. They facilitate empathy, help establish rapport, and contribute to the interpretation of spoken language, fostering deeper connections between individuals. In addition to their social significance, facial expressions also serve practical functions, such as protecting the eyes and mouth from potential harm, aiding in chewing and digestion, and regulating airflow during breathing. In Table 1.1, the facial expressions relevant to this thesis work are listed, along with their associated muscular activations.

Table 1.1. Facial Expressions and relative muscular activations [7].

Facial Expression	**Activated Muscles**
Smile	*Zygomaticus, Orbicularis Oris, Mentalis, Depressor Anguli Oris, Depressor Labii, Masseter*
Side Smile	*Zygomaticus, Orbicularis Oris, Mentalis, Depressor Anguli Oris, Depressor Labii, Masseter* (only on the activated side)
Clench teeth	*Masseter, Temporalis, Pterygoid, Frontalis, Stylohyoid*
Open Jaw [a]	*Digastric, Mylohyoid, Pterygoid*
Raised eyebrows	*Frontalis, Orbicularis Oculi*
Frown	*Corrugator Supercilii, Orbicularis Oculi*
Closed eyes	*Orbicularis Oculi, Retractor Bulbi, Levator Palpebrae Superioris, Frontalis*
"Pursuing lips [u]"	*Orbicularis Oris, Buccinator, Risorius*
Eye Blink	*Orbicularis Oculi, Frontalis, Corrugator Supercilii, Zygomaticus, Levator Labii Superioris* (when the "Blink" is forced or exaggerated)

1.2 Surface Electromyography

Surface electromyography is a non-invasive methodology for capturing electrical signals from muscles, by placing electrodes on the skin directly above the targeted muscle area. This technique enables the detection of the sEMG signal, which

reflects the electrical activity occurring when muscle fibers' membranes, specifically the sarcolemma, undergo depolarization [1, 8].

1.2.1 sEMG Signal

Muscles are composed of numerous motor units activated by motor unit action potentials (MUAPs). These MUAPs travel to the neuromuscular junctions of muscle cells, prompting a depolarization that spreads to the ends of the muscle fibers. The creation of the sEMG signal comes from the combined effect of these electrical phenomena, which can either reinforce or cancel each other out, enabling depolarization waves to exhibit either bi-phasic or tri-phasic patterns. The overall signal captured encompasses the collective action potentials of motor units within the observed area [8, 17].

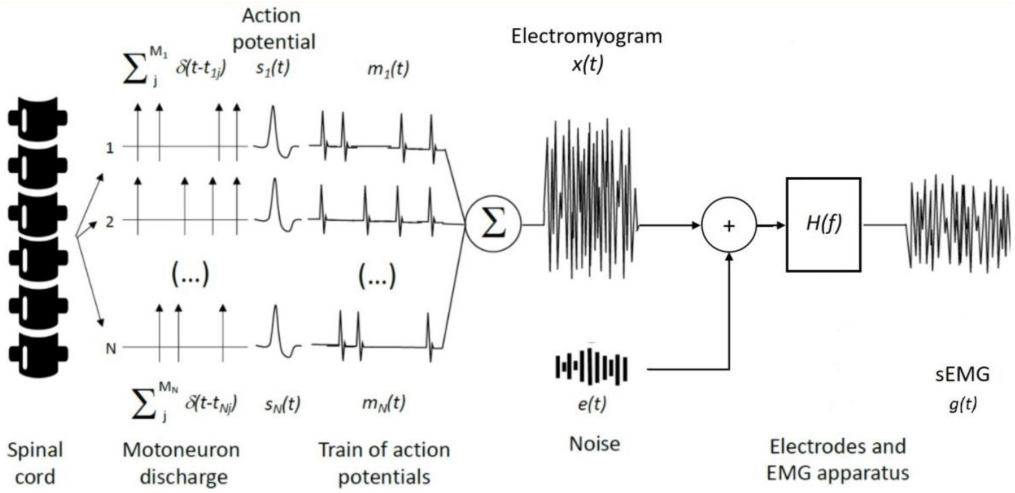

Figure 1.5. Representation of the generation of sEMG signal from motor unit action potentials summation process [14].

The sEMG signal's peak-to-peak amplitude can reach up to 10 mV, while its frequency range extends from 0 to 500 Hz, yet, the most significant energy concentration lies within the 50 to 150 Hz spectrum [15, 16]. The limitation of surface electromyography is its inability to isolate and analyze individual MUAPs due to the high number of MU present in the acquisition volume, a task more suited to the intramuscular technique. However, the sEMG signal is invaluable in examining muscle activation and nerve function, making it particularly suited for diagnostics, rehabilitation, and functional replacement [17].

1.2.2 Noise Sources

Considering the significantly low amplitude of the sEMG signal, it is imperative to consider all potential sources of noise that could corrupt the signal to prevent the loss of its informational content [8, 16]. The main sources of noise to be considered are listed below:

- **Electrode-Skin Interface and Electrode Surface Quality:** Poor electrode condition and the non-conductive nature of skin can result in high and inhomogeneous contact impedance, which can significantly affect signal conduction. Clean and intact electrodes must be properly applied to clean skin to ensure optimal signal acquisition.
- **Internal Body Noise:** The body tissues between the muscle of interest and the electrodes can interfere with the propagation of the sEMG signal due to capacitive effects and dispersive phenomena, reducing the amplitude of the acquired signal.
- **Motion Artifacts**: Subject movement or displacement of the electrode cables can introduce low-frequency interference. This can be mitigated by properly designing the acquisition circuit with a high-pass filter and minimizing cable movement.
- **Crosstalk**: Signal interference may be recorded due to the electrical activity originating from adjacent muscles. It can be reduced by decreasing the distance between the exploring electrodes, which narrows the sampling volume and increases the acquisition specificity.
- **ECG Artifacts**: The electrocardiographic (ECG) signal can be involuntarily acquired. The spectral overlap with the sEMG signal complicates its removal. Strategies for reducing ECG contamination include, for instance, the implementation of a differential amplifier with a high CMRR (Common Mode Rejection Ratio) in the signal conditioning chain.
- **Electromagnetic Noise**: The human body can act as an antenna for environmental electromagnetic noise. In particular, one of the most problematic sources is the power line, which has an amplitude that can easily overshadow that of the sEMG signal, and whose frequency (50Hz in Europe and 60Hz in the USA) overlaps with the signal's frequency band. To mitigate this interference, several precautions must be taken, such as striving to reduce and balance the impedance of the exploring electrodes, for instance, using active probes, and minimizing the imbalance of parasitic capacitance of cables by twisting them. Incorporating a differential amplifier with a high CMRR into the conditioning chain is also advisable to decrease the common mode's contribution to the output signal relative to the differential signal. Additionally, considering

the inclusion of hardware or software filters that do not impact the signal's useful bandwidth is recommended.

1.2.3 Acquisition Electrodes

Biopotential electrodes act as transducers, transforming ion distribution on the surface of the probed tissue into electrons, through electrochemical reactions. The electrode-electrolyte interface, which is a key factor in understanding the electrical behavior of electrodes, can be modeled as represented in Figure 1.6, where:

- E_{hc} is the electrode half-cell potential;
- R_s represents the total series resistance, encompassing all forms of resistive behavior, including those related to the solution, the material comprising the electrode, and the external circuit;
- R_d symbolizes the diffusion resistance, describing the current leakage across the double layer, which forms when an electrode is immersed in an electrolytic solution;
- C_d denotes the diffusion capacitance, corresponding to the capacitance across the same double layer.

At lower frequencies, the electrode-electrolyte interface impedance exhibits a predominantly resistive nature, converging towards $R_s + R_d$ as the frequency approaches 0 Hz. In the intermediate frequency range, which is the one of interest for biopotentials acquisition, the impedance behavior of the electrodes becomes frequency dependent, emphasizing the importance of the electrode material. For instance, Silver - Silver Chloride (Ag/AgCl) electrodes typically exhibit a lower R_d and a higher C_d compared to Gold electrodes, reflecting their more efficient charge transfer and better electrochemical stability at the interface. At higher frequencies, electrode impedance stabilizes and is predominantly influenced by R_s [27, 8].

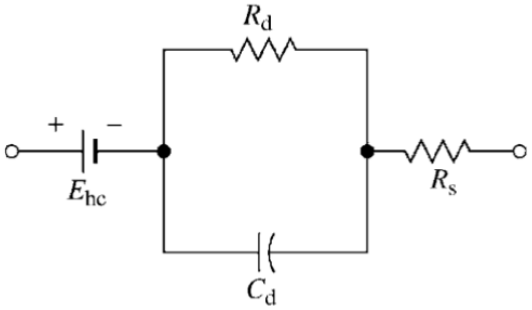

Figure 1.6. Equivalent electrical model of biopotential acquisition electrodes [27].

Considering the information provided above, the selection of electrodes for biopotential acquisition must take into account the electrochemical properties of the material used. Other crucial factors to consider include biocompatibility and the stability of the electrode-skin contact, which must be optimal to ensure high-quality signal recordings [27].

Wet-gel, Dry and Capacitive electrodes

- **Wet-gel electrodes**, known for their excellent signal quality, low skin contact impedance, and affordability, are the preferred choice in clinical health monitoring settings. Typically made of highly conductive silver interfaced with silver chloride and a gel rich in silver chloride ions, these electrodes offer the lowest and most stable junction potential. The gel's adhesive nature ensures the electrode remains securely attached to the skin, minimizing motion artifacts and signal distortion. However, wet electrodes come with notable drawbacks. Their shelf life is limited, and they are best suited for short-term biopotential monitoring, due to the potential dehydration of the gel that can degrade signal quality over time. Additionally, the use of Ag/AgCl electrodes can cause skin irritation or itchiness in some individuals. These limitations have driven research toward finding alternative electrodes, to address the challenges posed by wet electrodes [21, 22]. The electrical model is provided in Figure 1.7 (a).

- **Dry electrodes** offer a convenient alternative to wet-gel electrodes, particularly for extended monitoring and scenarios where gel application is impractical. They eliminate the need for gel, simplifying application and reducing setup time. Although they show higher contact impedance and are more susceptible to motion artifacts compared to wet-gel electrodes, they tend to improve after a settling period, outperforming capacitive electrodes in terms of artifact reduction over time. Therefore, their employment necessitates an input stage with extraordinarily high input impedance to guarantee the acquisition of high-quality biopotential signals [21, 22, 25]. The electrical model is provided in Figure 1.7 (b).

- **Capacitive electrodes** provide a novel approach compared to conventional wet and dry electrodes, which act as transducers by converting ionic current in tissue into electron flow in metal and require meticulous skin preparation to minimize impedance and noise. In contrast, capacitive electrodes use a conductive plate covered by a dielectric material to detect electrical displacement currents, thereby eliminating the need for skin preparation and conductive gels. This makes them advantageous for long-term monitoring and applications where skin preparation is impractical. Capacitive electrodes replace the

series resistance in the electrode-skin model with a coupling capacitance, significantly affecting signal quality through variations in electrode capacitance caused by movement, which requires sophisticated front-end electronics design to minimize artifacts. Advancements in front-end amplifier design, including high input impedance and techniques like neutralization and power supply bootstrapping, have improved their performance. Furthermore, appropriate shielding and design considerations allow insulating electrodes to achieve reduced interference and movement artifacts, positioning them between dry and wet electrodes in terms of artifact levels. Their evolving design makes them increasingly viable for a range of applications, potentially offering a balance between the low maintenance of dry electrodes and the signal quality of wet electrodes [8, 21, 22]. The electrical model is provided in Figure 1.7 (c).

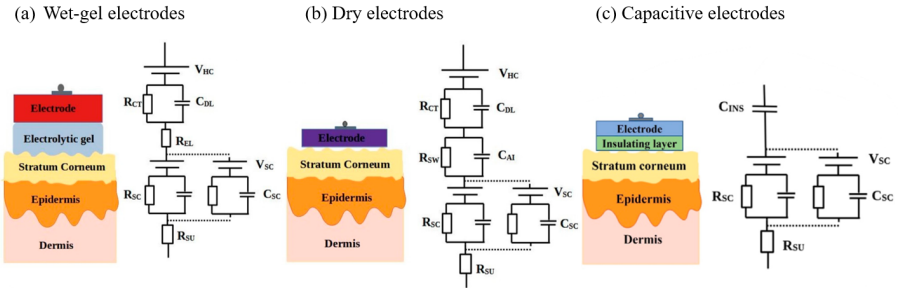

Figure 1.7. Representation of Wet-gel (a), Dry (b) and Capacitive (c) electrodes equivalent electrical models, adapted from [22]. Referring to Figure 1.6, within this figure, C_{DL} is equivalent to C_d, R_{CT} matches R_d, R_{EL} corresponds to R_s and V_{SC} to E_{hc}. C_{SC} is the capacitance of the insulating stratum corneum. Additional leakage resistance, R_{SC}, accounts for the effect of hair follicles, sweat glands, and pores within the stratum corneum. The subcutaneous layers beneath exhibit a conductive resistance R_{SU}. R_{SW} represents the resistance from the sweat layer, and C_{AI} quantifies the strong capacitive component due to the gap between the electrode and the skin.

Active electrodes

Active probes are favored for their ability to amplify signals directly at the measurement site, leading to improved signal quality. These features make them particularly valuable in clinical and research settings where signal fidelity is crucial. Active electrodes incorporate voltage followers, amplifiers with unity gain, that receive as input the signal picked up by the exploring electrodes.
The inclusion of these components has two main effects:

- Increase in input resistance, seen by the electrodes looking towards the acquisition system, which is crucial for minimizing the attenuation due to the effect of the acquisition front-end on the recorded signal.

- Decrease in output resistance, seen by the acquisition system looking towards the electrodes, which allows for minimizing common-mode and differential noise due to electrode resistance. This characteristic is especially beneficial when using electrodes with high electrode resistance, such as in the case of the Gold ones.

For this reason, they exhibit lower susceptibility to electromagnetic interference, offer reduced motion artifacts, and allow for the use of longer cables without signal degradation. Active electrodes also require less skin preparation and can integrate signal conditioning components such as filters to further enhance signal quality. However, active electrodes are more expensive than their passive counterparts and necessitate a power source, leading to greater complexity and a higher risk of damage. Moreover, their electronic components might make them bulkier, possibly interfering with natural movements. Despite these drawbacks, the effective noise reduction offered by active electrodes makes them an appealing option for detecting low amplitude muscle activations [27].

1.2.4 Detection system parameters influencing sEMG signal features

The acquisition system, characterized by the interaction between the electrodes and the tissues on which they are placed, is influenced by several variables that affect the recorded signal in different ways [27, 8]. Below it is provided a list of the main features to consider:

- **Thickness of the subcutaneous tissue layer:** The signal amplitude decreases and the bandwidth narrows as the thickness increases, acting as a spatial low-pass filter. This filtering effect is due to the additional layer the electrical signal must traverse, attenuating higher frequencies more than lower ones.
- **Depth of the muscle:** Signals originating from muscle sources that are deeper or more distant from the electrodes are attenuated, leading to a reduction in their amplitude.
- **Detection system and muscle fiber orientation:** The angle between the electrodes and the muscle fibers affects the captured signal's properties. The effect is multifaceted, influenced by the electrode's spatial filter, size, and shape, and can lead to variations in signal amplitude and frequency content. Optimal signal quality is achieved by aligning the electrodes with the direction of the muscle fibers.
- **Length of the muscle fibers:** Fiber length impacts the amplitude of the signal, particularly the end-of-fiber components, that arise when the propagating MUAPs reach the fiber end and progressively overlap. Short fibers result

in larger end-of-fiber potentials compared to the propagating signals, affecting the overall signal characteristics captured by the electrodes.

- **Location of the electrodes:** Electrodes placement is crucial for accurate signal capture. Locations between the innervation zone and the tendon are optimal for bipolar derivations, as this positioning minimizes the bias towards high frequencies and low amplitude values in the spectral features of the sEMG signal.

- **Inter-Electrode Distance (IED):** The IED, which represents the distance between the centers of the exploring electrodes, directly affects the spatial resolution, amplitude, and frequency content of the sEMG signal (Figure 1.8). A shorter IED can enhance the specificity of the signal by focusing on a smaller area of muscle activity, leading to higher spatial resolution. This configuration is particularly beneficial when targeting specific muscles or muscle parts, as it helps to reduce the crosstalk from adjacent muscles. Furthermore, a smaller IED can act as a high-pass filter, emphasizing higher frequency components of the sEMG signal. This is because the smaller detection area is more sensitive to the rapid changes in potential caused by nearby muscle fiber action potentials.
  Conversely, a larger IED can capture signals from a wider area, potentially including multiple muscle groups or deeper muscle layers, providing an increased sensitivity in the recording of muscle activity.
  Adjusting the IED allows researchers and clinicians to tailor the sEMG measurement to the specific needs of their study or diagnostic assessment, balancing between specificity, amplitude, and the depth of muscle activity being monitored.

- **Electrode size:** The size of electrodes used in surface electromyography significantly influences the signal's quality and characteristics. Larger electrodes collect signals from a broader area of muscle fibers, leading to increased sensitivity and a low-pass filtering effect (Figure 1.8). Conversely, smaller electrodes provide higher spatial resolution, allowing for more precise detection of muscle activity from a specific area, but may also capture less overall signal, which can be a disadvantage in detecting low-amplitude muscle activities. Furthermore, the electrode size directly influences its impedance, smaller electrodes have higher electrode impedance, which can lead to higher sensitivity to noise.

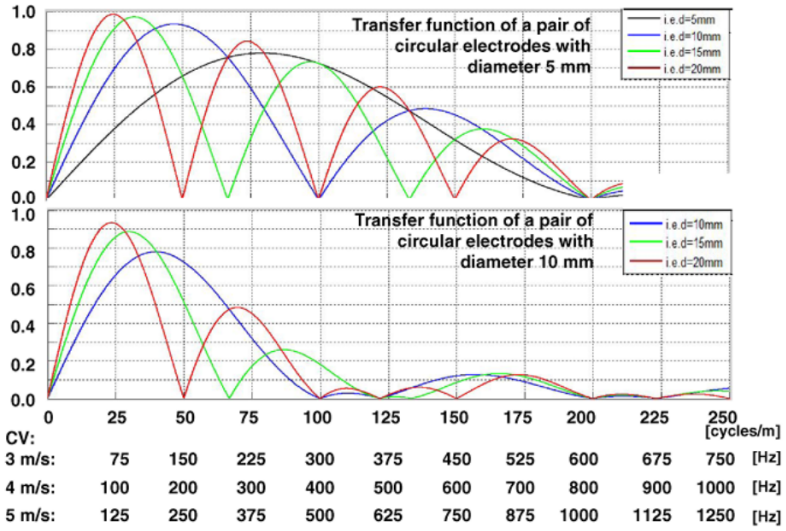

Figure 1.8. The graph depicts the transfer function for a bipolar recording using two round electrodes with different spacing between them and diameters of 5 mm (top graph) and 10 mm (bottom graph). The x-axis displays the spatial frequency (measured in cycles per meter) and translates it into the equivalent temporal frequency for three distinct muscle conduction velocities. The initial decrease observed in the transfer function is directly related to the inverse of the distance between the electrodes [8].

1.2.5 Acquisition techniques

Various methods can be employed in surface electromyography for capturing muscle activity, including monopolar, bipolar, and multipolar techniques, each offering unique advantages and disadvantages [23].

- **Monopolar technique:** This method, characterized by its simple setup, involves detecting the sEMG signal using a single recording electrode in conjunction with a reference electrode, placed far from the target muscle. Its primary downside is the heightened sensitivity to electromagnetic noise, which could compromise the signal quality by including unwanted interference [23].

- **Bipolar Technique:** This technique, on the other hand, employs two recording electrodes positioned directly over the muscle of interest, supplemented by a third reference electrode. This setup benefits from the use of a differential amplifier that amplifies the difference in signals between the two recording electrodes, relative to the reference electrode. The key advantage here is the effective elimination of electromagnetic noise, which enhances the clarity of the sEMG signals from the targeted muscle. Nevertheless, this method comes with the drawback of potentially missing out on certain sEMG signal information

due to the common mode rejection, which might eliminate parts of the signal along with the noise. Moreover, bipolar recordings introduce the concept of spatial filtering, which enhances the system's selectivity by focusing on the electrical activities of muscle fibers closer to the surface and diminishing those from deeper within the muscle, thus offering a more refined analysis of muscle activity albeit with reduced contributions from deeper muscle fibers [23].

- **Multipolar technique:** This method requires the use of several electrodes to produce a multitude of sEMG signals, surpassing the limited spatial resolution of traditional monopolar and bipolar configurations and thus providing a more detailed mapping of muscle activation [24].

The choice among these sEMG acquisition methods depends on the specific application needs, such as the desired precision in muscle activation studies, the activity's dynamic nature, or the practicality and simplicity required for certain situations.

1.2.6 Signal conditioning chain

To accurately capture sEMG signals, biopotential acquisition circuits integrate several critical components, each fulfilling a specific function within the system. At the forefront, safety precautions ensure that both patients and sensitive electrical components are not exposed to dangerous current flows. Subsequently, a differential high-pass filter is employed to filter out frequencies below the sEMG signal band, like those from motion artifacts. The core of a biopotential acquisition system lies in the differential amplifier, which provides an initial signal amplification. Usually, an Instrumentation Amplifier (INA) is implemented, as not only subtracts the two input signals to mitigate common mode interference but also maintains high input impedance, avoiding distortion at the electrode-skin interface. The CMRR of this amplifier is crucial, with acceptable values higher than 100 dB, ensuring that noise and unwanted signals are effectively suppressed. A low-pass filter is inserted to trim away any high-frequency interference that surpasses the sEMG signal bandwidth. Subsequent amplification stages boost the low-amplitude signals to a level appropriate for the analog-to-digital converter (ADC), the final element in the acquisition chain, responsible for converting the analog signals into digital form.
Through this arrangement, the chain provides acceptable signal amplitude and selectively acquires the necessary bandwidth of biopotential information [27].

1.3 Average Threshold Crossing Technique

Estimating muscle contraction force through the acquisition and processing of the analog sEMG signal entails high computational costs, due to the required digitalization via ADC. In addition, sEMG-based gesture recognition applications require additional processing to perform feature extraction. This affects power consumption and transmission performance, limiting the implementation of low-power and real-time technologies, such as wearable devices. To address these problems, Crepaldi et al. [18] introduced the ATC technique, which works by generating an event whenever the signal exceeds a defined threshold, obtaining the quasi-digital Threshold-Crossing (TC) signal. The count of these events is subsequently averaged over a time window (set to 130 ms, as it resulted being the best trade-off between the need to distinguish different magnitudes of muscle activation and a satisfactory temporal resolution of the acquisition [19]). This approach reduces power consumption through lower throughput (Figure 1.9) and a decreased computational cost for processing the ATC parameter, compared to the sEMG signal. A crucial aspect of obtaining ATC values representative of muscle activity is to set an appropriate threshold, which is provided as input to the voltage comparator along with the sEMG signal. The computed threshold should be high enough to prevent the generation of unexpected events, due to environmental noise, yet low enough to detect even low levels of muscle activation, to ensure information integrity.

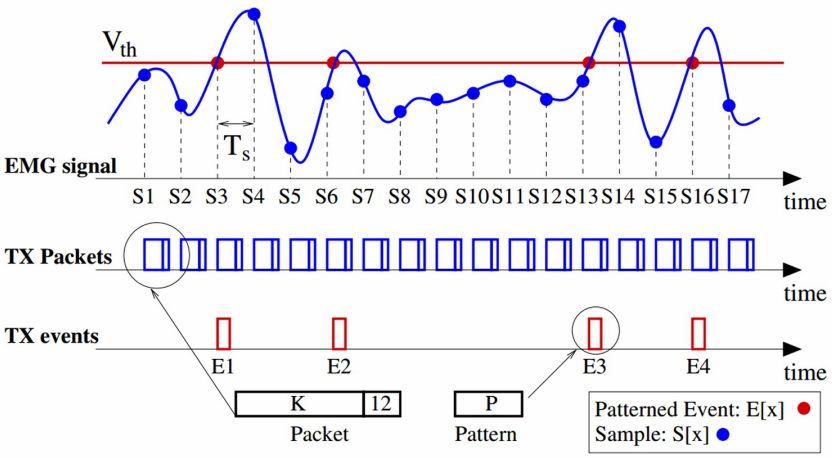

Figure 1.9. Representation of Average Threshold Crossing technique [18].

1.4 Bluetooth Low Energy (BLE)

This section briefly describes the main features of the Bluetooth Low Energy (BLE) protocol implemented for the wireless communication of the prototype. BLE is a low-energy wireless technology ideal for short-range control and monitoring, striking a balance between energy efficiency and latency. BLE architecture (Figure 1.10) is segmented into three main layers: Application, Host, and Controller. The Application layer encompasses the user interface and operational logic of BLE devices. Below it, the Host contains protocols like the Logical Link Control and Adaptation Protocol (L2CAP), Security Manager Protocol (SMP), and the Generic Attribute Profile (GATT), facilitating communication and data management. The Controller layer manages the physical and link layers, ensuring efficient wireless communication [31].

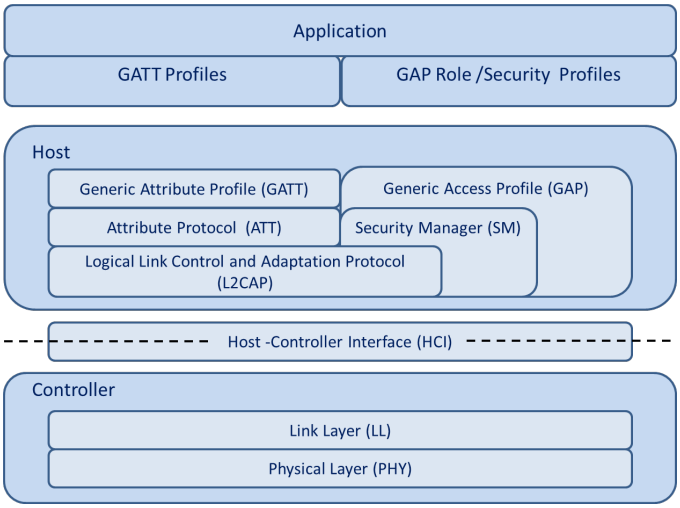

Figure 1.10. BLE protocol stack [33].

Focusing specifically on the GATT within the Host layer, it plays a crucial role in BLE communication by defining how a server (device offering data) exposes data to a client (device requesting data). In GATT terminology, data is organized into Services and Characteristics. Services are collections of information or functionalities that a device offers. Characteristics within a service provide specific information or functionalities. Each characteristic consists of a value and may also contain descriptors that provide additional metadata about the characteristic, such as its measurement units, callback presence, or access permissions for the characteristic, which can be therefore: readable (allowing clients to read their values); writable (permitting clients to modify values); notifiable (clients receive updates whenever the server alters a characteristic's value).

1.5 Classification algorithms and metrics

1.5.1 Algorithms

This section presents a concise introduction to some of the main techniques used to perform sEMG-based FER, setting the stage for an in-depth exploration in the upcoming chapters.

Linear Discriminant Analysis (LDA)

LDA is a supervised machine learning that aims to reduce data dimensionality, enhancing the optimization of machine learning models by separating classes with multiple features. LDA models the data distribution per class, employing Bayes' theorem to classify new data points based on conditional probabilities. The most informative linear combination of the features is determined, to project multi-dimensional data into a singular dimension for simpler class separation, as depicted in Figure 1.11. Unlike logistic regression, which is confined to binary classification, LDA's versatility allows it to tackle multi-class data classification tasks. LDA is praised for its simplicity, computational efficiency, and ability to handle high-dimensional data, retaining crucial information. However, LDA struggles to linearly separate classes that have similar statistical properties. Moreover, LDA's utility is limited to supervised learning scenarios where data is labeled [34].

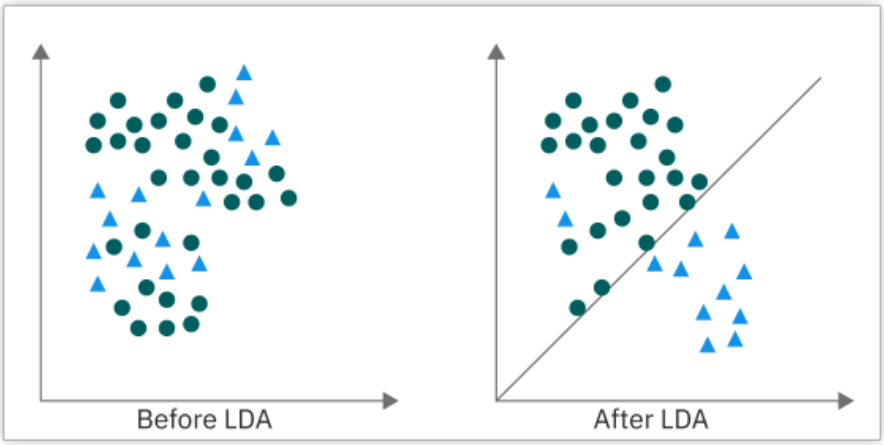

Figure 1.11. Representation of LDA technique [34].

Random Forest algorithm (RF)

The RF model, a collection of numerous decision trees (Figure 1.12), effectively tackles both regression and classification challenges by aggregating individual tree predictions. Indeed, a key feature of RF is its use of ensemble learning, where the ensemble is formed by a collection of decision trees, each trained on a random subset of the training data. For regression tasks, the model averages the predictions from each tree, while for classification, it employs a majority voting system. This approach enhances overall predictive performance, mitigates the issue of overfitting, and allows the straightforward assessment of significant features. Conversely, the model's downsides are its processing time due to the complexity of managing multiple trees, the demand for increased computational power, and the greater difficulty in interpreting the ensemble output, compared to that of a singular decision tree [36].

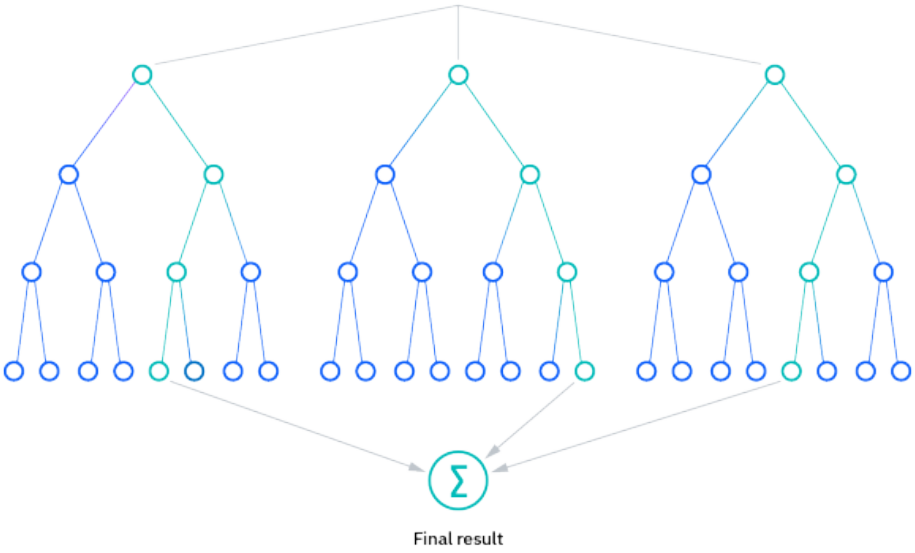

Figure 1.12. Representation of RF Alogrithm [36].

Artificial Neural Network (ANN)

The ANN is a supervised learning algorithm inspired by biological neural networks. It is made up of several nodes, or artificial neurons, organized in an input layer, one or more hidden layers, and an output layer (Figure 1.13). Each artificial neuron has an associated weight, which is the key feature of the learning process. The output of each neuron, which is computed as the weighted sum of the inputs and a bias, is then passed through an activation function. The role of the activation functions is to introduce non-linearity to the network, enabling it to learn complex patterns in the data. There are several types of activation functions:

- **Sigmoid:** Outputs a value between 0 and 1, making it useful for models where a probability represents the output.

- **Rectifier Linear Unit (ReLU):** Outputs the input directly if it is positive, otherwise, it outputs zero. It has become the default activation function for many types of neural networks because it helps with the vanishing gradient problem.

- **Tanh:** Outputs values between -1 and 1, offering a better range than the sigmoid function, which can help with training convergence.

- **Softmax:** It is suitable for output layers in classifiers with multiple categories. It returns a probability distribution computed by taking the exponential of each output and then normalizing these values by dividing by the sum of all the exponentials.

Any individual neuron, whose output exceeds a specified threshold, is activated, sending data to the next layer of the network. Learning in an ANN occurs through the process of adjusting the weights of the connections in the network during the training phase, typically using a method called gradient descent. Backpropagation is used to make those adjustments, calculating the gradient of the loss function with respect to each weight by the chain rule, efficiently propagating the error backward through the network [37].

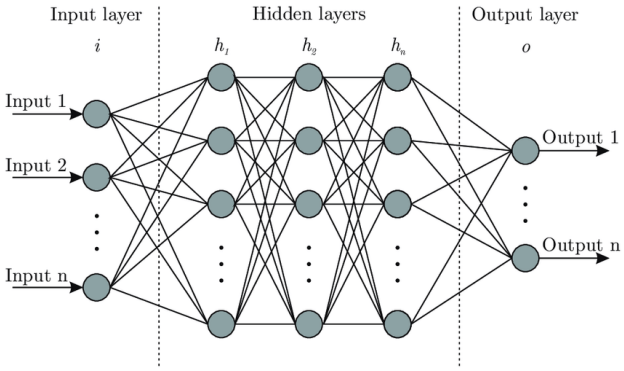

Figure 1.13. Representation of ANN architecture[38]

Convolutional Neural Network (CNN)

The CNN excels in recognizing patterns within data by applying importance to distinct features through its deep learning framework, significantly reducing the need for manual preprocessing. Inspired by the human brain's visual cortex, CNNs mimic the pattern of neuron connectivity, focusing on stimuli in a restricted visual field and overlapping these fields to cover the entire visual area. Its foundational building block, the convolutional layer, applies filters to the input through the convolution, this operation allows the detection of spatial features such as edges, enhancing the network's ability to recognize visual patterns. Following the convolutional layer, the pooling layer reduces dimensionality and computational complexity by summarizing the features detected, often through methods like max pooling. The fully connected layer then integrates these features, leveraging the high-level patterns identified by previous layers. Lastly, a Softmax activation function is applied to obtain the final classification (Figure 1.14). CNNs automatically detect important features without any human supervision, using backpropagation algorithms to minimize the error in predictions [35].

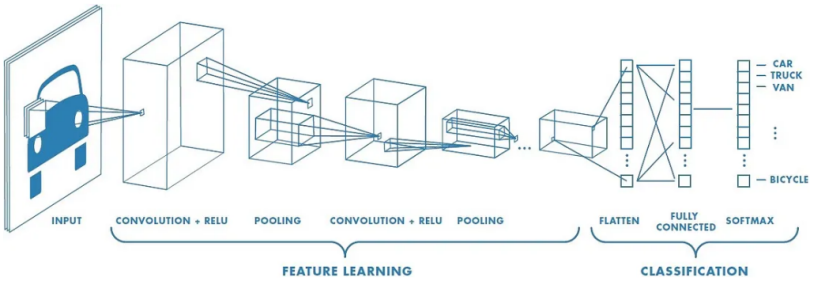

Figure 1.14. Representation of CNN architecture[35].

1.5.2 Metrics

To evaluate the effectiveness of a classification approach, employing specific metrics is crucial for quantifying predictions against actual labels, thus providing a measurable assessment of performance. In the subsequent sections, we will delve into some prominent metrics used in classification: accuracy, precision, recall, and the F1 score, which are based on the following concepts:

- True Positive (TP): Occurs when the model correctly predicts the positive class. In other words, the actual value is positive, and the model also predicts it as positive;
- True Negative (TN): Occurs when the model correctly predicts the negative class. This means the actual value is negative, and the model accurately identifies it as negative;
- False Positive (FP): Occurs when the model incorrectly predicts the positive class. This means the actual value is negative, but the model mistakenly predicts it as positive;
- False Negative (FN): Occurs when the model incorrectly predicts the negative class. This means the actual value is positive, but the model incorrectly labels it as negative.

Now, we consider the metrics:

- Accuracy: It measures the fraction of instances that the model correctly identifies out of all instances.

$$\text{accuracy} = \frac{TP + TN}{TP + TN + FP + FN} \tag{1.1}$$

- Precision: It indicates the proportion of accurate positive identifications made by the model compared to all positive identifications it makes.

$$\text{precision} = \frac{TP}{TP + FP} \tag{1.2}$$

- Recall: This is the measure of the model's ability to identify all relevant instances correctly.

$$\text{recall} = \frac{TP}{TP + FN} \tag{1.3}$$

- F1 Score: This metric is a weighted mean of precision and recall, providing a balance between the two.

$$F1 = 2 \times \frac{\text{precision} \times \text{recall}}{\text{precision} + \text{recall}} \tag{1.4}$$

Chapter 2

State of Art

FER technologies have primarily been dominated by computer vision techniques, appreciated for their straightforward deployment, affordability, and reasonable accuracy. Given that computer-vision FER is a leading research topic with numerous studies dedicated to it, an initial classification can be made into static image FER, dynamic sequence FER, and multimodal systems [39].
Static image FER focuses on extracting emotional cues from a single frame, and analyzing facial landmarks and muscle movements to classify emotions through machine learning algorithms. In contrast, dynamic sequence FER tracks the evolution of facial expressions over time, utilizing sequential neural networks to understand emotional changes across a series of frames. Multimodal systems enhance FER by integrating visual data with auditory signals and physiological measurements, offering a comprehensive and nuanced approach to emotion recognition. This combination allows for more accurate emotion detection, especially in complex scenarios where visual cues alone may not suffice. Li et al. [39] delve into the forefront of the latest FER techniques, showcasing novel deep neural networks and their training techniques for analyzing both static and dynamic images, while pointing out their pros and cons. Indeed, despite currently being the Gold Standard for FER, computer vision faces several challenges, including variability in lighting, facial occlusions, pose variations, and diversity among subjects, which can hinder accurate expression analysis. Privacy concerns and the need for high computational resources further complicate the deployment of these FER systems, especially in real-time applications.

Emerging as a cutting-edge alternative, sEMG-based FER leverages the electrical activities within facial muscles to decode emotional states and expressions. As for computer vision, this technology faces its own set of challenges. The outcomes of sEMG-based FER are notably sensitive to the condition of facial skin, where the presence of sebum and facial hair can compromise the electrodes' proper adherence, leading to a significant decrease in prediction accuracy. Moreover, variations in signal quality can occur due to individual differences in facial muscle configuration

across individuals, affected by age, gender, and habitual expressions, which can lead to variability in signal interpretation. Despite further research being necessary to enhance the reliability and applicability of sEMG in FER, this technique holds great potential due to several advantages. In fact, sEMG-based FER shows high resilience to external environment changes, thereby offering consistent performance regardless of lighting or occlusion. sEMG technology is also less prone to errors from head movements and provides insights into minor muscle movements that are not visually observable, making it highly effective for detailed expression analysis and a valuable alternative to computer vision techniques. Addressing current limitations through ongoing research may unlock its full potential for broad and effective application in emotion analysis and non-verbal communication support [41, 42, 43].
For this reason, the following pages detail the most recent studies on sEMG-based FER. Additionally, some studies introducing new technologies for creating flexible electrodes have been examined. To make sEMG-based FER applicable, it is indeed crucial to have comfortable electrodes, that ensure prolonged adhesion and capture a high-quality signal, allowing high classification accuracy. Finally, since this work aims to develop a wearable application, an innovative wireless and low-power system, tailored for processing sEMG signals, is presented.

Ho-Seung at al. carried out a study [40], utilizing 19 wet-gel electrodes (see Figure 2.1) to capture sEMG signals in the area surrounding the eyes, to classify 11 facial expressions. They applied feature extraction to the recorded sEMG signals leveraging Riemannian manifold, a mathematical space where Euclidean geometry is defined locally around each point. Then, they preprocessed the signals by notch-filtering at 60 Hz and bandpass-filtering at 20–450 Hz using a fourth-order Butterworth filter. The processed signals were then segmented using a sliding window technique. With this setup, they achieved an average accuracy of 85.01%, which limited the system's practicality. In a subsequent work [41], the research team improved the system's FER performance by adapting the user-specific LDA model with additional LDA models, built using data from other users. This strategy enhanced the mean classification accuracy to 89.40%. They also demonstrated the potential of a training-free user-independent FER system, achieving an 82.02% accuracy rate in classifying the selected facial expressions. This novel approach of cross-subject LDA adaptation represents a significant step towards more usable sEMG-based FER systems for applications like Virtual Reality (VR). Building upon these findings, the research group advanced the sEMG-based FER technology by integrating covariate shift adaptation techniques [42], significantly enhancing system robustness against electrode displacement. In detailed evaluations, participants expressed the 11 facial expressions across four sessions, involving the removal and reapplication of the electrodes. In the previous studies, classification accuracy suffered, dropping from 88% to 79% due to electrode repositioning. However, with

the implementation of the novel adaptation method, accuracy impressively recovered to 86%, proving the method's effectiveness. This progression underscores a significant leap towards the practical deployment of sEMG-based FER systems in immersive VR metaverse applications, promising a more seamless and consistent user experience.

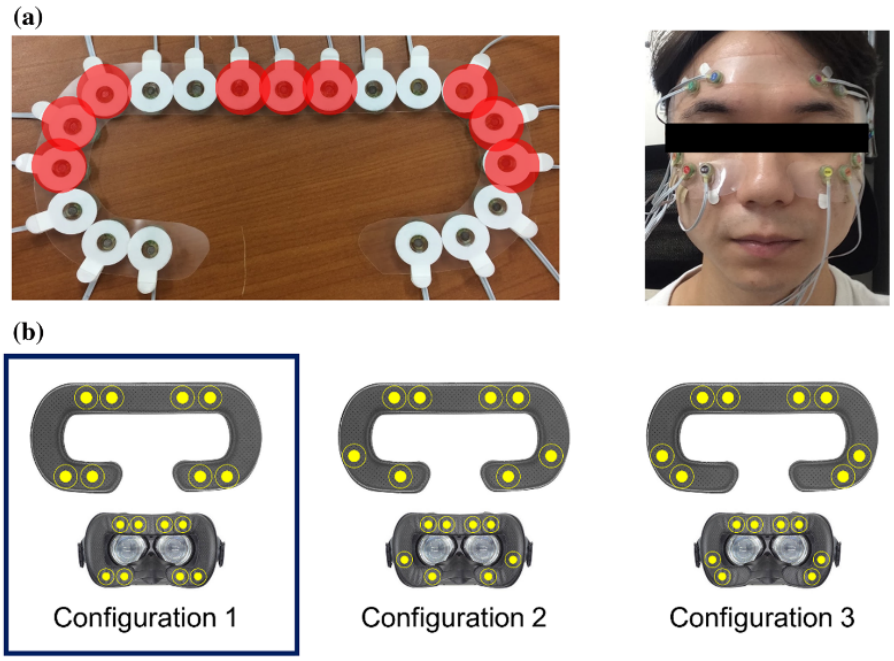

Figure 2.1. In their visual presentation, Ho-Seung et al. depicted, on the left side, a plastic film pad densely outfitted with 19 sticker electrodes. Those encircled in red were noted for their tendency to lose adhesion to the skin.

Kiprijanovska et al. evaluate a cutting-edge VR facial mask embedded with 7 sEMG bipolar sensors for tracking facial muscle dynamics and categorizing 5 distinct facial expressions [43]. The sEMG data were captured consistently at a rate of 1000 Hz and subjected to comprehensive preprocessing to perform signal denoising and filtering. They applied a Hampel filter to eliminate abrupt signal spikes caused by rapid movements. Then, to mitigate electromagnetic interference noise, notably at 50 Hz and its harmonics, a spectrum interpolation-based frequency filtering technique was implemented. Data segmentation leveraged a sliding window method, with 0.5-second windows and 0.1-second strides.
From each sEMG channel, 34 features were extracted for a total of 238 features, encompassing amplitude-based metrics, amplitude derivatives, auto-regressive and cepstral coefficients, frequency attributes, and statistical measures.
The combination of a RF algorithm with a Hidden Markov Model emerged as the

most effective machine learning strategy in their tests, showing notable versatility across the validation set. Depending on the chosen data scaling and sampling approach, accuracy ranged from 84.2% to 89.48%, with F1-Macro scores spanning 0.75 to 0.86. This comprehensive study underlines the influence of preprocessing techniques, feature selection, and machine learning algorithms on the performance of models designed for expression recognition, highlighting the complexity and potential of utilizing sEMG data within VR applications.

Figure 2.2. EmteqPRO™multi-sensor face mask employed in the study conducted by Kiprijanovska et al [43].

The cutting-edge FER system introduced by Liu et al. [44] integrates innovative epidermal electronics with flexible electrodes and artificial intelligence (AI) to achieve high-fidelity sEMG signal acquisition. This system employs a deep learning network to analyze features extracted from 10 acquisition channels, achieving an effective accuracy of expression intensity recognition of 92.51%. The system's architecture includes 10 working electrodes, alongside a reference electrode and a ground electrode. These electrodes comprise a 150 nm layer of gold (Au), a 10 nm layer of chromium (Cr), and a 1.1 μm layer of polyethylene terephthalate (PET), all encapsulated within a 47 μm thick layer of 3M Tegaderm medicine tape. This technology ensures more reliable skin contact than traditional gel electrodes, while effectively minimizing motion artifacts during skin expansion and compression. Notably, the Signal-to-Noise Ratio (SNR) of sEMG signals acquired with these flexible electrodes improves post-sweating, proving them to be a viable solution for long-term wear. The electrodes are wired to an acquisition unit that samples the recorded sEMG signals at 1000 Hz. The system then processes the signals, scaling and augmenting the input data to account for intersubject variations. The preprocessed values are

then transformed into a feature map, which serves as input to a convolutional neural network (CNN). This network calculates probabilities for each category, with the model distinguishing between 7 facial expressions and 5 intensity levels.

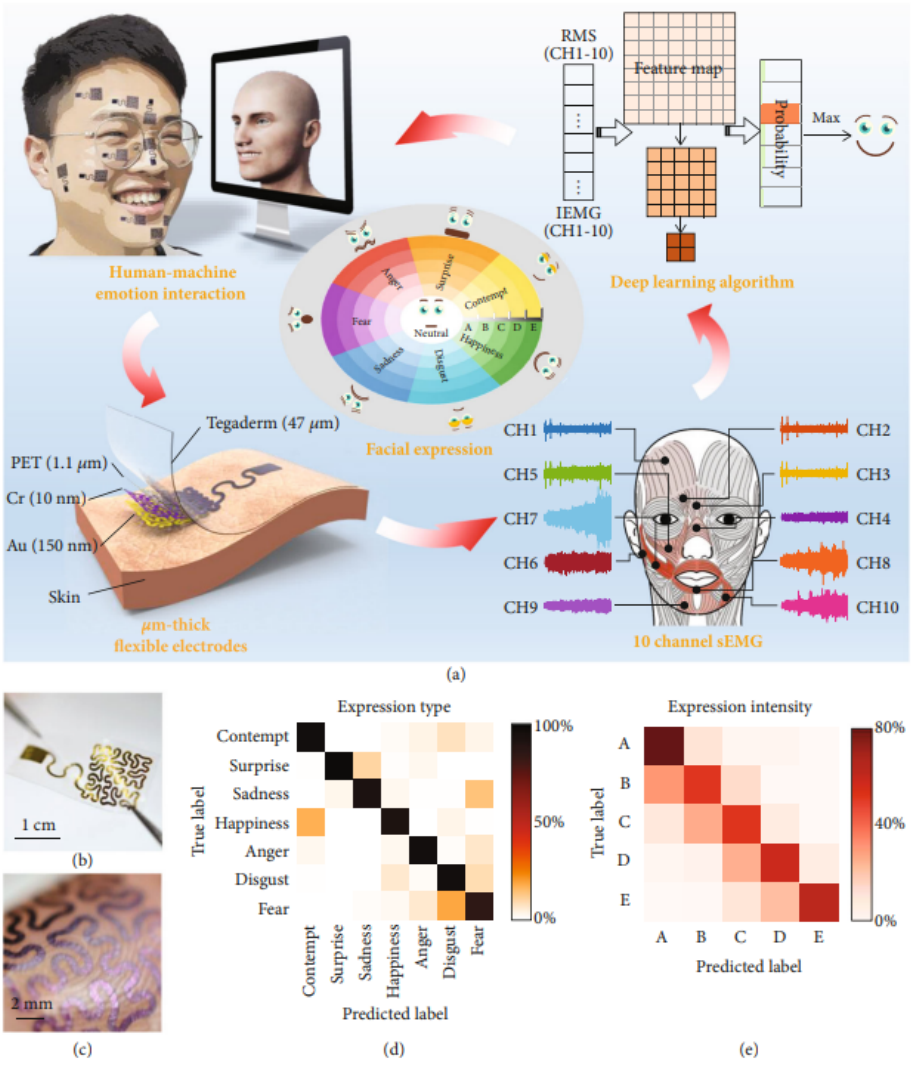

Figure 2.3. Overview of the Wearable FER System developed by Liu et al. [44]. Figure (a) illustrates the system's capability to recognize seven facial expressions, each classified into five levels of intensity. Figure (b) provides a visual depiction of a single flexible electrode and (c) its placement on the skin. Figures (d) and (e) represent the confusion matrix of 7 expression types and 5 levels of expression intensities.

The combination of time and spatial domain features during the measurement period enhances model training, yielding accuracies of 97.22% for the training set, 92.38% for the validation set, and 85.51% for the test set. This holistic approach, from electrode design to AI application, offers a nuanced and quantitative understanding of users' emotional states, surpassing traditional FER systems by eliminating constraints on movement, space, and lighting. The system's innovative use of flexible electrodes and deep learning not only supports spontaneous expression recognition but also paves the way for advanced human-computer emotional interfaces, demonstrating the potential for wide-ranging applications in daily and specialized settings.

Yeon et al. have developed a flexible electrode to address the challenges in controlling lower extremity robotic prostheses with sEMG, prioritizing comfort and manufacturability. This electrode effectively captures sEMG signals from the residual limb, even during dynamic activities, and matches the performance of traditional Ag/AgCl electrodes. Its design minimizes skin indentation, offering a significant improvement over previous solutions. The electrodes are produced using flexible PCB technology, ensuring both low-cost and easy manufacturing. The electrodes have a circular shape, 10 mm in diameter and 16 mm apart, to reduce crosstalk and enhance signal quality. Produced by PCBWay, each sensor costs less than $ 6.00 for a batch of 30, promising affordability for broader research and clinical use [45].

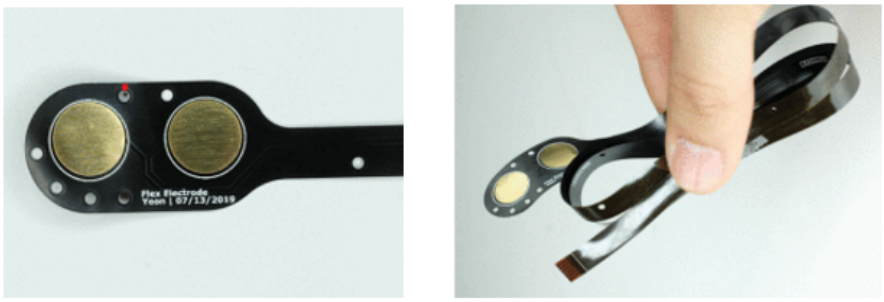

Figure 2.4. Manufactured electrode proposed by Yeon et al. (a) Close up on the electrode developed electrode. (b) Illustration of the electrode's flexibility post-production.

Despite ongoing research, no optimal trade-off has been discovered to simultaneously tackle robustness, miniaturization, versatility, and power efficiency for surface sEMG muscle monitoring. Rossi et al. have addressed this issue in a recent work [29], unveiling a sEMG ATC-based solution based on BLE 4.2 wireless connectivity,

chosen for its energy efficiency, flexibility, and broad adoption. They emphasized accurate representation of muscular activity, ensuring good signal detection amidst environmental noise, and employing a sufficiently representative digitization level. Additionally, they prioritized fast system response to input variability within real-time constraints, while also focusing on compact system dimensions, robust and accessible data streaming, and achieving sufficiently long operating time for multi-day monitoring without frequent recharges. The system integrates the AmbiqMicro Apollo3 Blue MicroController Unit selected because it can be powered at 1.8 V, key feature for low-power applications, and it is available in a 20.25 mm^2 compact package. Furthermore, it requires low current absorption of 6 $\mu A\ MHz^{-1}$ for the CPU (capable of running up to 48 MHz) and 3 mA TX power when transmitting at 0 dBm. It also features both non-volatile (e.g., Flash) and volatile (e.g., RAM) memory units, with RAM availability of 384 kB, sufficiently large to store application data, and support efficient firmware performance for edge-computing tasks, like gesture prediction. The proposed system also features a custom sEMG conditioning circuit designed to directly extract in hardware event-based signal information, such as TCs. The following pages describe the components of the developed Analog Front End (AFE) (Figure 2.5).

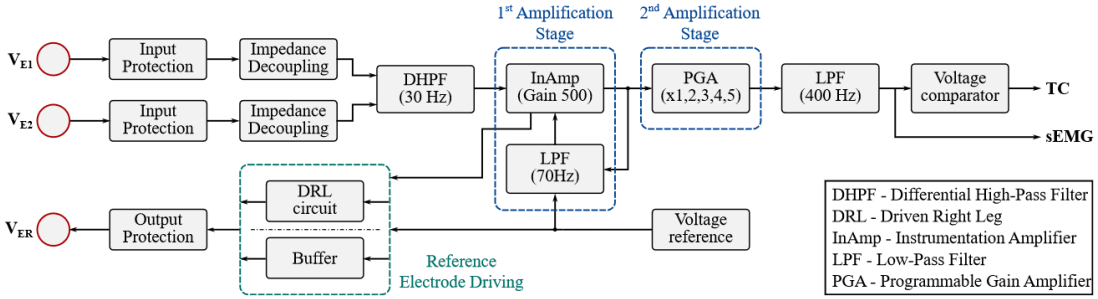

Figure 2.5. Schematic block diagram of the AFE proposed by Rossi et al. [29].

- **Input/Output Protection:** It is inserted to guard against excessive voltages above the supply level, preventing damage to circuit components. An R-D network, incorporating resistors and diodes, reduces high voltages to safer levels and diverts excess to ground, protecting downstream circuits. Ferrite beads suppress interference, while additional resistors limit currents to the ESD protection module, ensuring the integrity of the input protection system. This setup maintains controlled voltages at critical circuit points, safeguarding the device against electrical stress and enhancing durability.

- **Decoupling Circuit:** It incorporates a voltage follower for each sensing channel, positioned between input protection and signal conditioning, to match amplifier input impedance with electrode-skin impedance and preserve sEMG

signal integrity.

- **Differential High-Pass Filter (DHPF):** It is crucial for maintaining sEMG signal quality by transforming ionic flows into electrical currents at the electrode-skin interface, a process vulnerable to disturbances like movement artifacts which introduce low-frequency noise. To mitigate these effects, a DHPF was implemented before the INA, effectively filtering out frequencies below 30 Hz, chosen as an optimal balance between removing artifacts and preserving sEMG energy. Attempts to increase the cutoff frequency to 60 or 70 Hz aimed at reducing power-line interference were counterproductive, leading to the loss of sEMG content, hence maintaining the cutoff at 30 Hz. A visual representation of the implemented DHPF is provided in Figure 2.6.

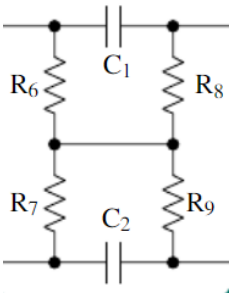

Figure 2.6. DHPF electrical model [29].

DHPF cutoff frequency:

$$f_c = \frac{1}{2\pi R_8 C_1} = \frac{1}{2\pi R_9 C_2} \tag{2.1}$$

- **INA (1st Amplification Stage):** It provides the first stage of amplification, crucial for processing bio-signals like sEMG, which require amplification to be digitally analyzed. Given the variability in muscle conditions, sEMG signals demand gains ranging from 500 V/V to 6 kV/V. The total amplification is often split across multiple stages to accommodate different muscle types and to ease the constraints on amplifier gain-bandwidth. The INA differentially amplifies the input signals, enhancing signal stability through low-pass negative feedback, and is designed to minimize common noise sources like power-line interference, thanks to its high CMRR. Utilizing the INA333 from Texas Instruments and specific resistor configurations allows for adjustable gain and effective noise management. Additionally, the system includes a negative feedback mechanism, as shown in Figure 2.7 to stabilize the output signal against low-frequency noise, with adjustments in cutoff frequency to address various

noise sources effectively, ensuring reliable sEMG signal acquisition and interpretation.

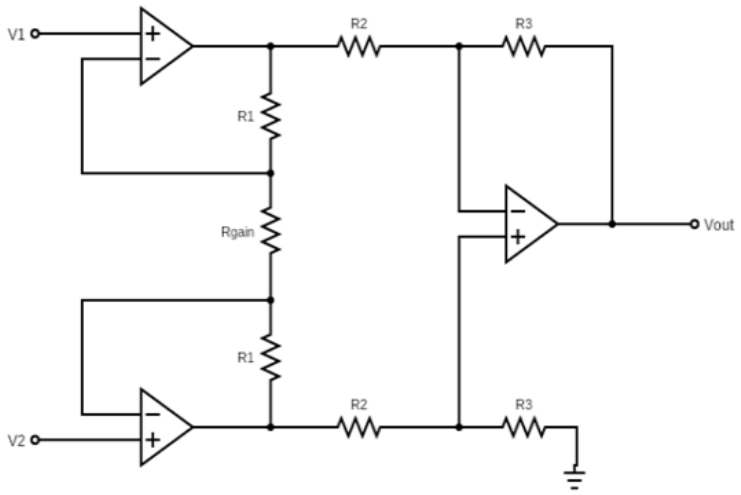

Figure 2.7. Representation of the INA electrical model.[28].

INA output voltage:

$$V_{out} = A_d \cdot (V_2 - V_1) + \frac{1}{2} A_{cm} \cdot (V_2 - V_1) \tag{2.2}$$

Differential Gain:

$$A_d = \left(1 + \frac{2R_1}{R_{gain}}\right) \cdot \frac{R_3}{R_2} \tag{2.3}$$

CMRR, where A_{cm} in the common-mode gain:

$$\text{CMRR} = 20 \cdot \log_{10} \left(\frac{|A_d|}{|A_{cm}|}\right) \tag{2.4}$$

- **Reference Electrode Driving:** There are two approaches for setting the reference electrode's voltage in bio-signal processing circuits: a simpler method that uses a voltage regulator to establish a fixed reference voltage at half the supply voltage (VDD/2), enhanced with a voltage follower for stability, and a more advanced Driven Right Leg (DRL) circuit aimed at reducing common-mode noise by inverting the common-mode voltage and feeding it back to the subject's body. Both strategies include a safety mechanism to cap the electrode current at 10 mA, blending ease of implementation with effective noise management.

- **Programmable Gain Amplifier (2nd Amplification stage):** To accommodate the amplification needs of deeper or smaller myofibers, a second amplification stage with a Programmable Gain Amplifier (PGA) offering different gain levels was developed, aiming for simplicity and user-friendly parameter control. This stage utilizes an analog multiplexer to select the gain by altering the electrical path to the operational amplifier, integrating an RC circuit as a high-pass filter to prevent baseline signal amplification. When extra gain is not required, it functions as a buffer, chosen over commercial PGAs for lower power consumption and reduced complexity.

- **Low-Pass Filter:** A Sallen-Key Low-Pass Filter, shown in Figure 2.8, is used after the amplification stages to restrict the sEMG signal bandwidth to 400 Hz, targeting the energy content primarily found between 50 Hz and 150 Hz. This filtering stage ensures that the signal is free from higher frequency interference not related to muscle activity and aligns with the designed amplification bandwidth. Additionally, serving as an anti-aliasing filter, it prepares the sEMG signal for input into an ADC.

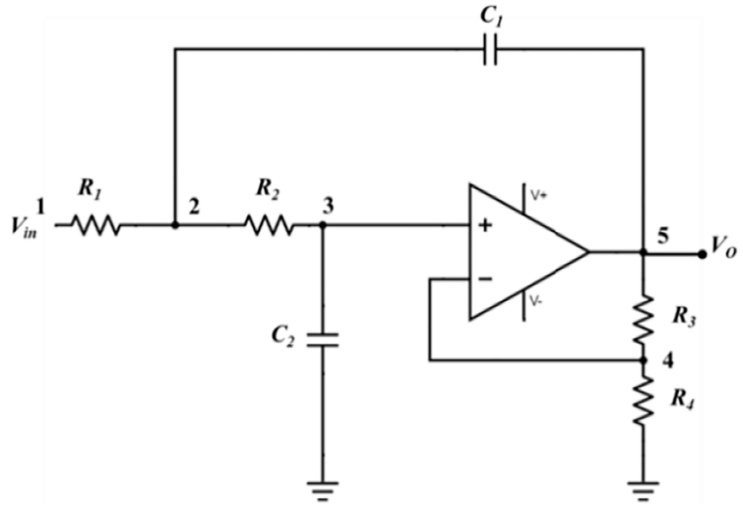

Figure 2.8. Representation of the Sallen-Key Low Pass Filter electrical model [30].

Cutoff frequency:

$$F_c = \frac{1}{2\pi\sqrt{R_1 R_2 C_1 C_2}} \tag{2.5}$$

Quality factor:

$$\mathrm{Q} = \frac{\sqrt{R_1 R_2 C_1 C_2}}{C_2(R_1 + R_2)} \tag{2.6}$$

- **Voltage Comparator and DAC:** The final stage of the Analog Front-End (AFE) incorporates a voltage comparator for extracting the TC signal, enhanced with a Digital-to-Analog Converter (DAC) to allow for adjustable threshold values tailored to various muscle activities and environmental conditions. Implementing a 30 mV hysteresis around the threshold value converts the comparator into an efficient Schmitt Trigger, mitigating spurious spikes by stabilizing the signal transmission to the MicroController Unit (MCU) dedicated input.

Central to the system's signal-processing digital unit is the previously discussed Apollo3 Blue MCU. Essential components include a UART-to-USB converter for direct computer communication, I2C connectors for network integration, a DAC for threshold calibration, and a USB-powered battery charger, emphasizing portability. The MCU processes AFE signals, facilitates BLE connectivity, and interfaces via USB or I2C. Leveraging FreeRTOS, the firmware adeptly manages ATC evaluation and Bluetooth communication, adaptable to various applications, from real-time data analysis to gesture-controlled actuations, ensuring a versatile and efficient digital framework. Setup includes peripheral configuration for ATC management and GPIO for input signals, with a focus on energy-saving timer settings. Serial ports for SPI control and AFE gain adjustment via PGA are also configured. Threshold calibration, essential for distinguishing muscle activity from noise, is performed at startup, adjusting for environmental variables and ensuring accurate signal detection amidst potential noise disturbances.
A BLE server on the Apollo3 MCU allows full device control and real-time data notifications. User interface elements include command and status characteristics for device control and feedback, and data characteristics like gain, sEMG readings, threshold settings, and ATC counts, each tailored for specific operational needs.
Simulated analysis confirmed the hardware threshold comparator's accuracy in tracking *Biceps Brachii's* static response to varying weights, with data processing revealing a direct proportionality between load and TCs, supported by a strong correlation with simulated signals. Furthermore, a power consumption analysis proved that ATC data reduction and optimized connectivity timing can save up to 80% of the sEMG energy budget, enabling approximately 230 hours of continuous transmission with a 110 mAh LiPo battery.

Inspired by this technology, the research team developed an sEMG-based FER prototype (Figure 2.9) as part of a previous thesis work [48].

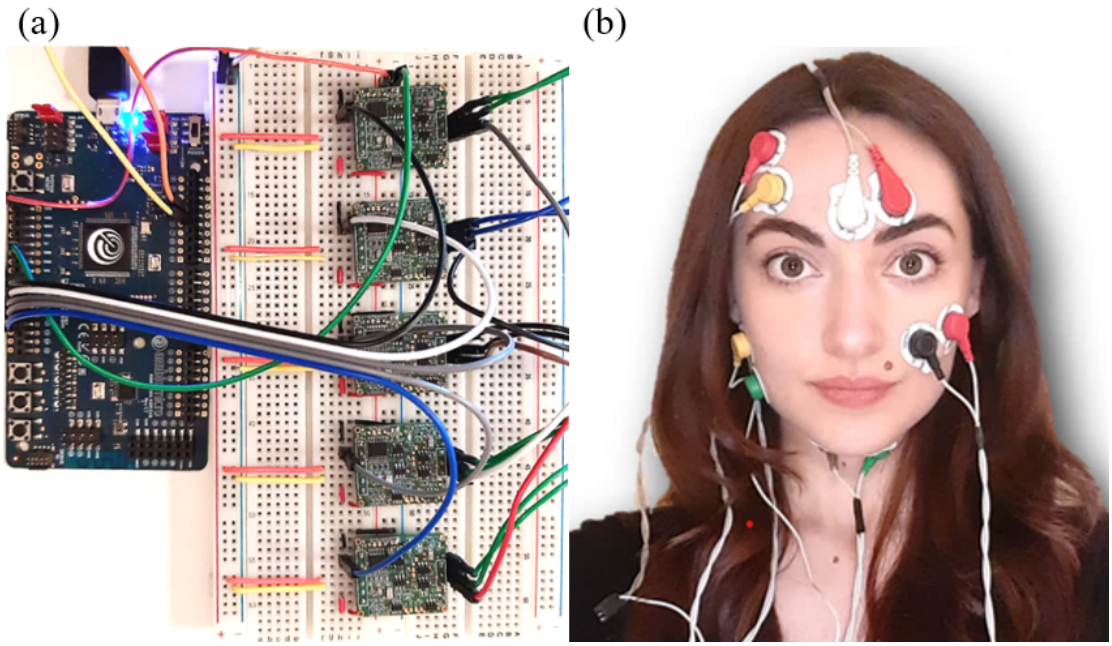

Figure 2.9. The picture shows the previously developed prototype, in particular in (a) it is illustrated the Evaluation board and the AFEs and in (b) the placement of the Ag/AgCl electrodes with the shielded fields.

It included five acquisition channels designed to capture the sEMG signals from the *Zygomaticus*, *Corrugator Supercilii*, *Frontalis*, *Masseter*, *Digastric* facial muscles. A schematic representation of the described system is shown in Figure 2.10.

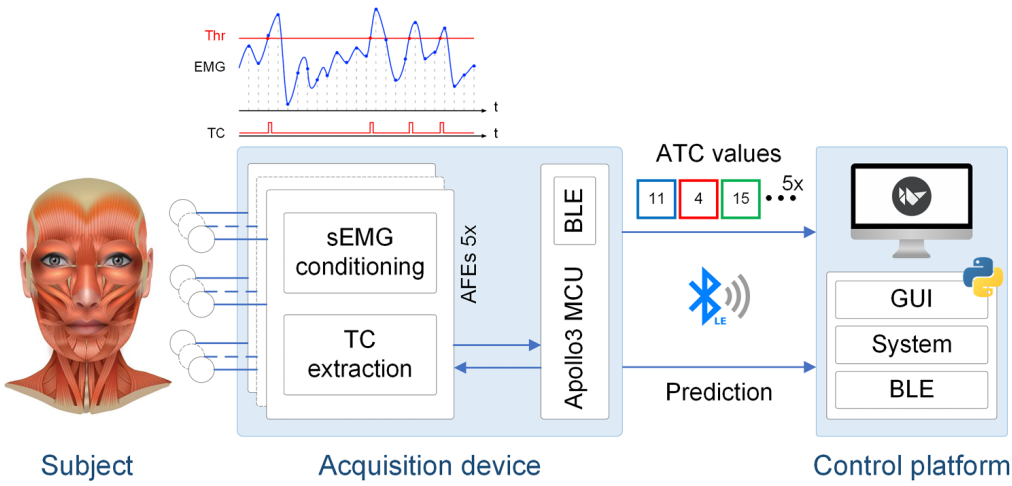

Figure 2.10. System overview of the previous prototype [48].

Each channel used a pair of exploring electrodes alongside a shared reference electrode, totaling 11 Ag/AgCl H124SG pre-gelled disposable electrodes. These electrodes were connected via shielded wires and clip heads to five AFE boards (Figure 2.11). The boards processed the TC signal through a series of signal conditioning stages:

- **Differential High Pass Filter (HPF):** Implemented as a second-order filter with a 33.86 Hz cutoff to eliminate movement artifacts.
- **INA:** The INA333 was chosen for its stable gain and high CMRR, with an adjustable gain ranging from 1 to 10,000 V/V through an external resistor, preset at 500 V/V for these boards.
- **Low Pass Filter (LPF):** Employed with a 70 Hz cutoff as negative feedback to the differential amplifier's reference voltage, reducing power-line interference.
- **Gain Selector:** A PGA allows setting the channel gain at $\times 1$, $\times 2$, $\times 3$, $\times 5$, $\times 6$.
- **Second-order LPF:** Implemented with a 397.40 Hz cutoff frequency, further reducing high-frequency components outside the sEMG spectrum.
- **Voltage Comparator:** Introduced to detect TC events by comparing the signal to an adjustable threshold, featuring a 30 mV hysteresis for reliable switching. The analog threshold is provided by a DAC component, controlled via I2C commands from the MCU.

- **Voltage Regulator:** Added to adjust the 3.3 V supply voltage to a 2.5 V range for all board components.

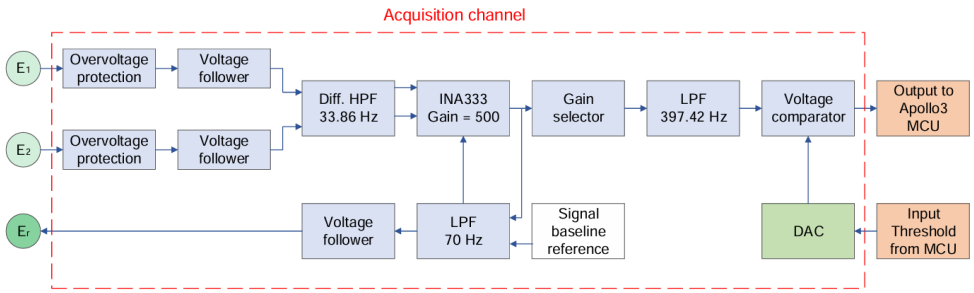

Figure 2.11. Schematic block diagram of the AFE proposed for the previous prototype [48].

The system was based on an AmbiqMicro Apollo3 Blue Evaluation board, integrating an ARM Cortex-M4 processor. For this application, the main clock frequency was set to 24 MHz, using a 32.768 kHz crystal for the 130 ms time window needed for ATC computation. The board was powered at 3.3 V through an external device, which in this case is a computer. The MCU firmware, developed with ARM Development Studio IDE v2020.1, benefited from its compatibility with the ARM product family and support packages, including the Digital Signal Processing (DSP) library for Cortex-M-based devices. It was built on previous projects for acquiring, processing, and transmitting muscular information, incorporating FreeRTOS for multitasking and real-time operations. A BLE server, integrated for data exchange and control, facilitated client/server communication with a laptop as the central device. Supported by ARM's Cordio Bluetooth module, it provided a full Bluetooth stack and APIs for seamless microcontroller integration, offering a robust solution for Bluetooth connectivity and real-time IoT device communication.

The BLE server, taking inspiration from earlier models [29, 46], provided essential functionalities for device management and monitoring:

- **Command:** Initiates specific routines such as activation, gain selection, notifications, and ATC threshold calibration;
- **Status:** Displays the board's current operational status, accessible for reading or notification;
- **Available:** Indicates each AFE board's operating state, adjustable to reflect changes in availability and status;

- **Gain:** Shows the board AFEs' gain multiplier, which can be read or manually adjusted for individual or multiple board groups;

- **ATC:** Provides the latest ATC data computed for up to nine acquisition boards, it also includes the duration of the last ATC window and the packet number, with updates through notification;

- **Threshold:** Enables reading or manual setting of threshold values for each board, from 0 V to 2.5 V;

- **Prediction:** Deliveres the latest predicted class and corresponding packet number, via notification requests.

The prototype featured a Graphical User Interface (GUI) for system control via computer, simplifying the training and testing stages. This Python-based software, inspired by the architecture of prior projects, was structured into three primary layers. The BLE Module, as the foundational layer, managed connections and data exchange between the Apollo3 board and external devices. The Ap3 sEMG System Module, the intermediary layer, converted user inputs into executable commands and processed incoming data. The GUI included a Control Panel for managing system connections, enabling boards, and calibrating ATC thresholds, necessitating subjects to stay motionless for precise adjustments. A Testing Panel aided in building the dataset and the testing phase, directing subjects with visual and auditory prompts, and labeling data based on the executed expressions. This labeling took into account possible response delays, employing a standard and threshold method to accurately determine the expression being performed.
As concerns the classifier developed to identify the 11 facial expressions presented in Section 1.1.4, the choice fell on an ANN model comprising 1 layer with 42 nodes and a regularization term (λ) equal to 0.001. To train and validate the network, 30 healthy subjects were recruited, and a k-fold cross-validation method was implemented. During the training phase, the dataset was divided into 5 groups, with 4 groups serving as the training set and 1 as the cross-validation set. This process was repeated twice, meaning the dataset was split into 5 groups on each occasion, and each model underwent training and validation 5 times to ensure every group had an opportunity to serve as the cross-validation set.

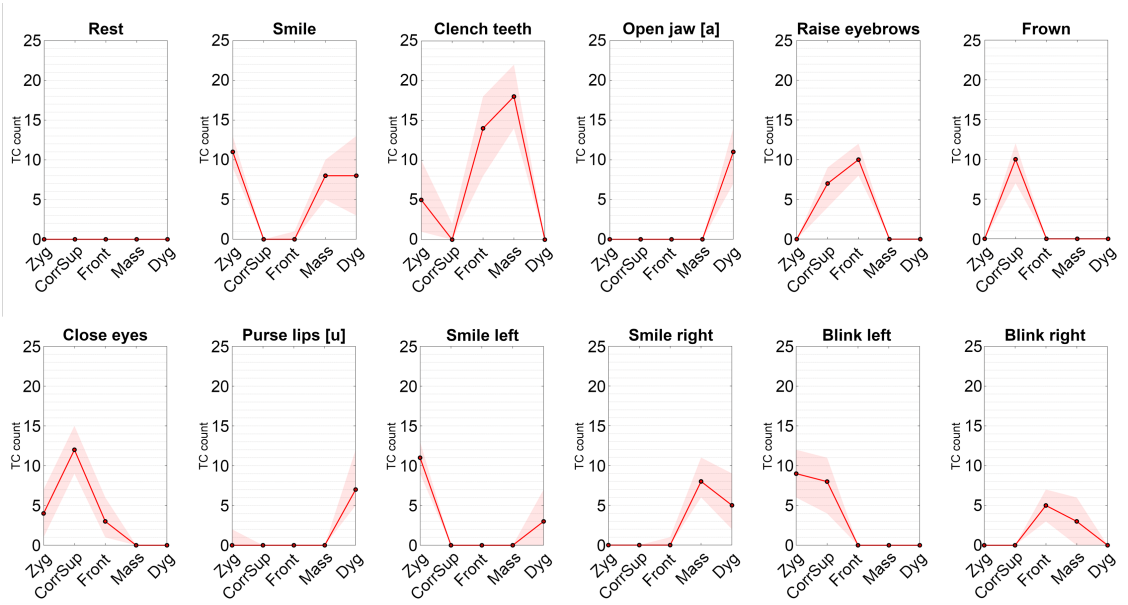

Figure 2.12. Representation of muscular activations and associated expressions used to train the ANN [48].

In a testing phase with 6 additional subjects, the system achieved an high average classification accuracy of 97.4%. Power consumption was minimal at 0.593 mA, and with a total application latency of 205.627 ms, it shows promise for HMI applications.

However, the prototype's usability is hindered by several constraints:

- **Disposable Ag/AgCl electrodes:** Although the gel ensures good adherence, the necessity of using socket/clip heads for cable connections significantly escalates both the electrode's overall weight and stiffness, making them uncomfortable and cumbersome, and impeding facial expression execution. Increased stiffness also substantially reduces the electrode's adherence to the skin, preventing it from conforming to skin deformations caused by facial expressions. Moreover, positioning 11 electrodes for each acquisition amplifies preparation time, positioning variability, and material wastage.
- **Utilization of shielded cables:** This additionally augments the weight imposed on the electrodes, diminishing adhesion duration and further burdening the face.
- **Plugged-in power supply:** Together with the previous point, this aspect prevents the prototype from being wearable, thereby reducing the subject's range of motion. Consequently, during the utilization, the subject is restricted to a seated position close to the power source.

Chapter 3

Medusa Prototype

The practical applicability of the previously developed prototype was limited by the factors discussed in the previous section, despite its promising performance. This thesis aims to enhance the applicability of the prototype in the field of sEMG-based FER by developing a new prototype that combines the qualities of the previous one with improved wearability.

Figure 3.1. The picture shows the developed prototype.

3.1 System Requirements

The design started with the definition of the following system requirements, which guided all design choices made in the development.

- **Adaptable and stable electrodes placement:** As discussed earlier, a key functionality of the system is to minimize electrode detachment. This is crucial because even partial electrode detachment, which often happened with Ag/AgCl electrodes, can corrupt the acquired signal, necessitating periodic reapplication.
- **High quality of the acquired signals:** The acquisition system must accurately represent muscle activity, minimizing noise that would compromise the integrity of the acquired signals. This specification is critical to ensure the system's utility, without which any application proposal would be meaningless.
- **Lightweight & comfort:** As a facial application, comfort is of primary importance, both to minimize interference with movement and to make use more appealing to potential users.
- **Portability:** This characteristic is important to increase the device's usage versatility, allowing the subject to move freely within a few meters (determined by the capabilities of the BLE connection).
- **Power efficiency to enable battery operation:** This feature is crucial for making the device suitable for long-duration applications, avoiding activity interruption or limitation during battery recharging.
- **Wireless Connectivity:** Seamless data exchange between the prototype and an external device eliminates the necessity of connection cables, thus enhancing the prototype's wearability.
- **Ease of use of the whole system:** The system's usability hinges on the simplicity of wearing the device, straightforward electrode placement, and intuitive interaction with its functionalities.

3.2 System Architecture

The system, illustrated in Figure 3.2, was developed with a comprehensive design approach, starting from the acquisition and analysis of sEMG signals, and proceeding with the development of two printed circuits. The development then continued with the 3D printing of a mechanical support and concluded with the firmware and software implementation to achieve a functioning prototype suitable for future applications.

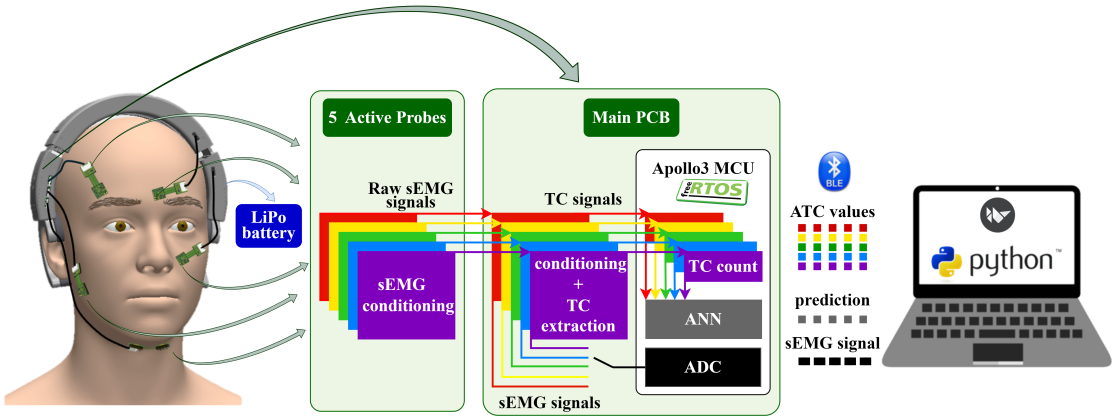

Figure 3.2. System overview of the implemented prototype.

The prototype consists of the following functional parts:

- **5 Active Probes:** Designed to be positioned directly on the face for acquiring high-quality sEMG signals, ensuring prolonged electrode adhesion. They constitute the initial signal conditioning block as described in Figure 3.3, producing a partially conditioned sEMG signal fed into the main PCB.
- **Main PCB:** Engineered to fit within the mechanical support, it provides additional sEMG signal conditioning (Figure 3.3). This stage outputs two signals for each of the 5 acquisition channels: a fully conditioned sEMG signal and a TC signal, from which the ATC parameter is calculated as described in Section 1.3 and then provided as output. The board, based on the Apollo3 Blue MCU, also features dedicated power management circuits, Flash memory, and an Inertial Measurement Unit (IMU), added for future applications.
- **Mechanical Support:** Designed in SolidWorks and 3D printed to ensure the wearability of the device.
- **Lithium-Polymer Battery:** Selected by the research team [29] for its lightness, high capacity, low leakage risk, and elevated recharging speed, it is the

ideal choice for portable applications and advanced technologies.

- **nRF52840 BLE dongle**: It is a versatile USB device produced by Nordic Semiconductor, which provides wireless BLE connectivity between the prototype and the computer used to visualize the GUI.
- **Adhesive Tape**: It enables the adhesion of active probes to the face; its performance is crucial for the quality of the acquired signals. For this prototype, a skin-friendly, breathable, elastic, and waterproof film roll (Fixomull produced by Leukoplast) was selected.
- **Firmware:** The firmware structure closely follows the one proposed in [29] and inherits some features from [48]. It thus relies on FreeRTOS for parallel execution of multiple tasks, leverages the DSP library for signal processing, and the Cordio module for managing BLE wireless connectivity. As regards the classifier, The ANN architecture trained in [48] was implemented at the firmware level, enabling real-time prediction of 11 facial expressions.
- **Software:** Developed in Python with a modular and object-oriented approach, it facilitates computer interfacing with the MCU, managing data exchange via services and characteristics implemented in the firmware-level Bluetooth stack.

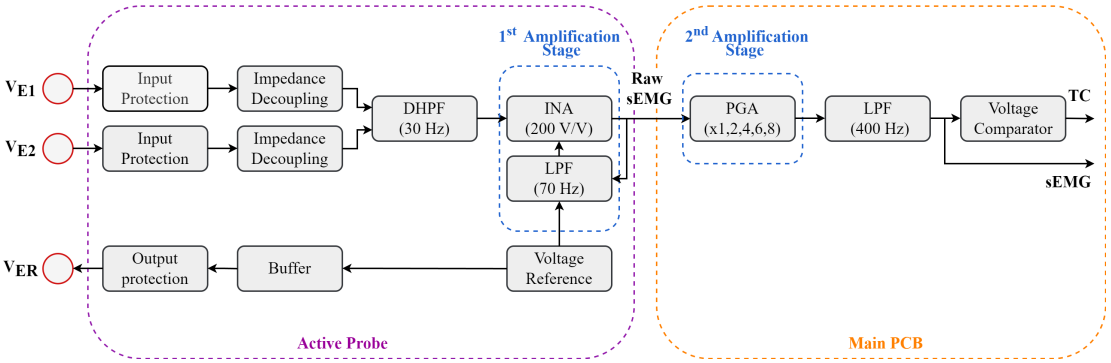

Figure 3.3. Schematic block diagram of the AFE proposed for the implemented prototype.

Chapter 4

PCBs Hardware Design

4.1 Active Probes

To tackle the issues identified in the previous prototype regarding the use of disposable electrodes and shielded cables, the active probes, illustrated in Figure 4.1, were designed.

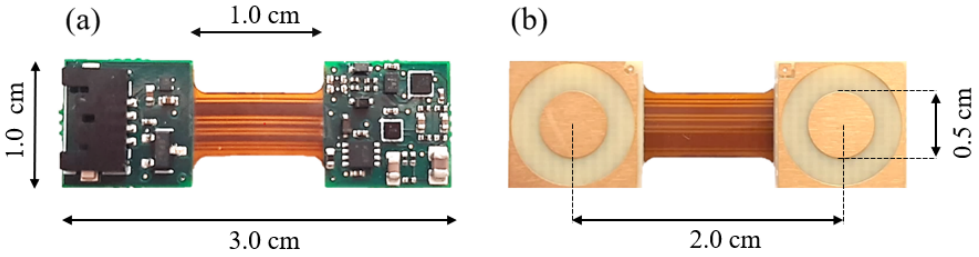

Figure 4.1. Developed Active Probe front side (a) and back side (b).

The printed circuit boards (PCBs) were developed taking into account the following requirements.

- **Skin Adhesion**: The probe must have a geometric shape and mechanical characteristics that ensure good adhesion to the facial skin, thereby prolonging the adhesion time.
- **Signal Quality**: A high quality of the signal acquired is crucial for the reasons described in Section 3.1.
- **Mechanical Strength**: The probes, designed to be positioned on the face using adhesive tape, must be sufficiently robust to withstand placement, usage, and removal without damage.

- **Manufacturability**: The probes should be manufactured commercially or through the resources provided by the research team.

In order to meet all the above requirements, it was decided to create active probes with Gold-plated electrodes. This solution allows the realization of dry and reusable electrodes, easily manufacturable by a PCB manufacturer [45]. Furthermore, the application of signal conditioning close to the point of signal acquisition allows to obtaining high-quality signals, thus improving the performance of the implemented dry electrodes (Section 1.2.3).

4.1.1 Preliminary Tests to evaluate the electrodes configurations

Preliminary tests were carried out to determine the most suitable electrodes configuration to be implemented in the active probes. The traditional Ag/AgCl electrodes were compared with 5 different gold-plated electrodes, shown in Figure 4.2. The recordings were performed using both the previous prototype with its Ag/AgCl electrodes and two acquisition boards developed by the research team: the first has two sockets for placing the Ag/AgCl electrodes, and the other is equipped with connectors for testing the different Gold-plated electrode configurations.

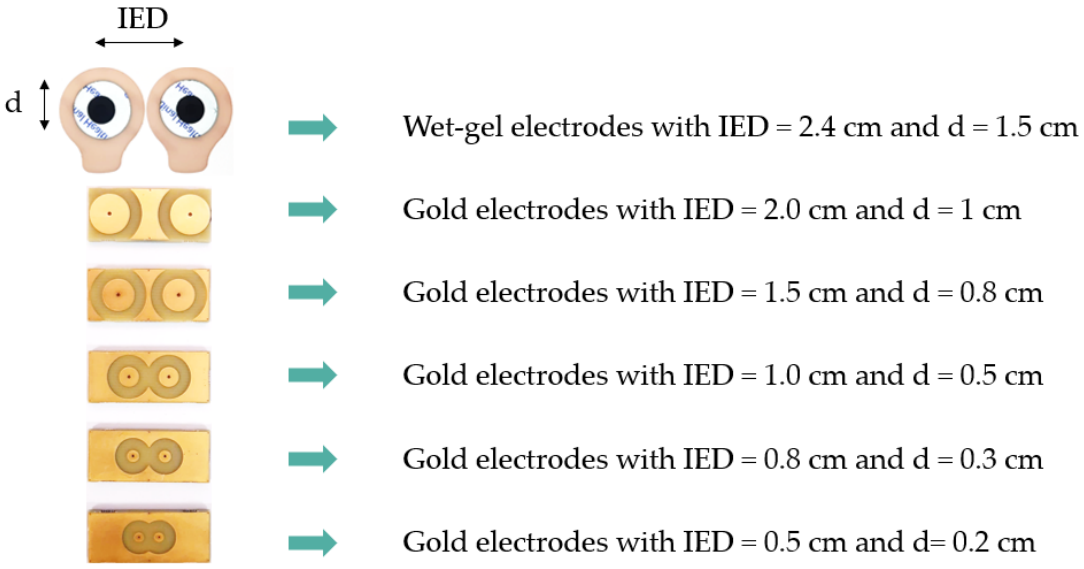

Figure 4.2. Configurations of electrodes tested for the design of the active probes.

The recordings were performed both on the *Biceps Brachii* and the facial muscles of interest, following the acquisition protocol presented in Figure 4.3, which

includes:

- 25 s of initial rest, from which 5 windows of 5 s each are extracted;
- 5 contractions at 30% of MVC lasting 10 s each, from which 5 windows of 5 s each are extracted, centered within the 10 s. Each contraction is followed by 10 s of rest;
- 10 s of pause for weight change;
- 5 contractions at 70% of MVC lasting 10 s each, from which 5 windows of 5 s each are extracted, centered within the 10 s. Each contraction is followed by 10 s of rest.

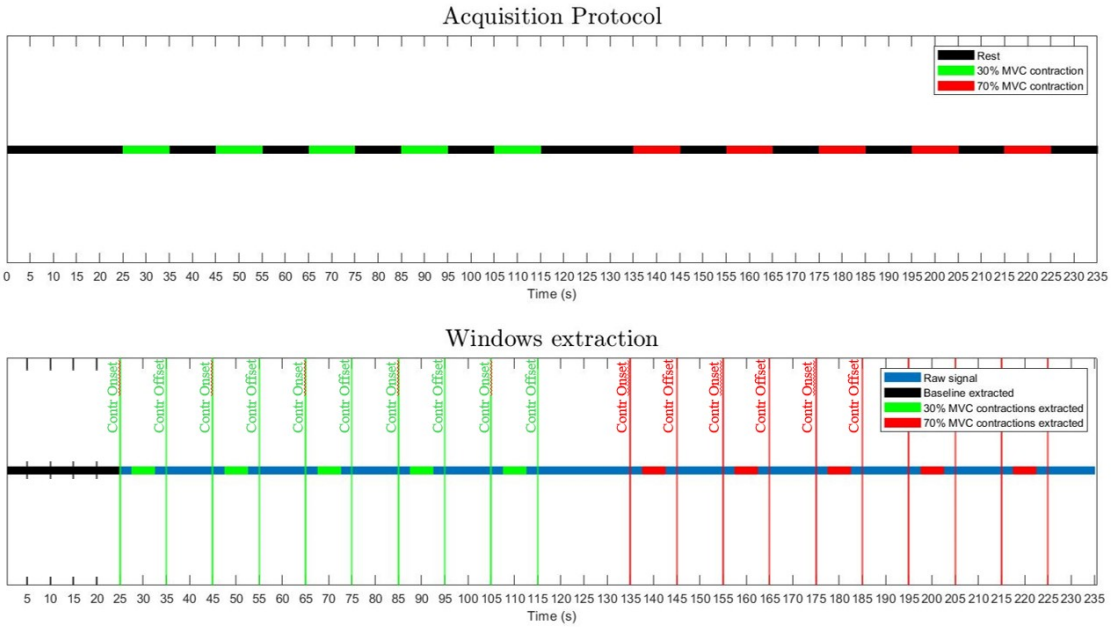

Figure 4.3. This image represents the acquisition protocol (a) and the signals windows extraction procedure (b).

Acquisitions were repeated twice: once to capture the sEMG signal and then to measure the ATC parameter. The gain was set at 200 V/V (x1) for all the recordings.

To establish the quality of the acquired signals, the SNR was calculated as follows:

$$SNR = 10 \cdot \log_{10}\left(\frac{P_{\text{EMG}}}{P_{\text{noise}}}\right) = 10 \cdot \log_{10}\left(\frac{\sigma^2_{\text{signal}} - \sigma^2_{\text{noise}}}{\sigma^2_{\text{noise}}}\right) \tag{4.1}$$

This metric assesses the contribution of the sEMG signal relative to the background noise. The reference value is set at 15 dB, to ensure that the quality of the sEMG signal meets acceptable standards [49].
As the input to the final classifier will be the ATC parameter, the values obtained for each extracted window were grouped by contraction condition (30% MCV and 70% MVC) and averaged to provide another reference for estimating signal quality. In addition, a frequency analysis was performed to investigate two main aspects: the influence of the acquisition system transfer function on the signal and the presence of potential noise sources. The power spectral density (PSD) was calculated using the Welch method, implemented as follows:

$$[PSD, f] = pwelch\left(x - \text{mean}(x), \text{hamming}\left(\frac{\text{length}(x)}{a_{clen}}\right), \frac{\text{length}(x)}{a_{clen}} \cdot 2, NFFT, f_s\right) \tag{4.2}$$

The input x corresponds to a window of 5 s duration (acq_{len}), extracted from sEMG signals acquired at 1 kHz (f_{s}) as shown in Figure 4.3 (b). Using the *pwelch* function (available in MATLAB), each input was divided into smaller windows of 1 s with 50% overlap to obtain a theoretical frequency resolution of approximately 1 Hz. This analysis provides a detailed representation of the power distribution of the signal at different frequencies while reducing the typical variability of the sEMG signal spectrum. The results obtained with the previous prototype (Table 4.1) serve as a benchmark to assess the signal quality yielded by this device. It should be noted that the x1 gain selected for these acquisitions is equal to 500 V/V, higher than that of the acquisition boards (200 V/V).

Table 4.1. SNR and ATC values on *Biceps Brachii* for all the available gain values.

	30 % MVC Contraction	**70 % MVC Contraction**
SNR (dB)	33.4 ± 3.7	53.0 ± 4.2
ATC values	3.1 ± 1.3	7.3 ± 1.1

The results obtained with the evaluation boards from the *Biceps Brachii* are shown in Figure 4.4, 4.5, 4.6.

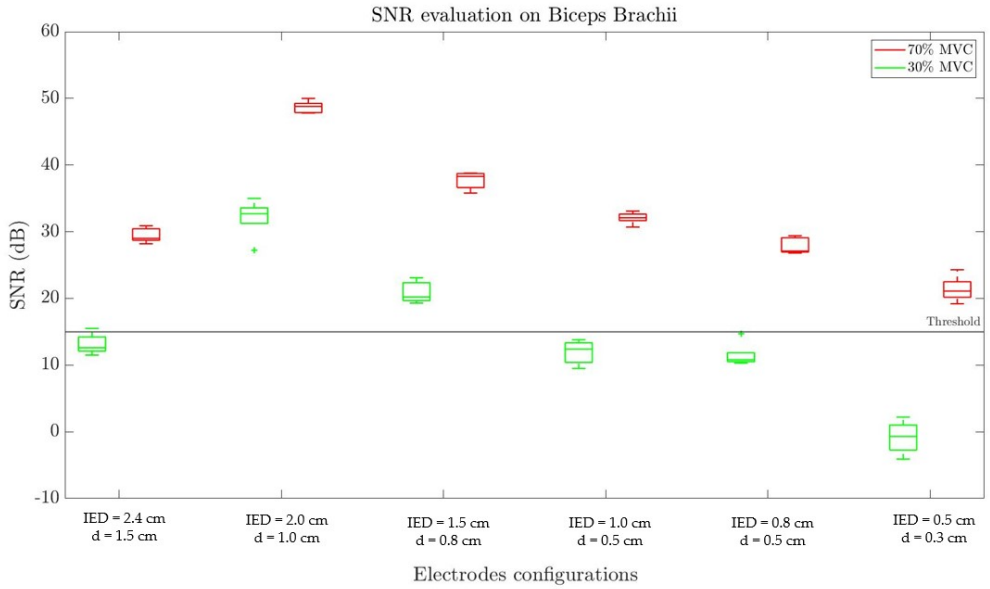

Figure 4.4. SNR evaluated on *Biceps Brachii* for the electrodes configurations illustrated in Figure 4.2. Signals exceeding the black horizontal line, set at 15 dB, are considered of acceptable quality.

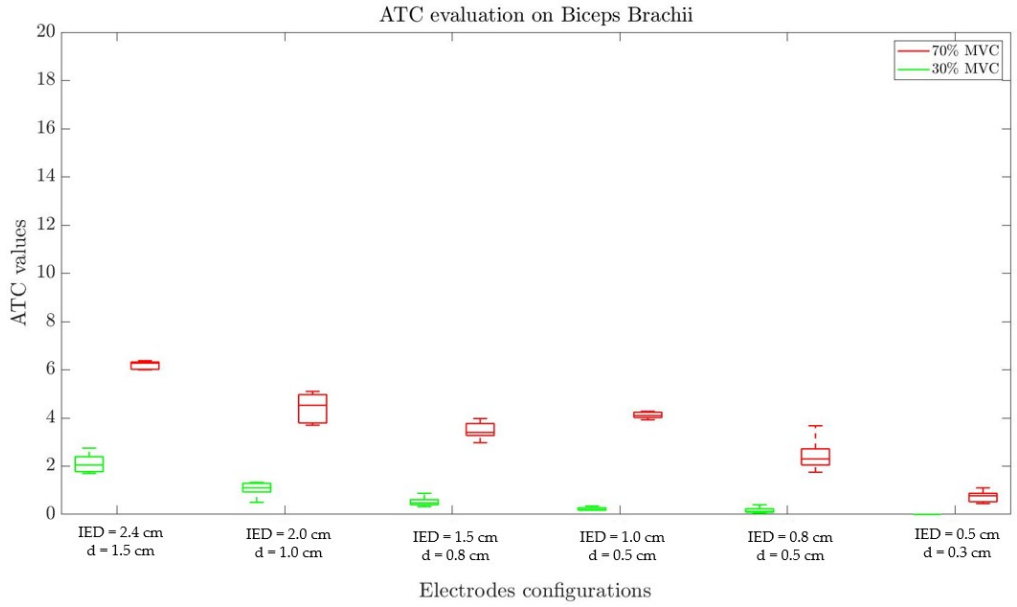

Figure 4.5. ATC evaluated on *Biceps Brachii* for the electrodes configurations illustrated in Figure 4.2.

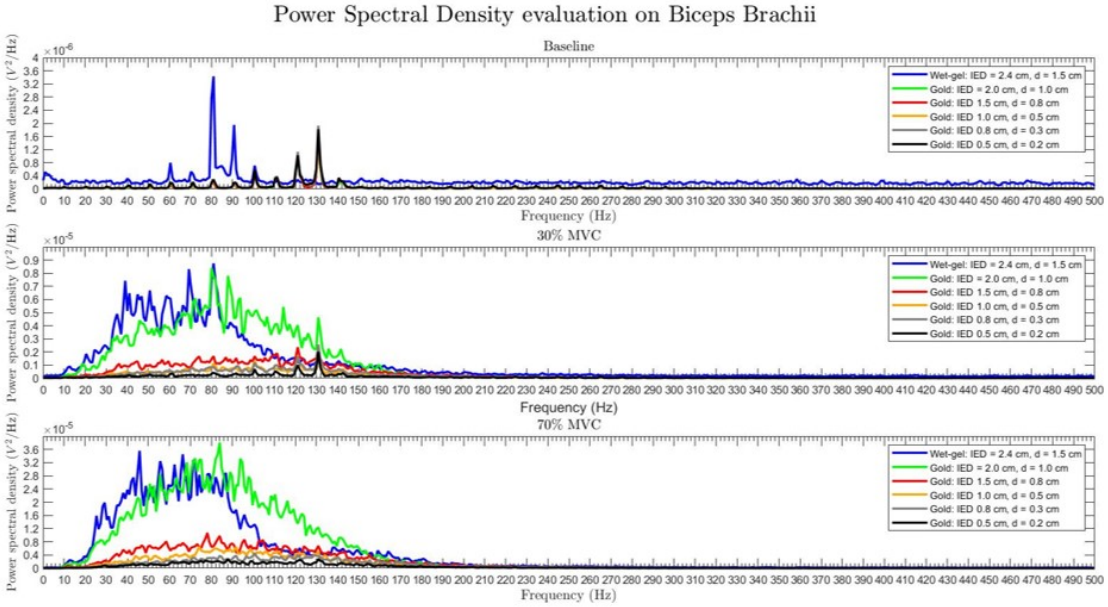

Figure 4.6. PSD evaluated on *Biceps Brachii* for the electrodes configurations illustrated in Figure 4.2.

Therefore, from the results obtained above, it was concluded that IED = 0.8 cm and d = 0.3 cm is the smallest configuration capable of detecting the sEMG signal. On the other hand, the configuration with IED = 1.5 cm and d = 0.8 cm was found to be the smallest layout capable of detecting a signal with an SNR equal to, or greater, than the acceptable threshold.

To obtain a more representative estimate of the final application performance of the electrodes, tests were also carried out on 5 facial muscles. In this case, the test was performed with the two smallest configurations capable of detecting a significant signal in previous tests (IED=1.0 cm and d=0.5 cm; IED=0.8 cm and d=0.3 cm). It's important to note that performing isotonic and isometric contractions on the face, which are essential to ensure the reproducibility of measurements, is particularly challenging. Additionally, the SNR values obtained from facial muscle contractions generally exhibit lower values than those obtained from the bicep. This is because facial muscles always display slight activity, even when not actively contracted, to maintain facial tone. Moreover, it should be mentioned that the size of the recording plates was critical, hindering movement and causing frequent electrode detachment. The signal recorded from the target muscles (*Zygomaticus*, *Corrugator Supercilii*, *Frontalis*, *Masseter*, *Digastric*) gave an average value of about 8 dB for medium contractions and 19 dB for intense contractions for the IED = 0.8 cm and d = 0.3 cm configuration, and 11 dB and 25 dB, respectively, for the IED = 1.0 cm, d = 0.5 cm configuration.

Table 4.2 shows the results obtained specifically for the *Zygomaticus*, which will serve as a benchmark for further evaluations. This muscle was selected because it presented intermediate SNR values among all muscles and allowed for the most reproducible results considering the size of the acquisition board.

Table 4.2. Summary of the SNR values obtained on *Zygomaticus* for the selected electrodes configurations.

Electrodes Configuration	**SNR (dB)**	
	Medium Contraction	**Intense Contraction**
IED = 0.8 cm, d = 0.3 cm	10.0 ± 1.7	17.1 ± 2.2
IED = 1.0 cm, d = 0.5 cm	12.4 ± 3.3	20.9 ± 2.1

It was therefore found that, for facial muscles, the latter configuration was the smallest capable of capturing a signal of acceptable quality.

Considering that the boards' rigidity posed significant challenges in ensuring adequate electrode adherence, and the need for superior signal quality to achieve high-accuracy FER, a custom electrodes configuration was selected. This choice leverages the Rigid-Flex technology for manufacturing the active probes, which allows the implementation of a greater IED, without compromising electrodes adherence. The best trade-off between probe adherence and signal quality features:

- d=0.5 cm, which proves to ensure acceptable signal quality;
- IED=2.0 cm, which provides greater sensitivity and enhances the overall signal quality.

This combination is expected to provide a signal quality that is intermediate to the ones of the respective initial configurations (IED = 2.0 cm and d = 1.0 cm, IED = 1.0 cm and d = 0.8 cm), which is adequate for the intended application.

4.1.2 Circuital components

For the analog design of the probes, the devices developed by the team (see Appendix) were used as a reference. The probes include the following basic blocks:

- Two exploring electrodes;
- An active electrode, that imposes a voltage of 0.9 V on the skin, to center the dynamics of the input signal on that of the INA with single-supply;
- Protection circuit;
- Impedance decoupling;
- DHPF, with a cutoff frequency of 33.86 Hz;
- MAX41400 INA, which offers electronic characteristics suitable for the acquired sEMG signal, combined with low power consumption, a compact package, and the possibility of being powered at 1.8 V. This component provides a first amplification stage equal to 200 V/V;
- LPF, with a cutoff frequency of 70 Hz;
- Voltage regulator, included for the reasons discussed in the following paragraph;
- Buffer, included for the decoupling of the exploring electrode's impedance;
- A resistor, preceding the reference electrode, is inserted to limit the current injected into the skin.

The main changes made to this circuit were:

- Division of the AFE (Figure 3.3) at the INA's output, implementing in the probes the circuit components between the electrodes and this point. This choice was driven by the need to provide an output signal already sufficiently amplified, to avoid the use of bulky shielded cables (without the need to include the entire original AFE in the active probes, unsuitable for reaching the required level of miniaturization).
- Removal of the DRL circuit, which, as shown in [29], did not provide a benefit in terms of signal quality improvement, which was sufficient to justify the space occupied by the necessary components.
- Replacement of the two LPV821 OPAMPs of the LPF and the reference electrode buffer with the dual OA2ZHA22Q Integrated Circuit (IC), which occupies less space and offers better electronic characteristics.

- Insertion of the voltage regulator, to ensure the correct supply voltage to the components of the active probes, without voltage drops on the connecting cables to the PCB compromising it.

- Insertion of the connector, to bring GND and V_{IN} from the Main PCB to the probes and the partially conditioned sEMG signal in the opposite direction.

- Removal of the INA shutdown, which did not bring significant benefits in terms of power saving.

4.1.3 Stack-up and PCB Layout

As discussed previously, the Rigid-Flex Layer Stack shown in Figure 4.7 was selected. The flexibility of the central section is provided by a layer of Polyimide, a material characterized by the combination of high flexibility and mechanical resistance. The rigid sections contain additional layers that increase stiffness, allowing for the placement of components necessary to realize the AFE of the active probes.

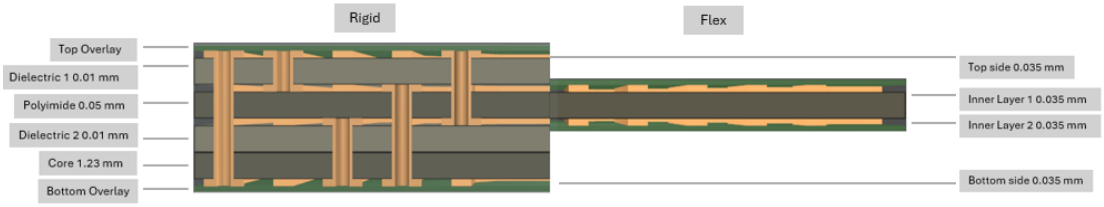

Figure 4.7. Active Probe layer stack.

The challenge of this part of the project was to achieve the necessary miniaturization by positioning the 40 components in the Top Layer of these regions, whose total surface amounts to 2 square centimeters (Figure 4.1, 4.8).

Figure 4.8. Active Probe Top Layer.

In Mid Layer 1 (Figure 4.9), length tuning of the tracks for the exploring electrodes was carried out to compensate for the different distances relative to the INA's inputs and avoid the compromise of the differential signal.

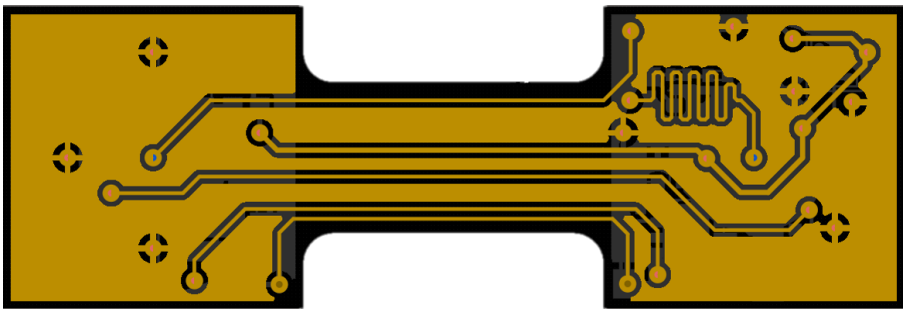

Figure 4.9. Active Probe Mid Layer 1.

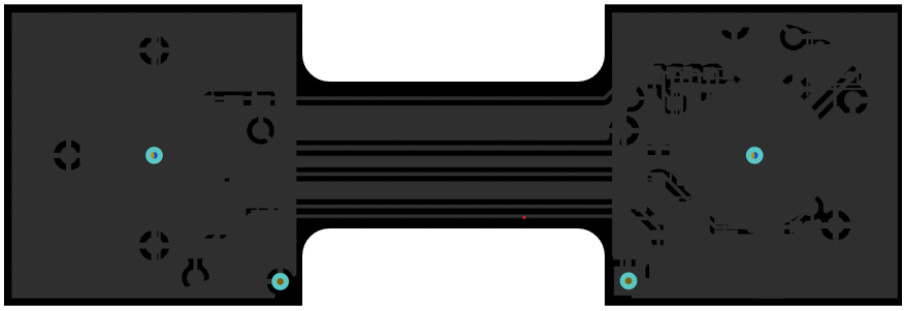

Figure 4.10. Active Probe Mid Layer 2.

The two exploring electrodes were placed on the bottom layer (each one designed with a diameter of 5 mm, as previously determined). They were surrounded by the reference electrode, positioned at a distance of 2 mm, which helps to avoid interference with the exploring electrodes and to maintain the continuity of the geometry.

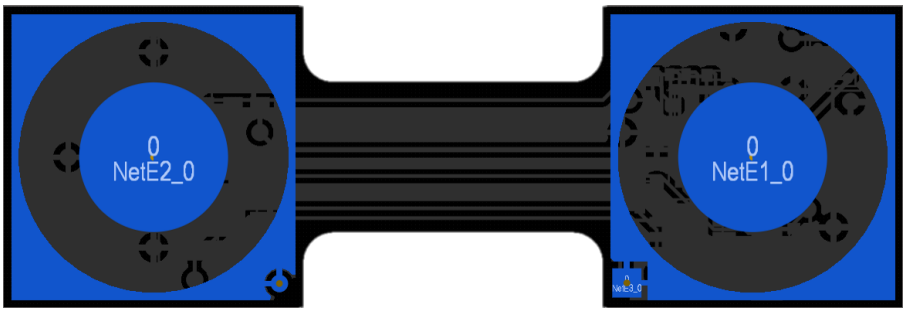

Figure 4.11. Active Probe Bottom Layer.

4.2 Main Board

Figure 4.12 represent the main PCB, which includes further signal conditioning, power management, and communication circuits, in addition to Flash memory and an IMU.

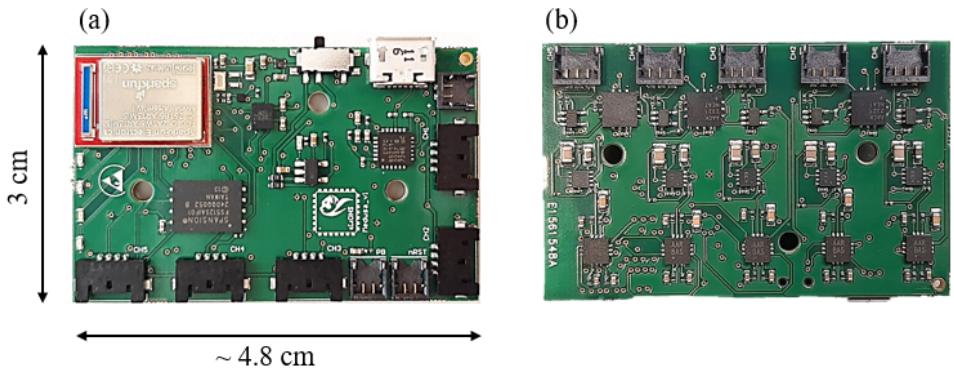

Figure 4.12. Developed main PCB front side (a) and back side (b).

The board was designed with the following fundamental requirements in mind:

- Preservation of signal integrity;
- Effective conditioning of the sEMG signal;
- Miniaturization and straightforward integration with mechanical support;
- BLE connectivity for data transfer to an external device.
- Low power consumption.

4.2.1 Preliminary test for the definition of the PGA gains

With the aim of effectively conditioning the sEMG signal while also considering the need to keep the board's size small, preliminary tests were conducted to determine the gains to implement in the PGA. The device that inspired this approach implemented 8 gains greater than x1 (x2, x4, x6, x8, x10, x12, x14, x16), some of which were often not used because, being too high, they caused excessive sensitivity to noise. By selecting only those gains that are actually functional from the above, it is possible to avoid inserting dozens of unused components (considering the need to implement them for each of the 5 acquisition channels), with significant effects on the final size of the board.

For this purpose, further acquisitions were carried out on the *Zygomaticus* muscle, following the same methods described in the tests of the previous chapter. The results obtained are represented in Figure 4.13. For this test, the Ag/AgCl electrodes were used, as the associate acquisition board allows to evaluate all 8 possible gain values.

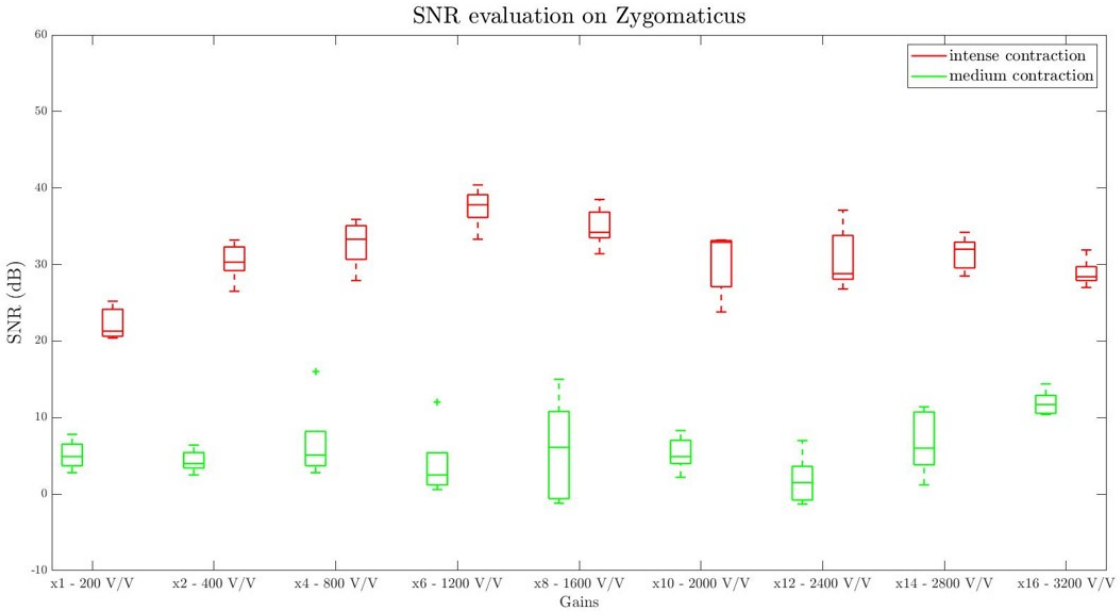

Figure 4.13. SNR evaluation for different PGA gain values.

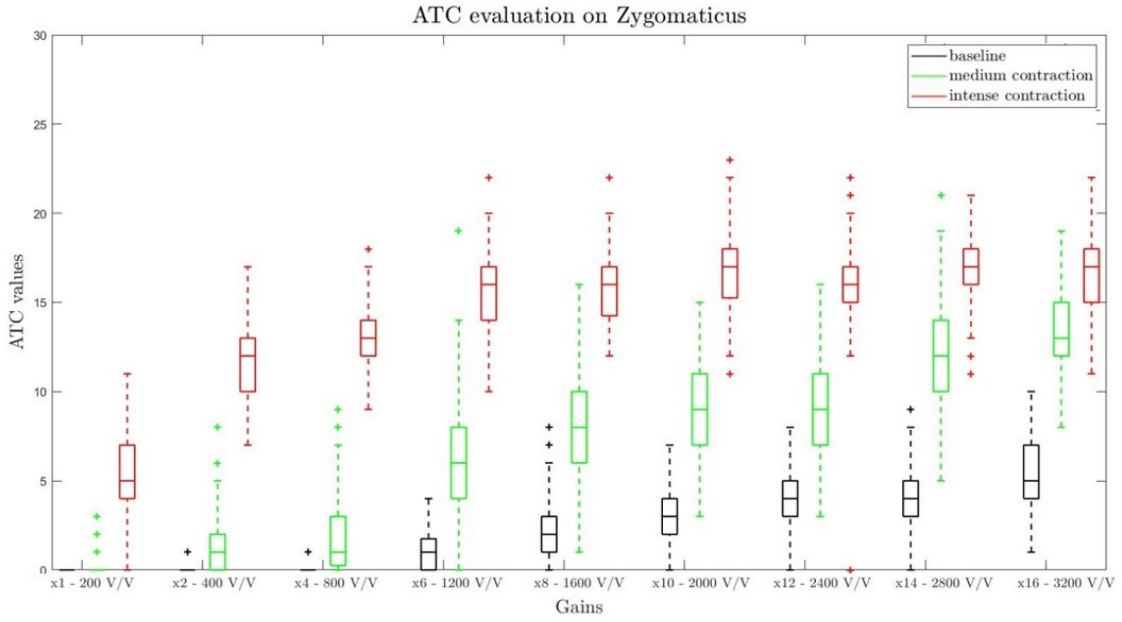

Figure 4.14. ATC evaluation for different PGA gain values.

Results show that starting from gain x6 (1200 V/V), sensitivity to noise increases with increasing gain (Figure 4.14). From gain x8 to higher values, the SNR does not increase any further (Figure 4.13). Therefore, the following gains have been implemented in the PGA: x1 (200 V/V), x2 (400 V/V), x4 (800 V/V), x6 (1200 V/V), x8 (1600 V/V).

4.2.2 Circuital components

As introduced previously, the main PCB developed provides further conditioning of the sEMG signal (Figure 3.3) through the following functional blocks implemented for the 5 acquisition channels:

- Connector, that allow connection with the active probes;
- PGA, which provide the second step of amplification, with gains determined through considerations made in the following section;
- Sallen-Key LPF, with a cutoff frequency of 397.4 Hz;
- DAC (for some channels it is shared);
- Voltage comparator, for the extraction of the TC signal.

Aside from the initial division of the AFE described in the previous chapter, the main changes to this module with respect to the reference circuit have been:

- Multi-channel implementation of all analog blocks, because, unlike the reference circuit and AFEs used in the previous prototype, the main board contains all five analog acquisition channels;
- Replacement of the PGA multiplexer, the MAX4781ETE+T was replaced by the MAX4734, which can be driven by 3 MCU GPIO pins instead of 4, saving 5 MCU pins.
- Replacement of the LPV821 OPAMPs with the dual OA2ZHA22Q IC;
- Addition of two dual DACs, to provide the MCU computed thresholds to each voltage comparator.

The digital part consists of:

- Artemis module integrating the Apollo3 Blue MCU;
- USB-to-UART interface;
- Reset and bootloader circuit;
- 4 LEDs.

The primary work on this part involved defining the allocation of the microcontroller inputs, allowing all fundamental functions for the 5 acquisition channels to be carried out with the available number of pads. Table 4.3 shows the defined allocation, which also took into account the PCB design needs, aiming to simplify track tracing and thus enable miniaturization.

In this project, for instance, the reading of thresholds calculated by the ADC has been omitted. In addition, 3 LEDs have been added and the I2C daisy chain connectors have been removed, as the main board doesn't need to be digitally connected to other boards for serial connection. As presented above, the main board also contains circuits and components dedicated to power management, such as USB connector, power source selection, voltage regulator, and charging circuitry, as well as accessory components such as flash memory and IMU, which have not undergone any major changes compared to the reference circuit.

4.2.3 Layer stack and PCB Layout

For the Main PCB, the standard 6C 4-Layers EuroCircuits stack-up (Figure 4.15) was selected.

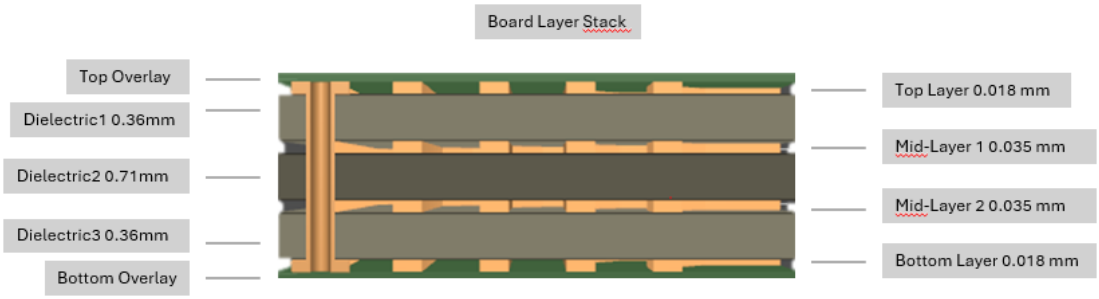

Figure 4.15. Main PCB layer stack.

The following images (Figure 4.16, 4.17, 4.18, 4.19) provide a detailed illustration of the PCB design, which features 170 components on both Top and Bottom Layer for a total size of 4.8 cm x 3.0 cm. The top layer contains the digital, power management, and accessory modules, as well as the connectors for the active probes, the USB port, and the buttons.

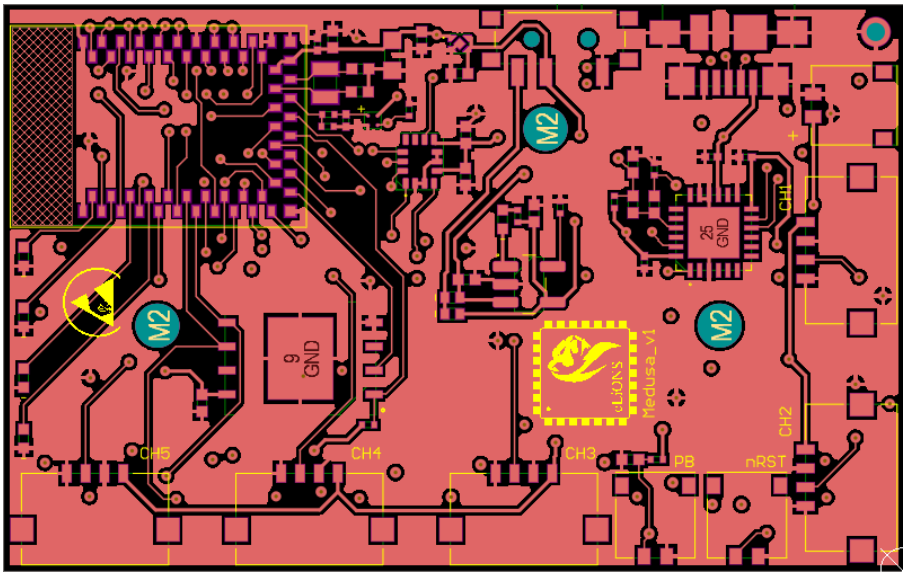

Figure 4.16. Main PCB Top Layer.

In Mid Layer 1 the length tuning of the USB data differential pair was applied to avoid signal distortion.

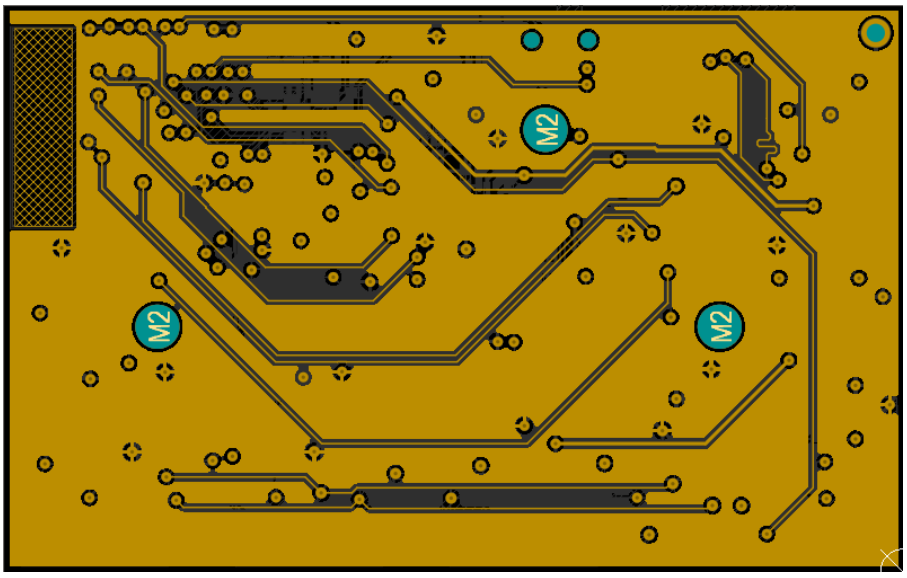

Figure 4.17. Main PCB Mid Layer 1.

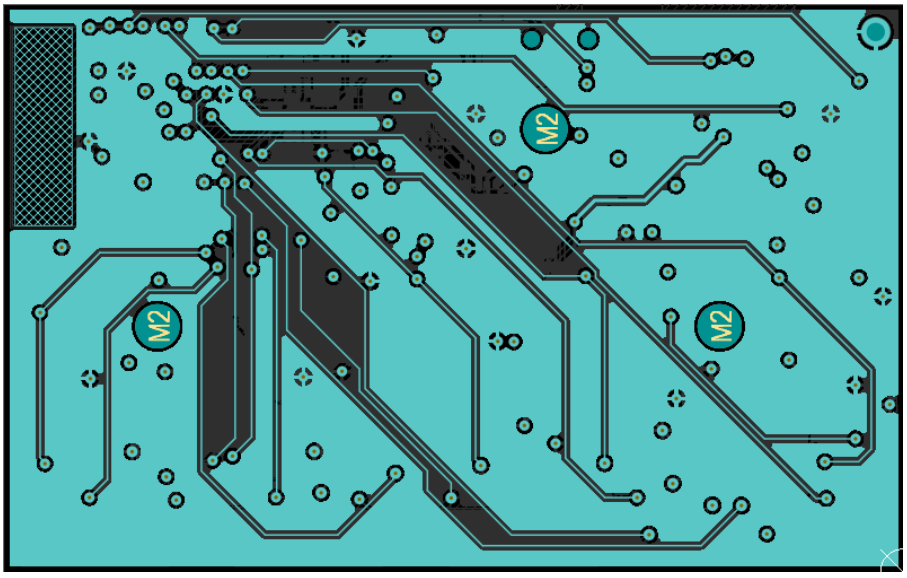

Figure 4.18. Main PCB Mid Layer 2.

The bottom layer contains the analog modules, which run in parallel for the 5 acquisition channels.

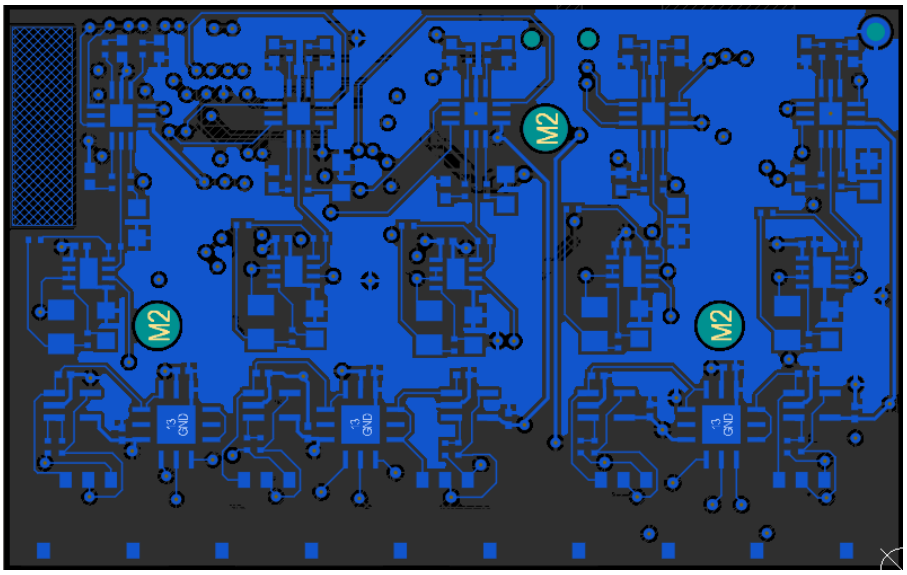

Figure 4.19. Main PCB Bottom Layer.

Table 4.3. Representation of Apollo3 Blue MCU pins allocation, with pad number and relative selected pad function.

Input name	**Pad number**	**Pad Function**
EMG_CH[1, 2, 3, 4, 5]	31, 11, 13, 32, 35	ADCSE[3, 2, 8, 4, 7]
TC_CH[1, 2, 3, 4, 5]	18, 33, 28, 27, 22	CT[4, 23, 7, 5, 12]
IOM0_CS[0,1,2]	23, 24, 14	NCE[23, 24, 14]
IOM0_MOSI	7	M0MOSI
IOMO_SCK	5	M0SCK
MUX_A0_CH*	0, 41, 26, 8, 37	GPIO[0, 41, 26, 8, 37]
MUX_A1_CH*	1, 45, 25, 21, 44	GPIO[1, 45, 25, 21, 44]
MUX_EN_CH*	3, 17, 34, 4, 36	GPIO[3, 17, 34, 4, 36]
UART_TX	48	UART0TX
UART_RX	49	UART0RX
BOOT	47	BOOT
nRTS	~RST	SCCRST
BATT_SENSE_EN	2	GPIO2
BATT_SENSE	29	ADCSE1
CUSTOM_LED[1, 2, 3, 4]	20, 39, 9, 10	GPIO[20, 39, 9, 10]
IMU_INT1	40	GPIO40
IMU_INT2	16	GPIO16
IOM3_CS[0]	12	NCE12
IOM3_SCK	42	M3SCK
IOM3_MOSI	38	M3MOSI
IOM3_MISO	43	M3MISO
Custom_PB	19	GPIO19
IOM0_CS3	15	NCE15
IOM0_SCK	5	M0SCK
IOM0_MOSI	7	M0MOSI

Chapter 5

Mechanical support design

The headset, depicted in Figure 5.1, was designed to meet the need to make the device portable.

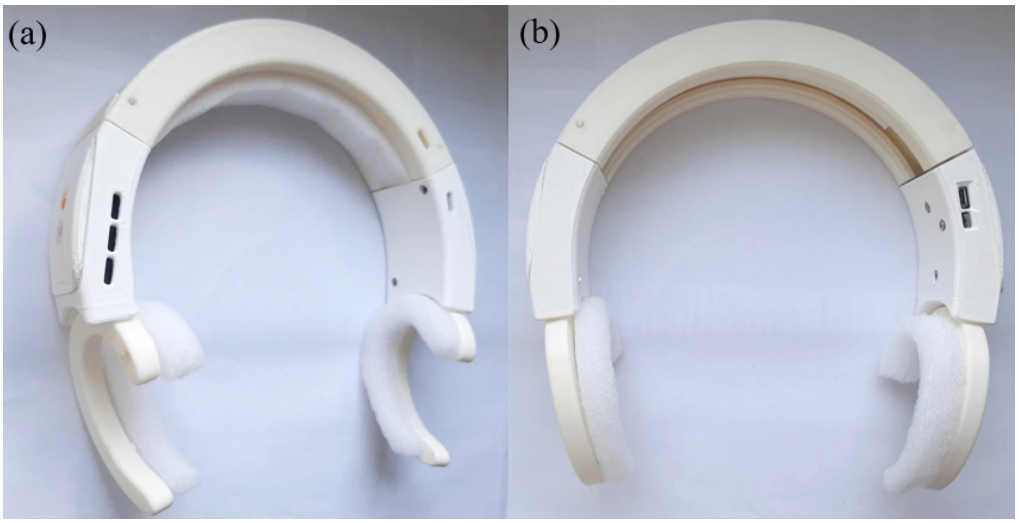

Figure 5.1. Picture presenting (a) front and (b) back side of the 3D printed mechanical support.

To ensure proper functionality, the following requirements were considered in the design:

- Presence of dedicated spaces for the main board and battery;
- Presence of slots for connectors, power switches and buttons;
- Printability of the components using filament 3D printers;
- Assemblability of the printed parts;

- Adaptability to heads of different sizes, ensuring stability and comfort;

- Reduced weight.

The upper support (Figure 5.2) was designed with an inner radius of curvature of 7.5 cm, selected to be slightly less than that which can encircle a small-sized head. This parameter is crucial for ensuring a good fit of the final headset without causing discomfort. Additionally, the piece incorporates several design features to enhance functionality and adaptability:

- Features a cavity for inserting length regulators, with cantilevered stops to provide controlled and quantified relative sliding of parts.

- Includes an opening at the bottom for the insertion of cables from active probes and the battery, spaced by appropriate separators.

- Has openings for the insertion of a probe connector and stoppers (Figure 5.3) designed to halt the regulators' travel and prevent disassembly.

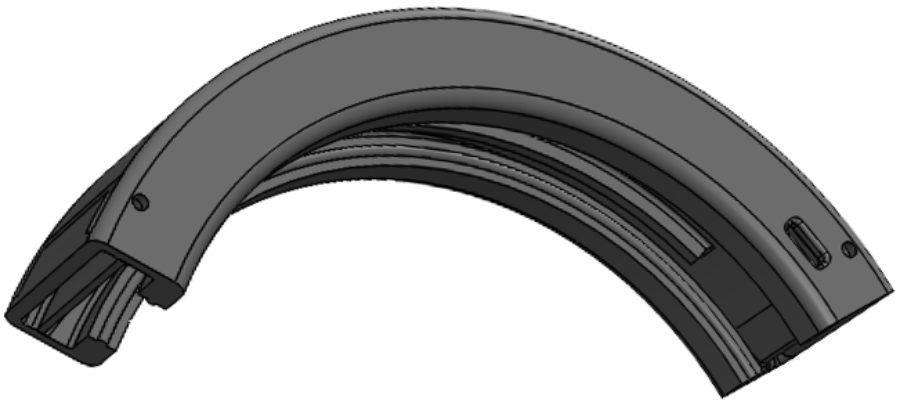

Figure 5.2. Upper support shown with a 3D view to appreciate the details.

Figure 5.3. Close-up of one of the 4 stoppers.

The heart of the system's adaptability lies in the toothed portion of the regulators (Figure 5.4, 5.5), providing length adjustment and flexibility, and protecting components from deformation due to the thickness of other parts. The left regulator hosts the main PCB, enabling its attachment with screws and ensuring full accessibility to each connector. The right regulator, instead, is designed for inserting and protecting the battery.

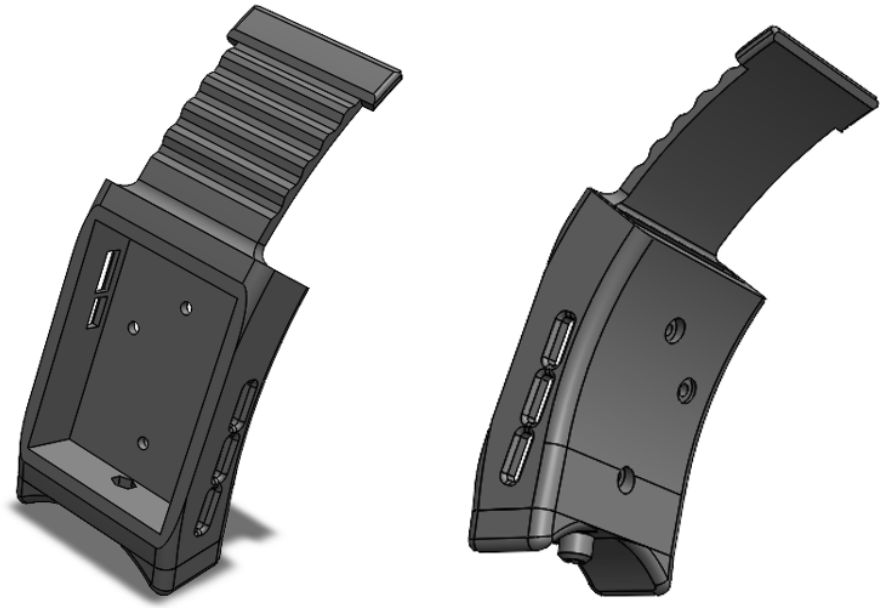

Figure 5.4. Regulator left, represented from two different 3D views.

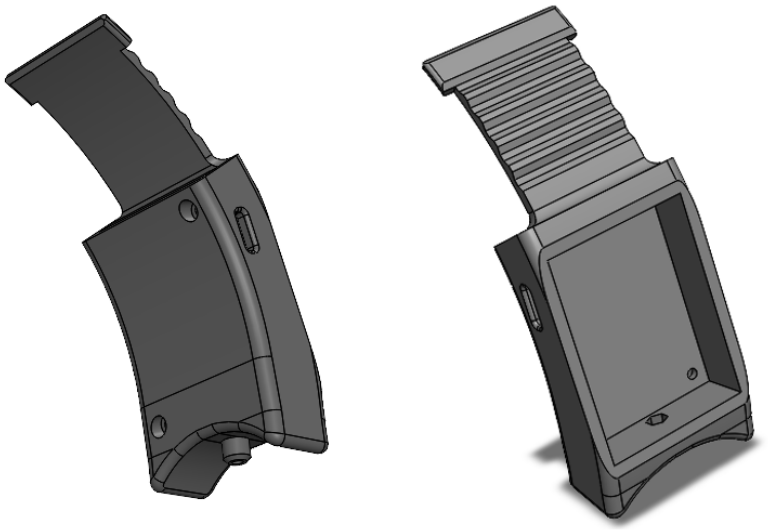

Figure 5.5. Regulator right represented from two different 3D views.

Regulator lids are designed to perform multiple functions:

- Protect the main PCB and battery.

- Acts as an anchor for the screws inserted under the regulators to secure the covers. For the left cover, the screws also tie the position of the main PCB. This functionality is achieved by parallelepiped extrusions with a hexagonal slot for nut insertion, providing a durable thread.

- Provide openings for button insertion (left lid).

- Channel light from the small LEDs on the main PCB (left lid).

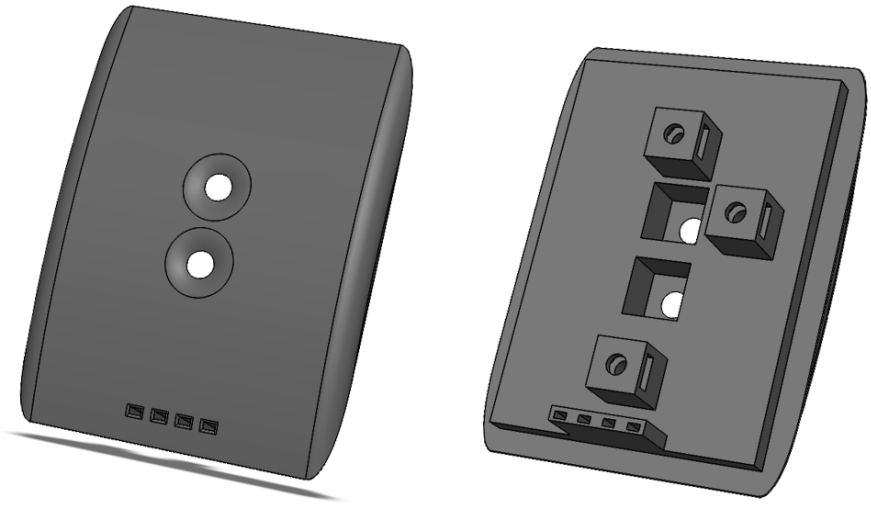

Figure 5.6. Lid left, represented from two different 3D views.

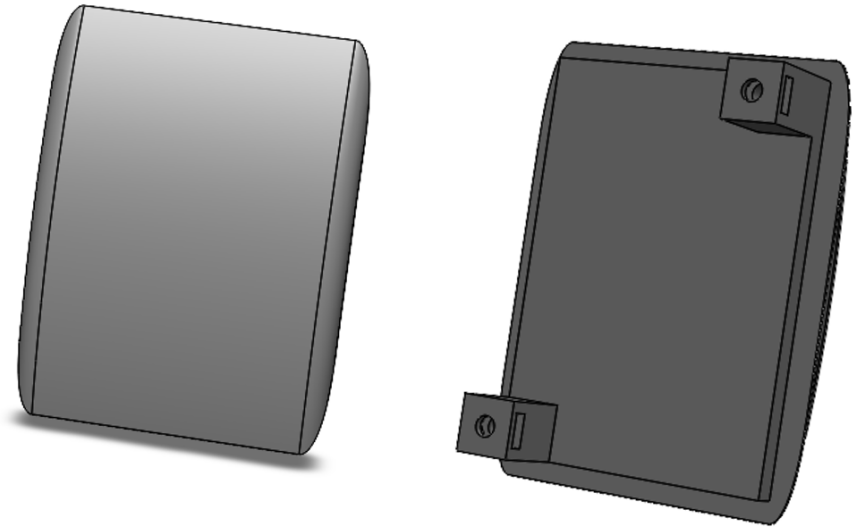

Figure 5.7. Lid right, represented from two different 3D views.

To ensure the headset fits comfortably on the head, ergonomic ear supports have been designed to anchor and stabilize the system without causing discomfort. Finally, soft padding has been added to the inner surface of the ear pads and in the upper pad opening to further enhance the headset's comfort and wearability.

Figure 5.8. Ear support, represented from two different 3D views to appreciate the details.

The parts were then 3D printed, and the PolyLactic Acid (PLA) was chosen for its remarkable mechanical properties, which were critical to making the headset flexible yet durable. This material also requires no post-print processing and is very low cost. The printer used was the Raise3DPro, for which the following parameters were set:

Layer	Layer Height	0.2500 mm
	Shells	3
Infill	Infill Density	15%
	Infill Pattern Type	Gyroid
Support	Generate Support	all
Platform Additions	Platform Addition	Skirt Only
	Skirt Loop Lines	5
	Skirt Offset Distance	0.01 mm
Temperature	Heated Bed Temperature	70 °C
	Left Extruder Temperature	225 °C
	Right Extruder Temperature	226 °C
Speed	Default Printing Speed	60.0 mm/s
	Infill Speed	70.0 mm/s
	X/Y Axis Movement Speed	150 mm/s

The tolerances, essential for ensuring the correct fit between the various mechanical couplings, were finally determined by performing some preliminary test prints.

Chapter 6

Firmware and Software Development

6.1 Medusa BLE Server

Among all the Medusa server services (Figure 6.1), the core of the system resides in the EMG service.

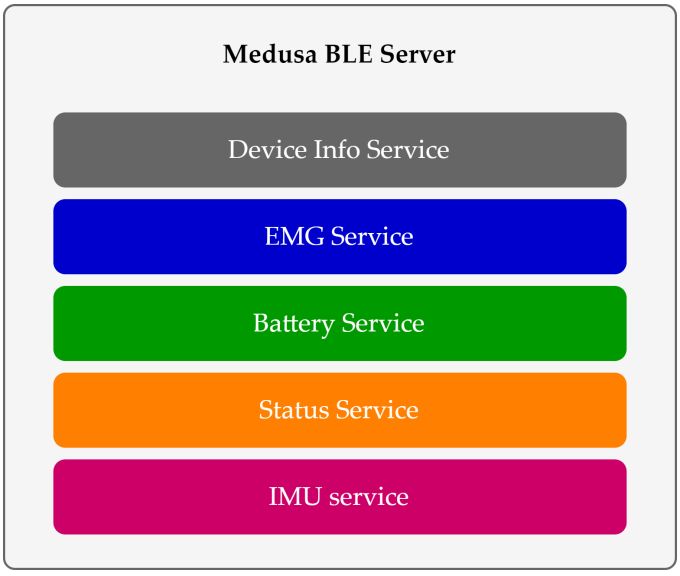

Figure 6.1. Schematic representation of the Medusa prototype BLE services.

The main characteristics implemented for the EMG service are listed in Table 6.1.

Table 6.1. Features of the main characteristics implemented in the EMG BLE service.

Characteristic	**Bytes**	**Permissions**	**Callback**
Parameters	15	Read	-
Command	3 (variable)	Write	Write
Status	1	Read/Notify	-
EMG channel	1	Read/Write	Write
Gain	5	Read/Write	Write
Raw	201	Notify	-
Threshold	10	Read	-
ATC	8	Notify	-
Gesture Prediction	2	Notify	-

To better understand the function of each characteristic, a brief description is provided.

- Parameters: enables reading the parameters set for the board, such as supply voltage, available gains and channels, ADC and DAC resolution, sampling and timer frequency, TC and ATC windows.
- Command: allows the user to control system functions by initiating the execution of specific routines based on the written value. Allows, for example, calibrating thresholds, setting the gain for a specific acquisition channel, selecting the sEMG acquisition channel, and starting and stopping acquisition for enabled features.
- Status: can be read or notified to the user providing information about the execution of a command and the board operating status.
- EMG channel: enables to both set and read the channel selected for the sEMG acquisition.
- Gain: enables to both set and read the gain values of all channels.
- Raw: can be notified to provide the acquired sEMG signal amplitude values.
- Threshold: allows to read the threshold computed for each channel.

- ATC: can be notified to provide the computed ATC values for each channel with the duration of the ATC window and the packet number.
- Gesture Prediction: can be notified to provide the latest predicted class and the relative packet number.

6.2 Firmware

The program is structured in a conventional format, segmented into three principal parts. It begins by specifying all essential constants and variables. Subsequently, it proceeds to describe helpful routines. The culmination is in the initialization of the FreeRTOS tasks. A summary of the routines called by the main function is provided, listed in the order of their application:

- **Clock Frequency Configuration:** Adjusts the system clock frequency based on predefined conditions to optimize performance and power consumption.
- **UART Debug Interface:** If enabled, initializes the UART interface for debugging purposes to facilitate system diagnostics and monitoring.
- **Cache Configuration:** Sets the default cache configuration and enables it to improve processing efficiency.
- **Floating Point Unit (FPU) Configuration:** Enables or disables the FPU based on system requirements to optimize the computational capabilities for floating point operations.
- **Low Power Configuration:** If conditions allow, configures the board for low-power operation, including disabling unnecessary oscillators to save power.
- **Memory Management:** Ensures optimal use of Flash and SRAM by activating only the necessary memory modules to reduce power consumption.
- **GPIO Configuration:** Establishes GPIO settings essential to system operation and lays the foundation for peripheral interactions.
- **Timer Configuration:** Implements timer settings to meet system timing requirements, critical for event management and scheduling.
- **System Clock Check:** Checks the clock frequency using LED indicators to visually report high-frequency operation.
- **ADC Configuration:** If necessary, configures the ADC for analog data acquisition, which is critical for raw EMG data processing or battery health monitoring.

- **Serial Ports Configuration:** Sets up any required serial communication interfaces, ensuring seamless data exchange with external devices.
- **DAC Shutdown:** Disables the DAC to minimize power consumption and prepare the system for energy-efficient operation.
- **EMG Channel and Gain Configuration:** Initializes EMG channel selection and gain settings according to predefined service values, optimizing signal acquisition quality.
- **Flash Memory Initialization:** Prepares the flash memory for data storage, enabling persistent data retention across system restarts.
- **Update Device Information:** Updates device information properties to ensure accurate system identification and configuration reporting.
- **Parameter Configuration:** Establishes communication and operating parameters for various system components to ensure consistent and efficient functionality.
- **IMU Parameter Configuration:** If an IMU is active, sets specific parameters to govern its operation, enhancing motion tracking capabilities.
- **Enable Global Interrupts:** Enables global interrupts, allowing the system to respond effectively to external events and triggers.
- **Execute Application Tasks:** Initiates and manages FreeRTOS tasks, bringing the system into its operational phase, ready to perform its designated functions.

The FreeRTOS tasks mentioned above are designed to perform specific functions that are critical to the operation of the system:

- **Setup Task:** This task is responsible for the global initialization that must occur immediately after the Job Scheduler is started and before any other functional tasks are run. It sets up basic configurations and enables events, semaphores, and other global features critical to the operation of the system.
- **Radio Task:** Manages radio communications, ensuring data transmission and reception via the BLE protocol. Its creation depends on the successful execution of initial setup routines.
- **Threshold Set Task:** Calculates the thresholds necessary to extract the TC signal to implement the ATC technique using a dynamic search algorithm. The computed threshold is then output to the 3 DACs and written to the relative sEMG service trace.

- **Prediction Task:** provides the ATC parameter computed for each acquisition channel as input to the ANN to provide real-time predictions. This task was inherited from the previous prototype.
- **Diagnostic Task:** Performs system diagnostics to ensure that all components are functioning properly. It is an essential task for maintaining system health and performance.
- **IMU Task** Available when an Inertial Measurement Unit (IMU) is active. This task manages the acquisition and processing of IMU data, which is essential for motion tracking and orientation.
- **IMU Diagnostics Task** Complements the IMU task by providing diagnostics specific to the IMU component, ensuring its reliable operation within the system. Since the Meduse prototype doesn't currently manage the values provided by the integrated IMU, this task and the previous one are not used.

The work carried out on the firmware focused on the following main aspects:

- Reallocation of the MCU pins according to the configuration shown in Table 4.3;
- Implementation of the multichannel structure to handle the 5 acquisition channels, with related changes to the BLE characteristics and the functions used for data processing;
- Insertion of a characteristic, command, and functions related to the selection of the sEMG channel to be acquired. Indeed, BLE capabilities do not allow for handling sEMG values coming from all 5 acquisition channels;
- Removal of the threshold reading output from DAC through ADC;
- Implementation of the task and characteristics related to the prediction of expressions, inherited from previous thesis work [48].

6.3 Software

The software design is inherited from both the earlier prototype and a more recent version of the software developed by the research team. It follows object-oriented programming (OOP) principles, has a layered structure, and uses multithreading for real-time system control. Inter-layer data transfer is managed using a queue-based approach to allow the system to efficiently manage different types of data. By inheriting from Kivy's Python classes, the GUI ensures cross-platform compatibility. In addition, the system design accommodates different operating system

environments by using specific hardware configurations for Bluetooth communication (USB dongle or integrated BLE antenna).

The software consists of three main classes:

- **GUI_Medusa:** Initializes a graphical user interface (GUI) for managing connections and data acquisition from the services represented in Figure 6.1. It includes methods for device scanning and selection, data acquisition setup, and real-time data visualization. It also supports user interactions for starting/stopping data acquisition, configuring device settings, and managing data storage preferences. Beside the Control Panel, it also includes a Testing Panel, designed in the previous thesis work, which facilitates the evaluation and characterization of gesture prediction through a structured testing sequence. It manages a series of gestures that participants are instructed to perform, ensuring a consistent and systematic approach to data collection.

- **Medusa:** Defines the Medusa class, which inherits the classes defined for each service of the BLE stack (Figure 6.1). It performs BLE devices search, initializes the selected device, sets up and reads parameters from the BLE services, handles incoming data in real-time, and finally deconfigures the device.

- **System:** Configures the BLE dongle, scans for Medusa devices, establishes connections, enables/disables various notifications (sEMG, ATC, ML), and start/stop data acquisition. It supports setting up channels and gains for the Medusa device. It performs threshold calibration and handles data acquisition in different modes (sEMG, ATC, ML). The system can also save acquisition data to files. It includes a comprehensive set of operations to manage device connection, configuration, and data handling, with the ability to monitor battery levels and device disconnection.

The software development focused on the following aspects to provide a user-friendly interaction with the system:

- Update of parameters and methods from the Status and sEMG services classes, to match the firmware changes described above.

- Implementation of a multi-channel structure to manage the data streaming from 5 acquisition channels to correctly visualize and store ATC, sEMG and gesture prediction data.

- Management of the user operation to set parameters related to the acquisition channel, such as selecting the gain for each channel or selecting the acquisition channel for the sEMG acquisition mode.

- Integration of the updated Control Panel with the Testing Panel.

Chapter 7

Methods for Prototype Validation

7.1 Signal Quality Assessment:

As the first step, the signal quality read from the active probes was tested, both on the face, specifically on the *Zygomaticus*, and on the *Biceps Brachii*. The acquisition protocol described in Figure 4.3 (a) was used for the acquisitions, and the signals obtained were windowed as shown in Figure 4.3 (b). SNR and PSD were calculated on the windows extracted in this way.

For signals from the *Zygomaticus*, the acquisitions were repeated for each of the gains implemented in the PGA.

For the *Biceps Brachii*, an acquisition was made with a gain of *x1*, in order to make it comparable with the data presented previously.

7.2 Classifier Performance and Mechanichal Support wearability

To test the prototype, 7 healthy subjects were recruited, including 2 males and 5 females. The subjects were first informed about the details of the experiment and provided with an information form. Then, according to the guidelines of the bioethics committee, they approved and signed the informed consent form.

Electrodes were placed according to the arrangement shown in Figure 7.1. To confirm correct electrode placement and to determine the gains for each channel, subjects were asked to perform all 11 final expressions sequentially. Electrodes were repositioned and gains were adjusted as necessary until satisfactory ATC activation was achieved on each channel. The actual test then began, following the experimental protocol adopted by [48], which involves the execution of 3 sessions, each

consisting of:

- 20 seconds of initial rest to allow the subject to relax completely and to eliminate any unintended muscle contractions.
- 12 repetitions (rest + 11 expressions) of the sequence:
  - 7 seconds of expression execution
  - 3 seconds rest
  - 7 seconds of expression execution
  - 3 seconds rest
  - 7 seconds of expression execution
  - 5 seconds rest (to change the expression)
- A few minutes of recovery (varying according to the subject's needs) to rest the muscles and record any comments the subject may have about the test just performed.

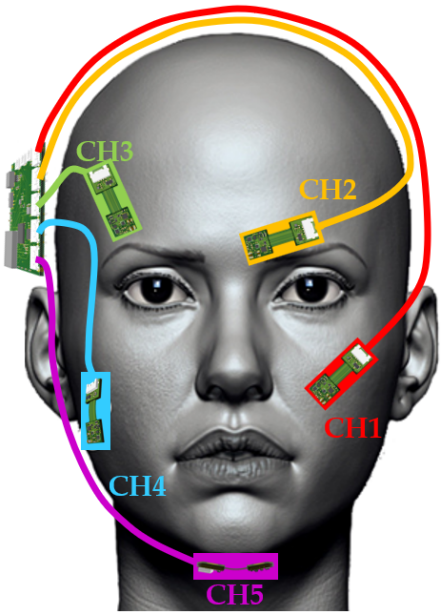

Figure 7.1. Electrode placement adopted to perform the *in-vivo* test.

The acquired data were processed by extracting the predicted and true classes from three 7-second windows obtained during rest. Then, windows corresponding to the other 11 facial expressions were selected, focusing on the predicted and true classes of the lines that met two criteria:

- the true class must be different from 0 (to exclude intermediate pauses)

- the norm of the inputs, calculated as follows, must be equal to or greater than a threshold of 3, as determined in the previous work [48]. This condition was applied because the network was trained to assign a true class of 0 if the norm of the inputs was below the threshold, in order to better separate the classes. The vectors of predicted and true classes were used to compute confusion matrices for each acquisition.

To obtain average data for each subject and across subjects, the confusion matrices were aggregated and metrics were calculated on the combined matrix.

At the end of the 3 sessions, the subject was asked to fill out a form containing questions regarding:

- Exhaustiveness of information provided in the initial phase;

- Overall test timing;

- Effectiveness of the graphical user interface;

- Timing for maintaining facial expression (7 seconds);

- Timing of the rest between repetitions (3 seconds);

- Expressions that were difficult to perform;

- Wearability of the cap;

- Weight of the cap;

- Presence of beard on the face;

- Discomfort caused by medical tape;

- Discomfort caused by cables;

- Suggestions on possible applications of the system.

7.3 Current absorption evaluation

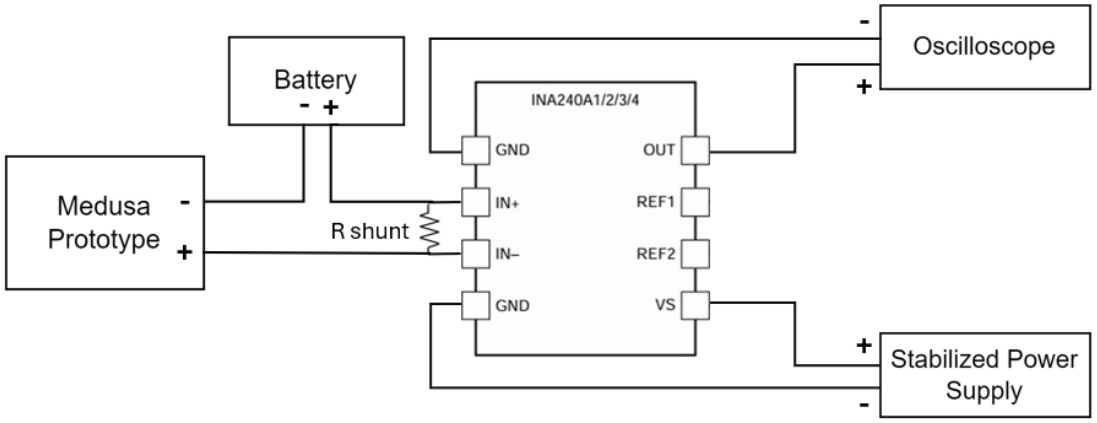

Figure 7.2. Current absorption evaluation setup, image adapted from [50].

The current absorption of the MCU was assessed using Texas Instrument's 20 V/V gain INA240 EVB [50], with the setup illustrated in Figure 7.2. The board amplifies the voltage drop across the shunt resistor (10 Ω), previously soldered across the *IN+* and *IN-* pads. The positive pole of the battery was connected to *IN+*, whereas the *IN-* pin was linked to the Prototype's power supply positive terminal. The negative poles of the battery and the prototype's power supply were connected directly. The EVB was powered with a stabilized power supply set at an output voltage of 5 V (with a current limit of 0.1 A), enabling accurate reading of an incoming current with dynamics up to 50 mA (far exceeding the expected values). REF1 and REF2 pads were left floating to set the voltage reference to GND. The voltage output was then connected to an Oscilloscope to display and save the acquired signal. To obtain the current values the read voltages were divided by $200\,\frac{\mathrm{V}}{\mathrm{V}} \cdot \Omega$ (gain * R shunt). the MCU current consumption was evaluated for the following operating modes:

- **Advertising Mode**: The MCU actively broadcasts the device's presence every 500 ms, by periodically sending out signals that announce its availability for connection.
- **Connection Mode**: The MCU establishes a connection with an external BLE device, where both units enter a wait state for data transmission and perform active checks at maximum intervals of 75 ms to confirm ongoing connectivity.

- **ATC Mode**: The MCU awakens from deep sleep every 130 ms to process ATC calculations and schedule notifications for the next connection opportunity.
- **ML Mode**: Similarly, every 130 ms the MCU awakens to process the expressions predictions computed by the ANN, and schedule notifications for the next connection opportunity.
- **ATC + ML Combined Mode**: Every 130 ms, both the ATC values and the ML prediction are processed and then sent as in the previous cases.
- **sEMG Mode**: The MCU digitizes the sEMG signal through the ADC and processes the data every 100 ms, scheduling notifications for the next connection opportunity.

Five acquisitions were carried out for each MCU working condition, setting a temporal resolution of 200 ms per division for the Advertising Mode (to display two periods) and 100 ms for the others. As stated before, the voltage values were divided by $200\,\frac{\mathrm{V}}{\mathrm{V}} \cdot \Omega$. Subsequently, the average current consumption for each operating mode was calculated by averaging the current values from the five windows. To correct the offset introduced by the instrument, an acquisition was made with the MCU turned off, and its average value was subtracted from the others.

Chapter 8

Experimental Results and Discussion

8.1 sEMG signal quality evaluation

Regarding the quality assessment of the acquired sEMG signal, the SNR values obtained for the *Zygomaticus* and *Biceps Brachii* are reported in Table 8.2 and Table 8.1, respectively.

Table 8.1. SNR estimation for 200 V/V gain on *Biceps Brachii*.

Gain	**SNR (dB)**	
	30 % MCV Contraction	**70 % MCV Contraction**
x1 - 200 V/V	23.5 ± 2.8	39.3 ± 1.3

Table 8.2. Summary of the SNR values obtained on *Zygomaticus* for all the available gain values.

Gain	**SNR (dB)**	
	Medium Contraction	**Intense Contraction**
x1 - 200 V/V	11.6 ± 3.9	23.8 ± 2.5
x2 - 400 V/V	9.40 ± 2.0	29.2 ± 1.7
x4 - 800 V/V	10.7 ± 3.0	33.5 ± 1.7
x6 - 1200 V/V	18.4 ± 1.2	34.3 ± 0.9
x8 - 1600 V/V	8.20 ± 6.0	31.5 ± 2.0

It is primarily observed that the values for the face, as expected, are lower and more variable than those obtained for the *Biceps Brachii*, for the reasons discussed in Section 4.1.1. Nevertheless, the values obtained are more than sufficient to prove the good quality of the acquired signal and are superior to those shown in Table 4.2, demonstrating that the chosen combination of IED and electrode diameter for the active probes was appropriate. The SNR obtained for the *Biceps Brachii* confirms this result when compared to the values shown in Figure 4.4.

8.2 Classifier performance

The performance of the classifier in discriminating the 11 expressions was tested on 7 subjects as described in the previous section. The final confusion matrix obtained by merging all the sessions performed by the subjects is shown in Figure 8.1.

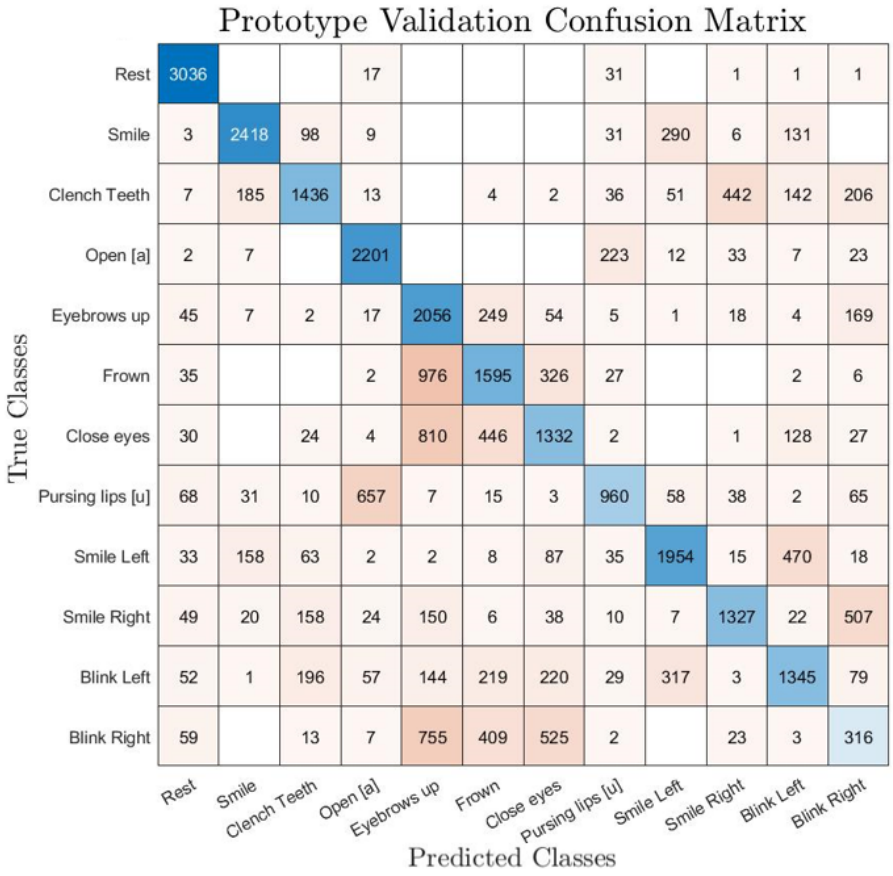

Figure 8.1. Confusion matrix obtain testing the classifier on 7 subjects.

Table 8.3 represents the computed metrics introduced in Section 1.5.2:

Table 8.3. Evaluation metrics computed for all the subjects.

	Evaluation metrics (%)			
Expression	Accuracy	Precision	Recall	F1-score
Rest	98.62	88.80	98.35	93.33
Smile	96.88	85.53	80.98	83.19
Clench teeth	94.73	71.80	56.89	63.48
Open jaw [a]	96.44	73.12	87.76	79.78
Raise eyebrows	89.11	41.96	78.26	54.63
Frown	91.29	54.05	53.72	53.89
Close eyes	91.30	51.49	47.51	49.42
Purse lips [u]	95.58	69.02	50.16	58.09
Smile left	94.81	72.64	68.68	70.61
Smile right	94.99	69.59	57.25	62.82
Blink left	92.89	59.59	50.53	54.69
Blink right	90.76	22.30	14.96	17.91
Avg.	93.95	63.32	62.09	61.82

The results depicted in Figure 8.1 and Table 8.3 indicate a generally high average classification accuracy for the rest state and the 11 facial expressions. However, the Precision, Recall, and F1-score show lower performance.

In particular, the higher results are obtained for "Smile", "Smile Left", "Clench Teeth", and "Open Jaw". On the other hand, "Right Blink", "Closed Eyes", and "Raised Eyebrows" were more difficult to classify.

When analyzing the potential causes of misclassification, it is important to compare the muscle activations deemed physiological for each expression, detailed in Table 1.1, and the dataset used for the ANN training, cited in [48] and shown in Figure 2.12. The main classification errors, as observed from Figure 8.1, concern the following expressions:

- "Frown" and "Closed Eyes": The trained ANN distinguishes these mainly by the activation of the *Frontalis* muscle. Physiologically, closing the eyes primarily involves the *Orbicularis Oculi, Retractor Bulbi, and Levator Palpebrae Superioris* muscles, which are not captured as inputs. Only with exaggerated movement, minor contributions from the *Frontalis, Zygomatic*, and *Corrugator Supercilii* muscles are detected. For accurate classification of eye closure, an exaggerated and unnatural motion is required, as demonstrated by the survey results.

- "Open Jaw [a]" and "Pursing Lips [u]": In the trained ANN, these two movements differ only in the level of activation of the *Digastric* muscle. While the "Open Jaw [a]" primarily involves this muscle, the contribution of the *Digastric* muscle is secondary to that of the *Orbicularis Oris* in "Pursing Lips [u]".

- "Blink" and "Side Smile": As previously discussed, signals from the muscles primarily involved in eye and eyelid movements are not captured. Consequently, activation of one side of the face due to a "Blink" is often interpreted by the ANN as a "Smile" on that side. Correct classification of "Left Blinks" requires an exaggerated expression, including a frown; "Right Blinks" require an unnatural activation of the *Masseter* muscle, which is not typically involved in this movement.

In addition, misclassifications of raised eyebrows and frowning are noted in some subjects, possibly due to cross-talk between the *Frontalis* and *Corrugator Supercilii* muscles. As shown in Figure 8.1, indeed, these muscles partially overlap.

The survey results also highlight general difficulties in performing "Closed Eyes" and "Blink", as well as specific challenges that some individuals have with "Clench Teeth" and "Side Smiles", thereby reducing overall performance in these categories.

Moreover, on Subject 1, who has light facial hair, classification performance in many classes was reduced due to noise picked up by the electrode placed on the *Digastric* muscle, causing false activation.

For Subject 4, many misclassifications were generated by noise under the electrode on the *Frontalis*. This could be due to the subject having a low forehead, making it more challenging to adhere the tape due to the presence of hair and closely set eyebrows, or because of pronounced expression lines in that area, which may have caused slight lifting of the electrode during testing.

Lastly, it is crucial to highlight that, contrary to more recent studies on sEMG-based FER that employ a number of differential electrode pairs equal to or exceeding the number of classes to be discriminated, this network was trained using only 5 inputs against 12 classes to be discriminated. This aspect indeed justifies the need for subjects to perform exaggerated expressions, as greater electrode redundancy would allow not only for the discrimination of subtler expressions but also enhance classification performance in individuals with activation patterns that deviate from the norm. This is essential, given that facial expression execution inherently shows greater variability than movements involving other body parts, due to the activation of numerous overlapping small muscles, as can be seen in Figure 1.3.

Considering all the discussed limitations, the results obtained are nonetheless satisfactory, indicating that the signals acquired by the new prototype are of sufficient quality to achieve high classification accuracies.

8.3 Mechanical support wearability

The evaluation of the headset's wearability was conducted through a form given at the end of the test performed on subjects, as illustrated in the previous chapter. All subjects involved in the test, who had quite variable head sizes, reported that the headset fit well, without slipping or being too tight throughout the test (1 hour and 30 minutes). Additionally, they commented on the overall weight of the device (178 g), and all subjects found it to be satisfactory. Wires and adhesive tape didn't cause any discomfort.

8.4 Current absorption evaluation

In Table 8.4, the current consumptions for the different possible operating states of the MCU are presented.

Table 8.4. MCU current absorption averaged over 5 acquired windows of 5 s each, for different operating modes.

	Advertising	Connection	ATC	ML	ATC and ML	sEMG
Avg. Current Absorption (mA)	0.488	0.505	0.646	0.675	0.816	1.2230

The values are notably low, which enables a LiPo battery of 175 mAh to last for over 140 hours during sEMG acquisition, which is the most power-intensive operation. Estimated battery life allows for extended use suitable for future applications, avoiding interruptions for battery recharging. The following images (Fig 8.2, 8.3, 8.4, 8.5, 8.6, 8.7), instead, provide a visualization of current consumption over time, offering deeper insight into the operation of the MCU. The higher peaks correspond to the sending of notifications, every 130 ms for the ATC and ML modes and every 100 ms for the sEMG mode. In the combined ATC + ML mode, it can be seen (Figure 8.6) that two notifications are sent separately, the first for the ATC values and the second for the ML prediction. The smaller peaks before the notifications are sent represent the writing of the characteristics. Finally, in the sEMG mode, a higher current consumption is observed between the peaks, which is due to the digitization of the sEMG values performed by the ADC.

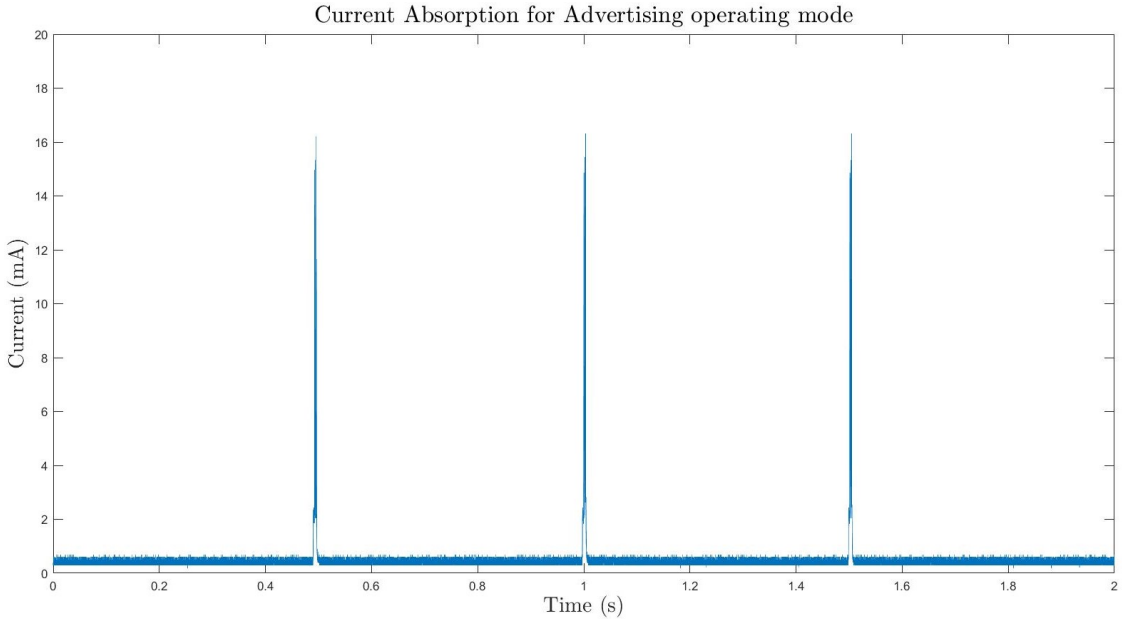

Figure 8.2. Current absorption of the MCU in advertising mode.

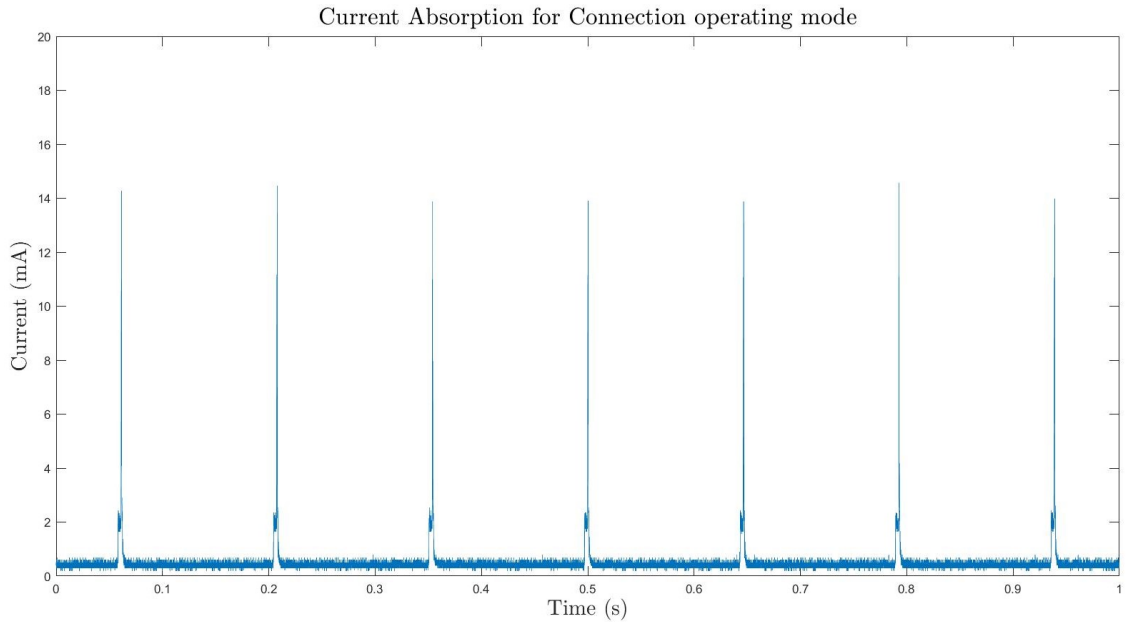

Figure 8.3. Current absorption of the MCU in connection mode.

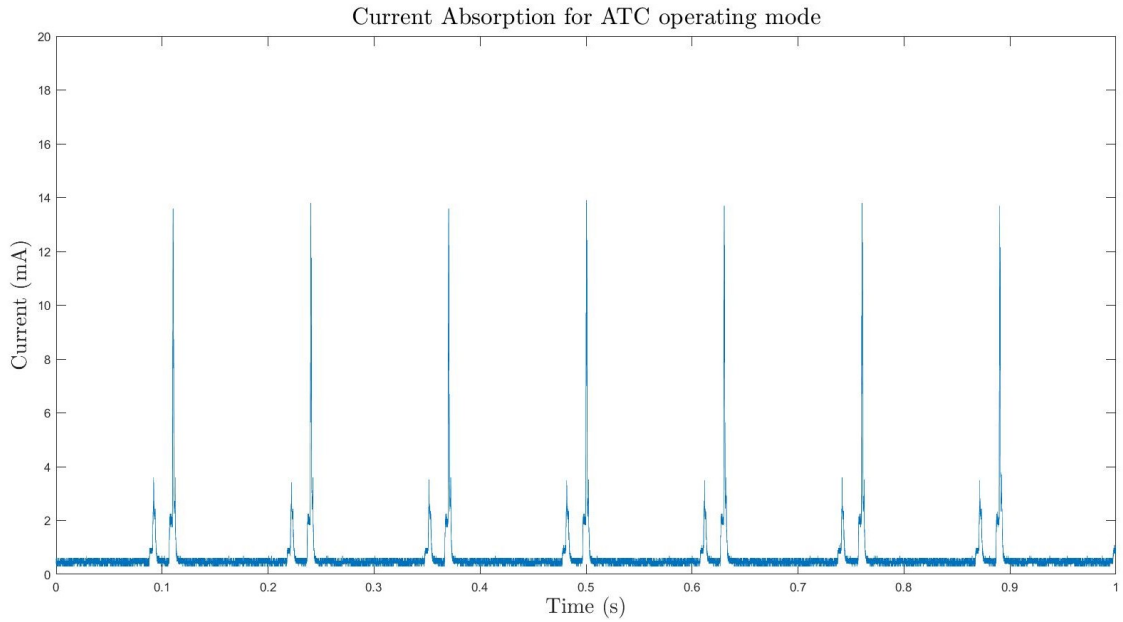

Figure 8.4. Current absorption of the MCU in ATC mode.

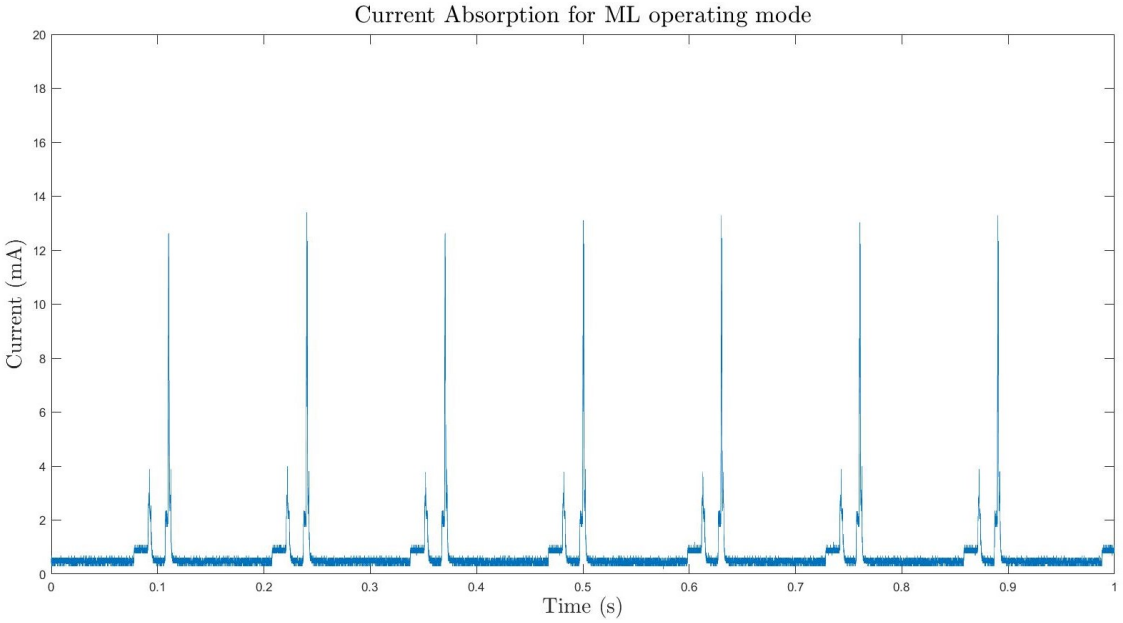

Figure 8.5. Current absorption of the MCU in ML mode.

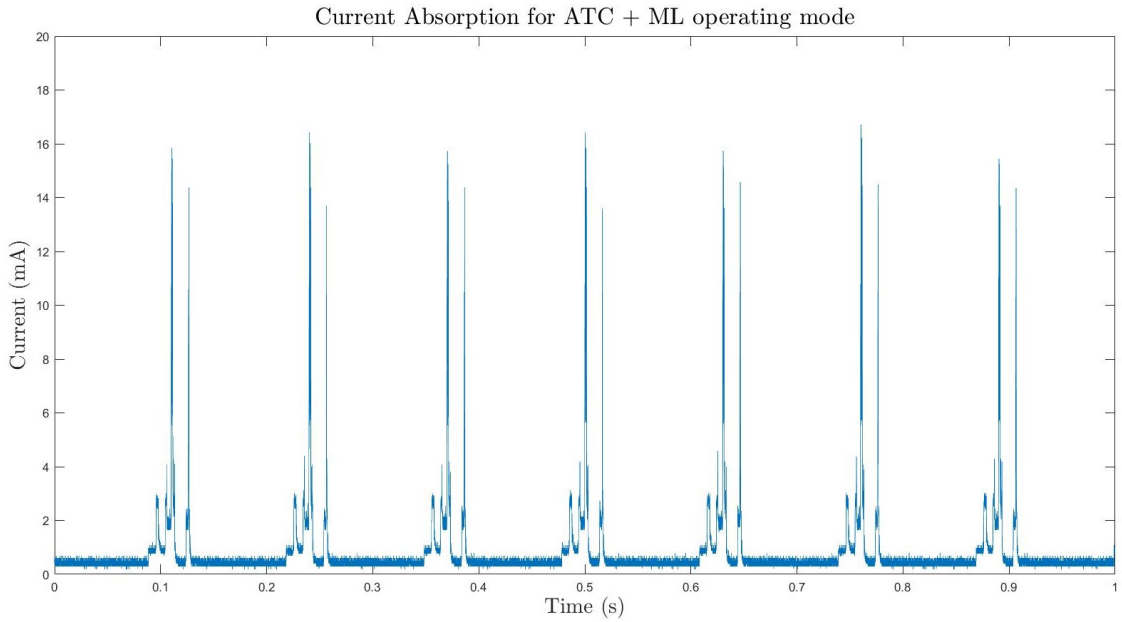

Figure 8.6. Current absorption of the MCU in ATC and ML mode.

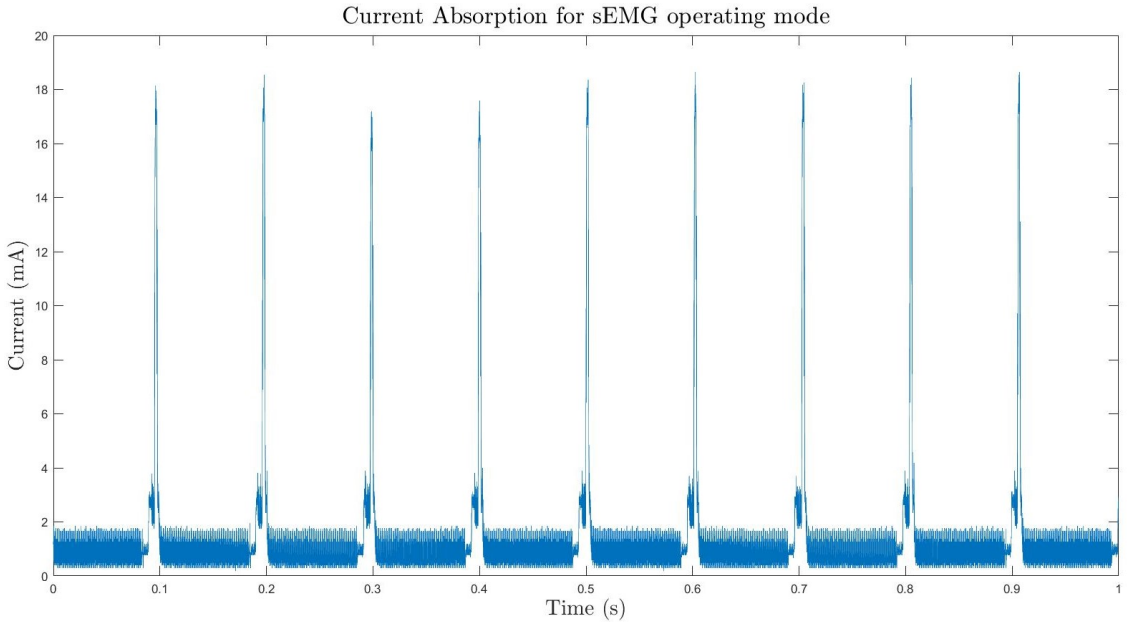

Figure 8.7. Current absorption of the MCU in sEMG mode.

Chapter 9

Conclusions and Future Perspectives

This thesis project presented a wearable prototype for real-time FER using surface ElectroMyoGraphic (sEMG) signals collected from facial and neck muscles. The system represents an advancement over a previous prototype developed by the research team, inheriting its Artificial Neural Network (ANN)-based classifier. The algorithm features an event-based feature extraction method, employing the Averaged Threshold Crossing (ATC) technique on the signals acquired from the 5 selected muscles. An initial phase of signal acquisition and processing led to the adoption of active probes with Gold-plated electrodes, which provide first-stage signal conditioning directly at the sEMG recording point. This phase was followed by the development of two Printed Circuit Boards (PCBs), one for the active probes mentioned earlier, and the other for a main board, which incorporates additional signal conditioning, power management, communication circuits, as well as Flash memory, and an Inertial Measurement Unit (IMU). These components were integrated into a wearable mechanical support, designed and 3D printed to provide comfort and adaptability for various users. The project then culminated in refining the firmware and software to enhance usability, allowing users to view sEMG signals, ATC values, and expression predictions. Testing the prototype's performance involved new acquisitions, which showed an average SNR of over 25 dB for intense facial contractions, indicating the system's ability to capture high-quality signals. The system was then tested on 7 healthy subjects, achieving an average prediction accuracy of 94%, with recall, precision, and f1-score values just above 60%. These outcomes demonstrate the system's potential for effective FER, while also highlighting the need, as discussed in a previous chapter, for network retraining focused on a specific application. The mechanical support successfully fulfilled the established criteria for functionality and wearability, while the firmware and software enhancements enabled a user-friendly interaction with the system. Further tests

on current absorption resulted in a maximum consumption of 1.2 mA for sEMG acquisition, and values at or below 0.8 mA for other operational modes. These values enable the device to achieve a battery life of over 140 hours, ensuring its portability. These results underscore the great potential of the developed device for various applications, which are presented below and refined by the input of the subjects who had the opportunity to test the prototype.

With the visualization of the ATC parameter over five channels and the acquisition of a high-quality sEMG signal, this tool suggests good potential for diagnostic applications. Furthermore, the system could be used in rehabilitative applications, which aim to enhance the ability to perform facial expressions and fundamental actions such as chewing and deglutition. This is particularly valuable since various conditions may compromise these capabilities, leading to significant social and functional challenges. In this application field, the device is ready for use in biofeedback, which enables patients to enhance their physical well-being by learning to regulate bodily functions, such as facial movements, through real-time feedback (visualization of ATC values). Moreover, FER paves the way for implementing a serious game for rehabilitation, blending therapy with engaging gameplay to enhance users' physical, mental, and emotional health. Ultimately, another potential application lies in developing a Human Machine Interface, potentially aiding actions performed by tetraplegic individuals.

Appendix

Evaluation metrics computed for all the subjects

	Evaluation metrics (%) - subject 1			
Expression	Accuracy	Precision	Recall	F1-score
Rest	98.65	96.11	89.57	92.72
Smile	93.60	68.81	62.47	65.49
Clench teeth	92.21	71.51	29.49	41.76
Open jaw [a]	96.68	7.35	27.78	11.63
Raise eyebrows	83.49	32.75	76.37	45.85
Frown	91.70	56.28	75.49	64.49
Close eyes	88.91	42.02	33.26	37.13
Purse lips [u]	98.10	68.58	90.64	78.09
Smile left	90.55	62.82	10.82	18.46
Smile right	86.99	20.06	18.49	19.24
Blink left	81.79	0.00	0.00	0.00
Blink right	83.14	13.97	14.48	14.22
Avg.	90.48	45.02	44.07	40.76

	Evaluation metrics (%) - subject 2			
Expression	Accuracy	Precision	Recall	F1-score
Rest	99.75	97.77	99.55	98.65
Smile	98.34	85.60	97.91	91.34
Clench teeth	93.55	0.00	0.00	0.00
Open jaw [a]	96.67	75.00	96.19	84.28
Raise eyebrows	96.34	72.64	94.13	82.00
Frown	93.36	64.20	59.91	61.98
Close eyes	90.70	48.94	85.85	62.34
Purse lips [u]	93.59	49.44	14.33	22.22
Smile left	95.24	67.25	94.61	78.62
Smile right	92.93	70.21	24.94	36.80
Blink left	96.30	92.23	64.92	76.20
Blink right	86.29	9.75	6.19	7.57
Avg.	94.42	61.09	61.54	58.50

	Evaluation metrics (%) - subject 3			
Expression	Accuracy	Precision	Recall	F1-score
Rest	100.00	100.00	100.00	100.00
Smile	99.03	91.28	98.39	94.70
Clench teeth	98.73	100.00	82.79	90.58
Open jaw [a]	97.08	75.09	99.54	85.60
Raise eyebrows	92.53	54.59	95.48	69.47
Frown	90.56	44.01	28.74	34.77
Close eyes	93.06	57.41	78.01	66.14
Purse lips [u]	97.08	98.14	52.67	68.55
Smile left	98.01	85.71	92.63	89.04
Smile right	99.15	90.85	100.00	95.21
Blink left	98.31	97.28	81.11	88.46
Blink right	93.34	94.87	25.46	40.14
Avg.	96.41	82.44	77.90	76.89

	Evaluation metrics (%) - subject 4			
Expression	Accuracy	Precision	Recall	F1-score
Rest	99.91	99.32	99.77	99.55
Smile	93.44	67.56	54.05	60.05
Clench teeth	90.40	47.76	37.47	41.99
Open jaw [a]	93.29	53.17	46.18	49.43
Raise eyebrows	68.51	7.78	81.63	14.20
Frown	90.46	57.89	2.49	4.77
Close eyes	89.90	30.00	1.99	3.73
Purse lips [u]	91.38	43.03	50.73	46.57
Smile left	91.79	55.39	84.07	66.78
Smile right	96.26	82.11	68.90	74.93
Blink left	89.79	1.38	0.61	0.84
Blink right	89.05	11.76	1.77	3.08
Avg.	90.35	46.43	44.14	38.83

	Evaluation metrics (%) - subject 5			
Expression	Accuracy	Precision	Recall	F1-score
Rest	99.94	99.32	100.00	99.66
Smile	99.03	95.64	94.13	94.88
Clench teeth	94.23	77.13	39.30	52.06
Open jaw [a]	97.08	77.64	98.22	86.73
Raise eyebrows	95.81	70.11	99.33	82.20
Frown	92.44	63.57	55.24	59.11
Close eyes	95.31	80.37	67.94	73.63
Purse lips [u]	97.02	94.08	52.57	67.45
Smile left	99.37	95.81	97.75	96.77
Smile right	97.47	84.41	77.81	80.98
Blink left	96.80	79.34	90.65	84.62
Blink right	94.79	3.61	6.90	4.74
Avg.	96.61	76.75	73.32	73.57

	Evaluation metrics (%) - subject 6			
Expression	Accuracy	Precision	Recall	F1-score
Rest	98.63	88.51	99.55	93.70
Smile	98.79	91.92	95.90	93.87
Clench teeth	98.14	85.54	95.00	90.02
Open jaw [a]	96.94	80.00	92.02	85.59
Raise eyebrows	95.62	91.74	53.91	67.91
Frown	86.89	41.73	75.40	53.73
Close eyes	86.06	27.40	27.60	27.50
Purse lips [u]	96.06	83.16	54.33	65.73
Smile left	93.20	72.73	14.86	24.68
Smile right	94.90	53.74	51.48	52.59
Blink left	94.53	71.05	75.70	73.30
Blink right	95.71	29.52	21.83	25.10
Avg.	94.62	68.09	63.13	62.81

	Evaluation metrics (%) - subject 7			
Expression	Accuracy	Precision	Recall	F1-score
Rest	91.50	60.00	100.00	75.00
Smile	95.46	96.86	62.37	75.88
Clench teeth	96.15	77.75	90.40	83.60
Open jaw [a]	97.60	89.90	88.75	89.32
Raise eyebrows	91.93	73.23	39.08	50.97
Frown	93.98	61.21	88.64	72.41
Close eyes	95.83	76.56	27.53	40.50
Purse lips [u]	95.95	75.15	55.61	63.92
Smile left	95.20	70.51	74.83	72.61
Smile right	97.57	94.92	58.95	72.73
Blink left	91.93	4.31	2.89	3.46
Blink right	94.07	30.53	58.97	40.23
Avg.	94.76	67.58	62.33	61.72

Apollux v023 schematics

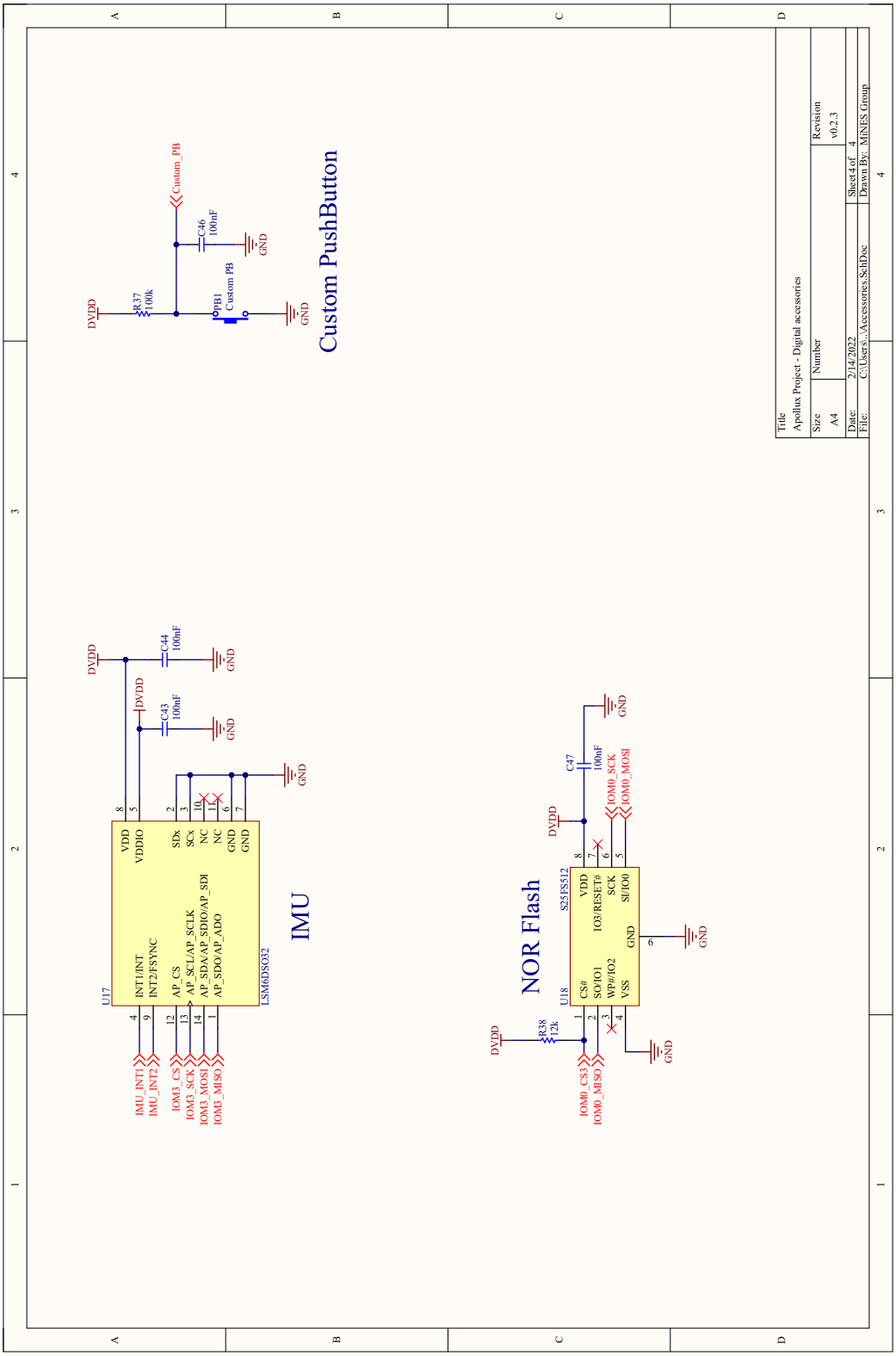

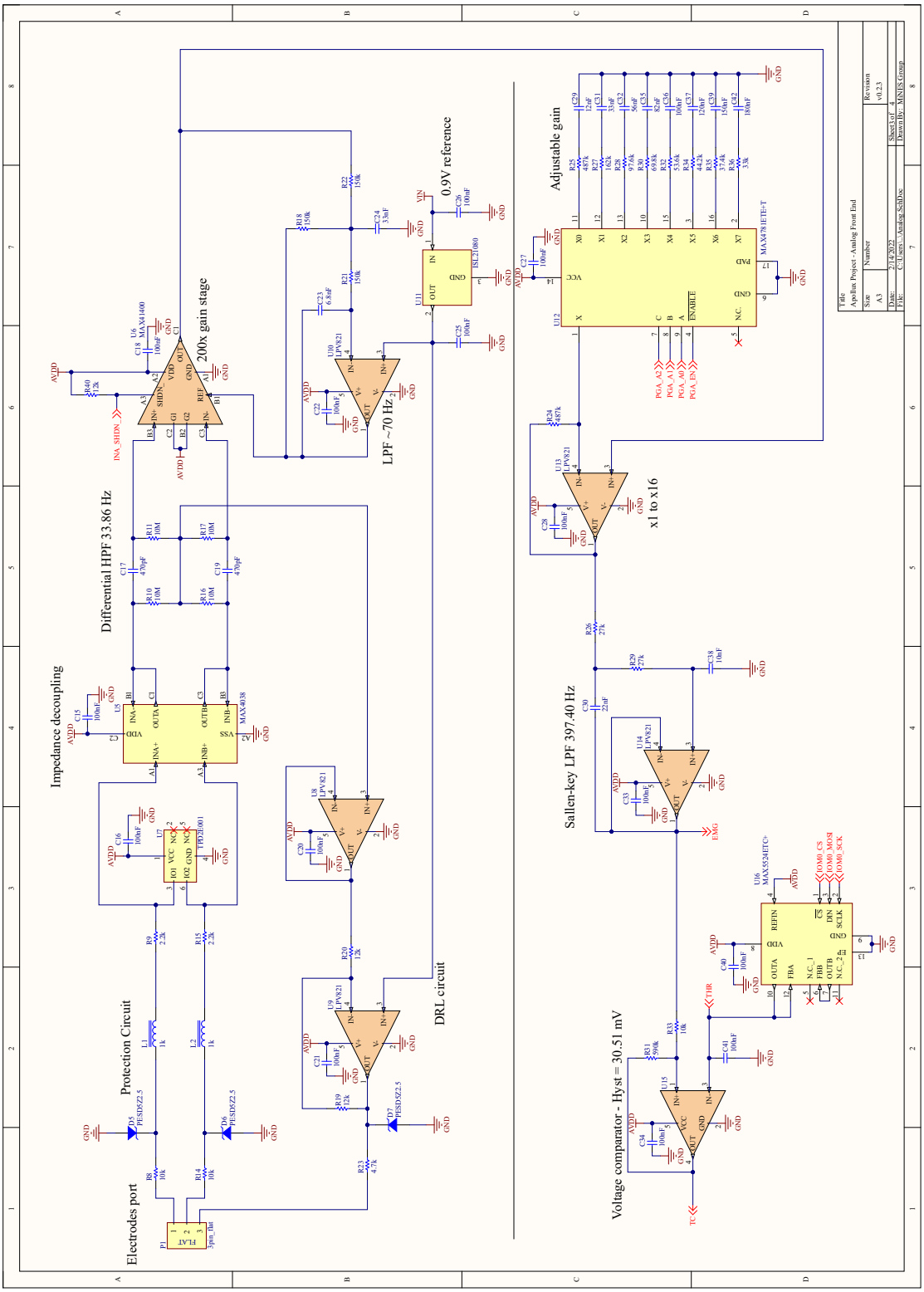
Impedance decoupling
Differential HPF 33.86 Hz
200x gain stage
LPF ~70 Hz
0.9V reference
Adjustable gain
x1 to x16
Sallen-key LPF 397.40 Hz
Protection Circuit
DRL circuit
Voltage comparator - Hyst = 30.51 mV
Electrodes port
Title
Apollux Project - Analog Front End
Size
A3
Number
Revision
v0.2.3
Date:
2/14/2022
File:
C:\Users\...\Analog.SchDoc
Sheet 3 of 4
Drawn By:
MNHS Group

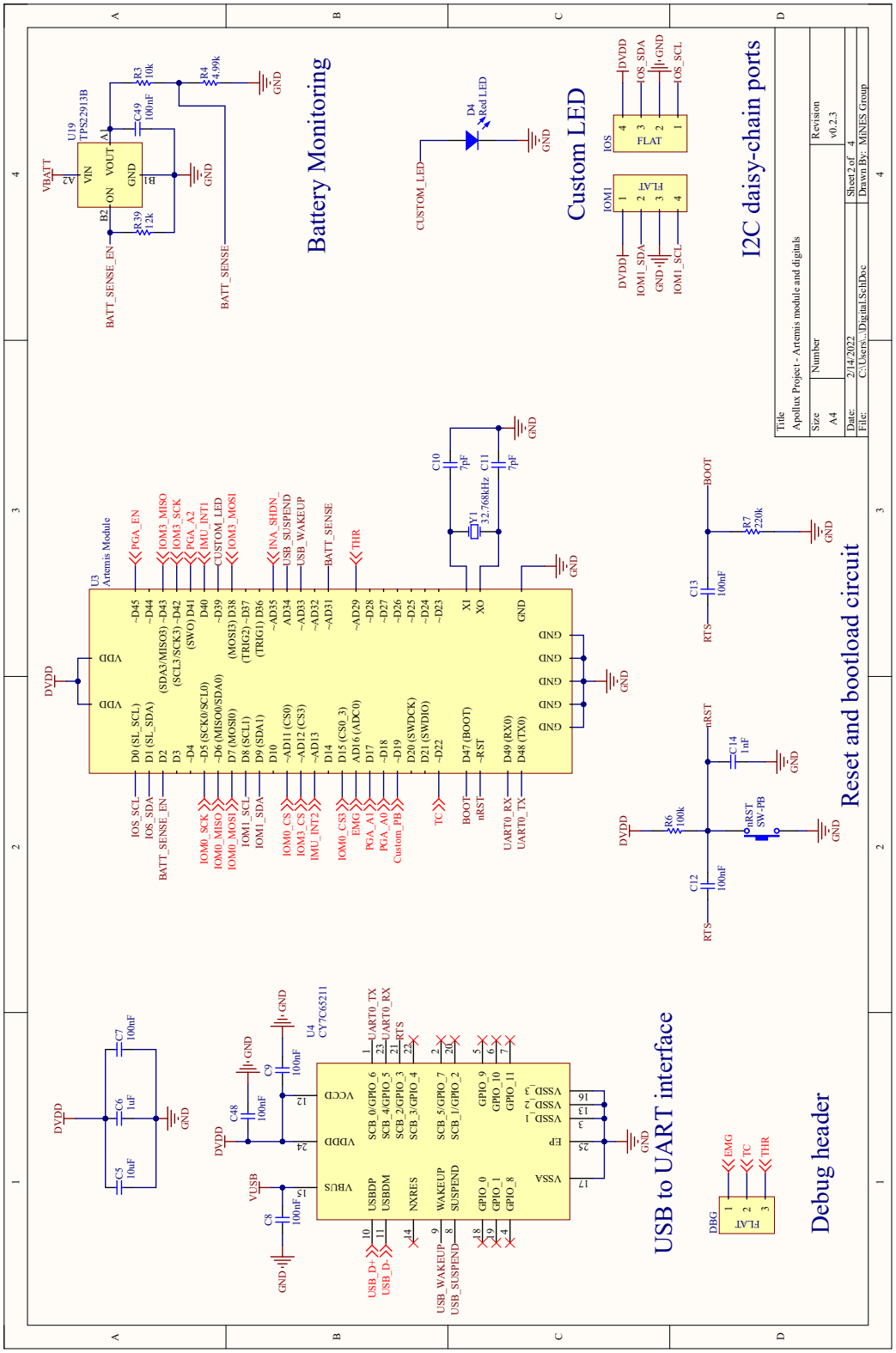
Battery Monitoring
Custom LED
I2C daisy-chain ports
Reset and bootload circuit
USB to UART interface
Debug header
Apollux Project - Artemis module and digitals
Artemis Module
TPS22913B
CY7C65211
Red LED
32.768kHz
SW-PB
FLAT
Size
A4
Number
Revision
v0.2.3
Date:
2/14/2022
Sheet 2 of 4
File:
C:\Users...\Digital.SchDoc
Drawn By:
MINES Group

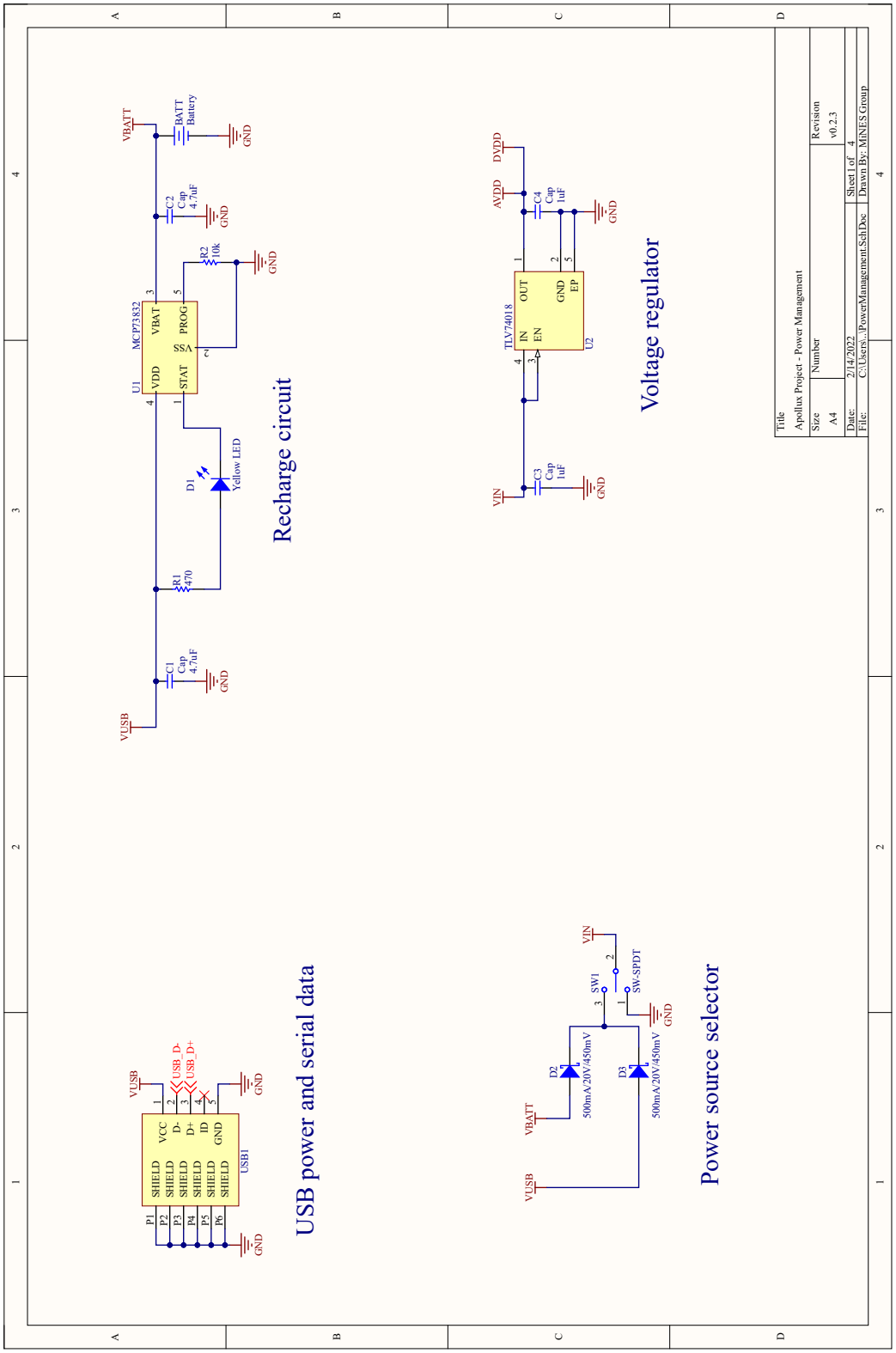
Recharge circuit
Voltage regulator
USB power and serial data
Power source selector
MCP73832
TLV74018
Yellow LED
500mA/20V/450mV
SW-SPDT
Title
Apollux Project - Power Management
Size
A4
Number
Revision
v0.2.3
Date:
2/14/2022
Sheet 1 of 4
File:
C:\Users\...\PowerManagement.SchDoc
Drawn By: MiNES Group

Active Probes schematics

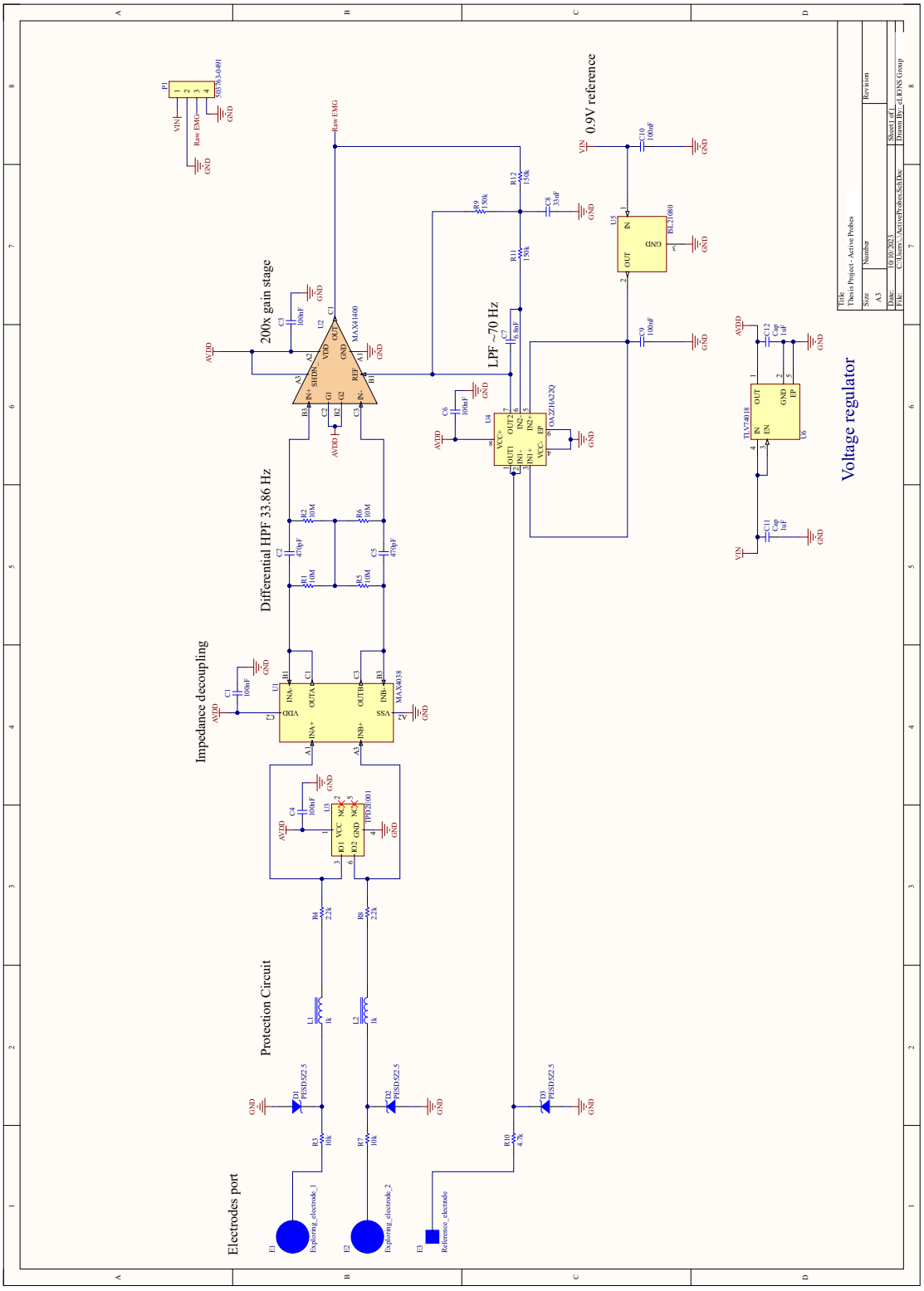

Main PCB schematics

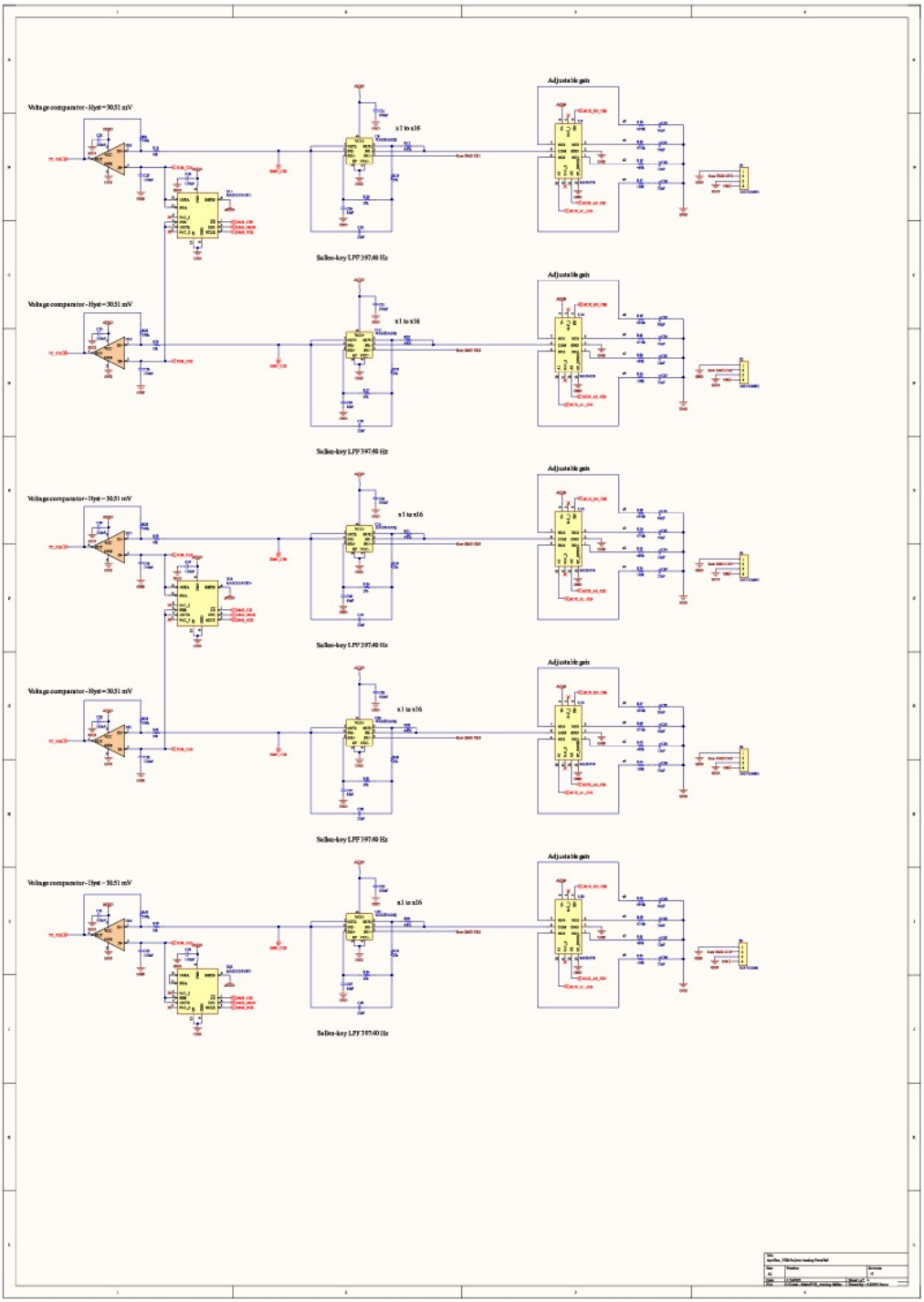

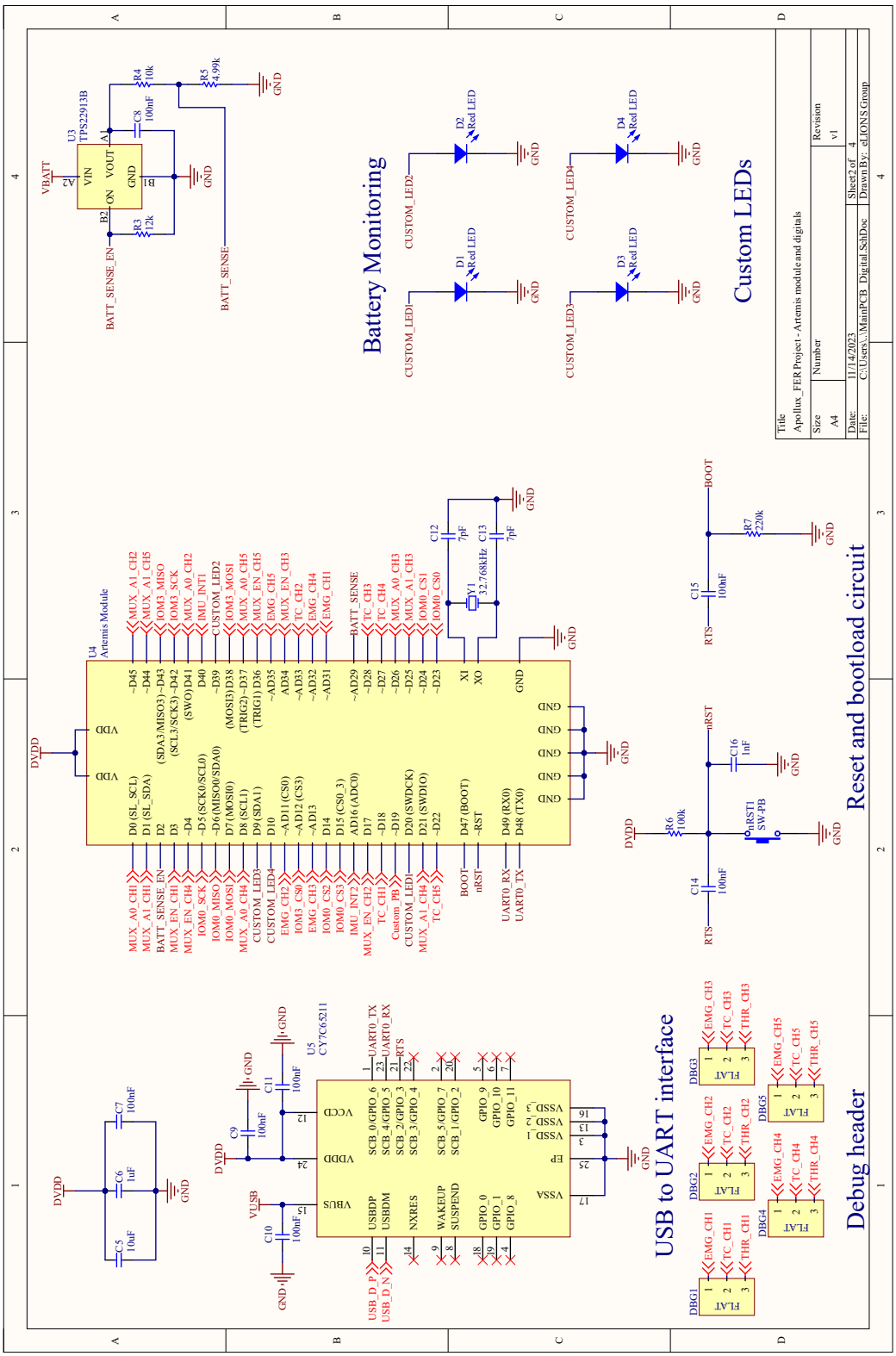
Battery Monitoring
Custom LEDs
Reset and bootload circuit
USB to UART interface
Debug header
U4
Artemis Module
U5
CY7C65211
U3
TPS22913B
Y1
32.768kHz
Title
Apollux_FER Project - Artemis module and digitals
Size
A4
Number
Revision
v1
Date:
11/14/2023
File:
C:\Users\...\MainPCB_Digital.SchDoc
Sheet 2 of 4
Drawn By:
eLIONS Group

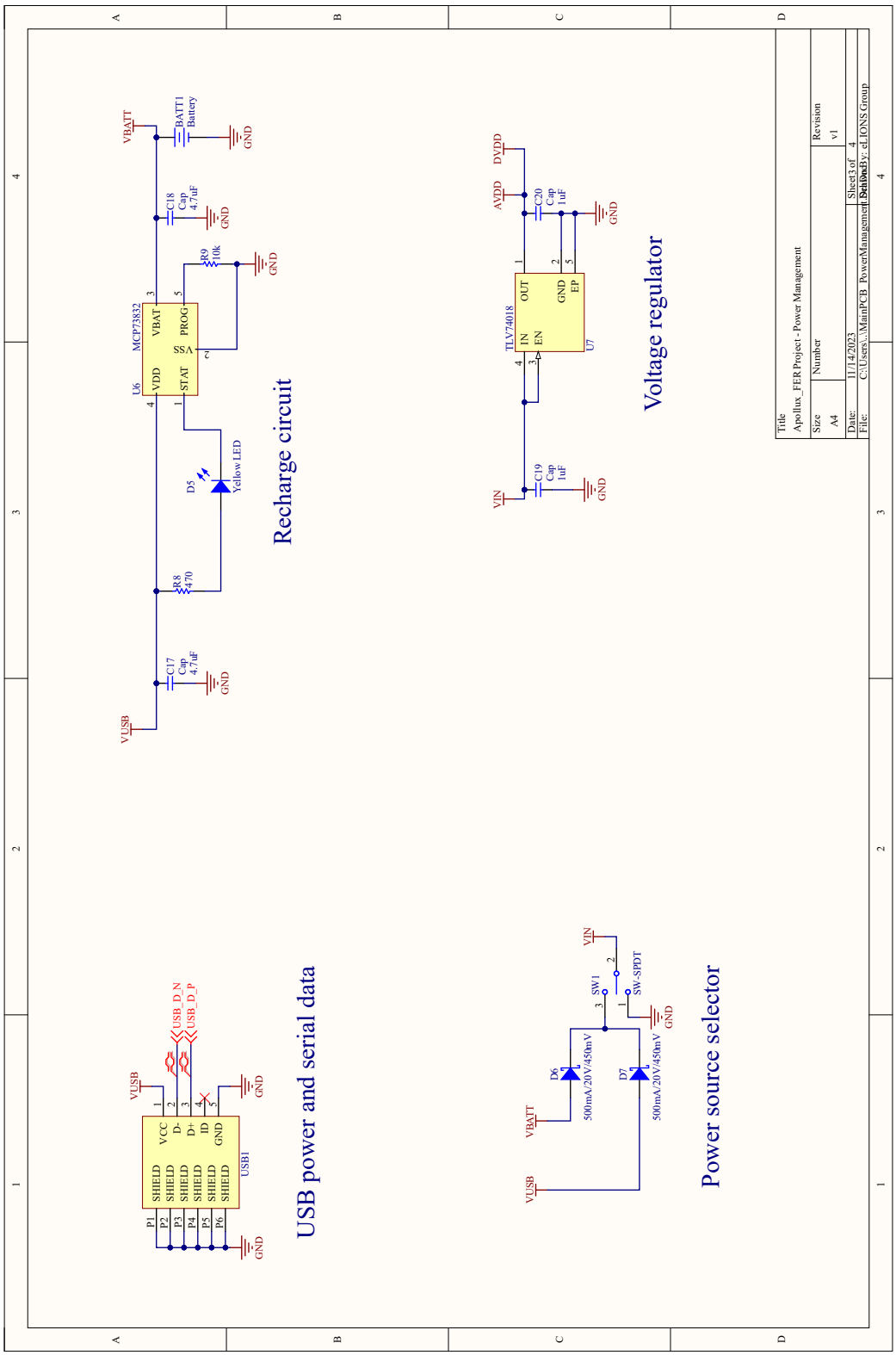
USB power and serial data
Recharge circuit
Voltage regulator
Power source selector
Apollux_FER Project - Power Management
Size: A4
Number
Revision: v1
Date: 11/14/2023
Sheet 3 of 4
File: C:\Users\...\MainPCB_PowerManagement.SchDoc
Drawn By: el_IONS Group
VBATT
BATT1
Battery
C18
Cap
4.7uF
R9
10k
U6
MCP73832
VBAT
PROG
VDD
STAT
D5
Yellow LED
R8
470
C17
VUSB
USB1
SHIELD
VCC
D-
D+
ID
GND
USB_D_N
USB_D_P
AVDD
DVDD
C20
1uF
TLV74018
IN
EN
OUT
EP
U7
VIN
C19
SW1
SW-SPDT
D6
D7
500mA/20V/450mV
GND

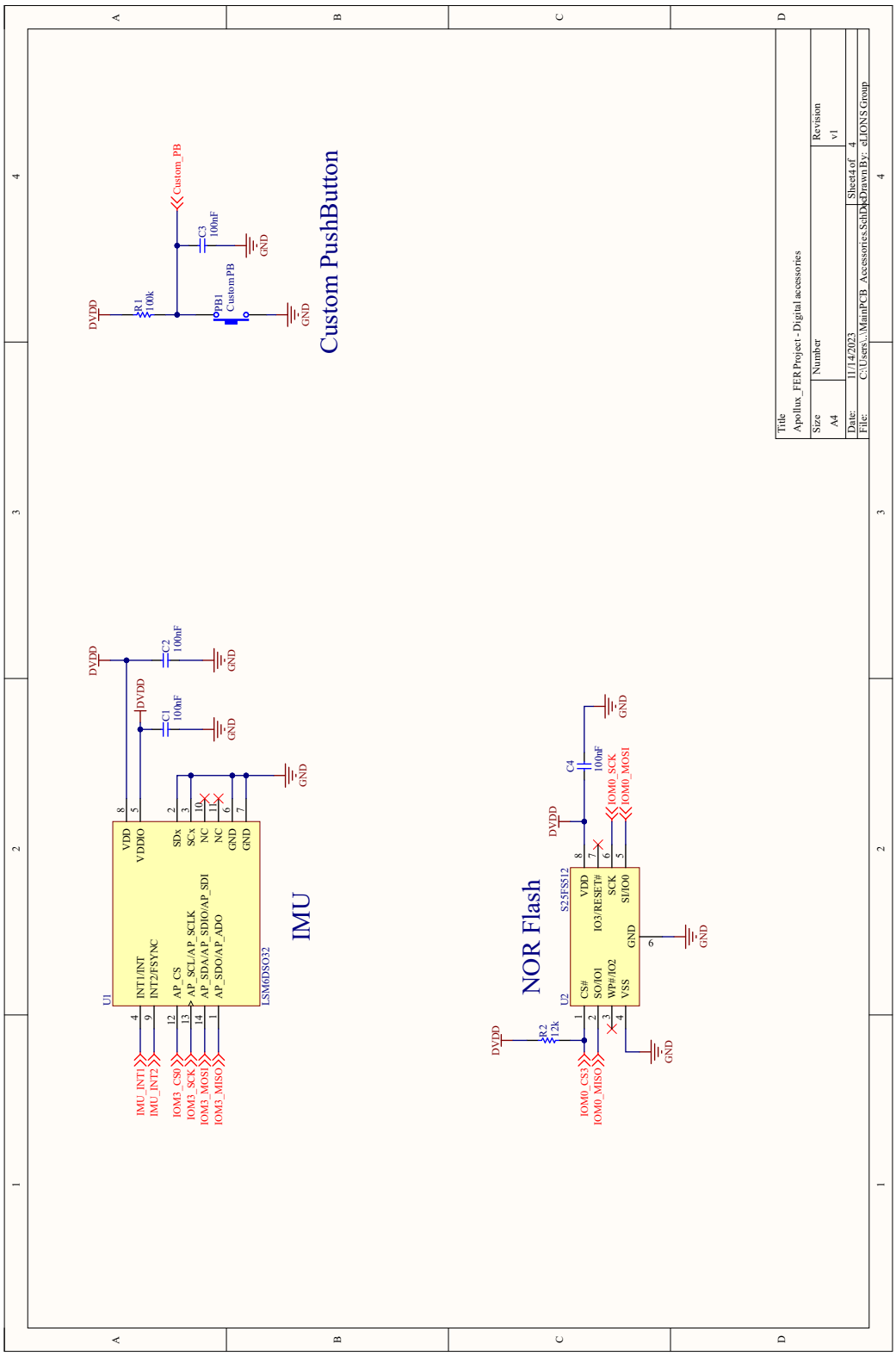
Custom PushButton
IMU
NOR Flash
Custom_PB
DVDD
GND
R1
100k
C3
100nF
PB1
CustomPB
C2
C1
U1
LSM6DSO32
INT1/INT
INT2/FSYNC
VDD
VDDIO
AP_CS
AP_SCL/AP_SCLK
AP_SDA/AP_SDIO/AP_SDI
AP_SDO/AP_ADO
SDx
SCx
NC
IMU_INT1
IMU_INT2
IOM3_CS0
IOM3_SCK
IOM3_MOSI
IOM3_MISO
U2
S25FS512
CS#
SO/IO1
WP#/IO2
VSS
IO3/RESET#
SCK
SI/IO0
C4
R2
12k
IOM0_SCK
IOM0_MOSI
IOM0_CS3
IOM0_MISO
Title
Apollux_FER Project - Digital accessories
Size
A4
Number
Revision
v1
Date:
11/14/2023
Sheet of
4
File:
C:\Users\..\MainPCB_Accessories.SchDoc
Drawn By:
eLIONS Group

Bibliography

[1] B. Cadot and E.R. Gomes. “Skeletal Muscle”. In: Encyclopedia of Cell Biology. Edition by Ralph A. Bradshaw and Philip D. Stahl. Waltham: Academic Press, 2016, pp. 677–682. ISBN: 9780123947963.

[2] Muscle Anatomy. *Encyclopædia Britannica*. Available at: `https://www.britannica.com/science/muscle`. Last visited on September 23, 2023.

[3] G.J. Tortora and B.H. Derrickson. "Principles of Anatomy", 14th Edition. Wiley, 2013. ISBN: 9781118808856.

[4] M. Schuenke, E. Schulte, and U. Schumacher. "General Anatomy and Musculoskeletal System". THIEME Atlas of Anatomy Series. Thieme, 2011. ISBN: 9781604062939.

[5] Sliding Filament Model of Muscle Contraction. Available at: `https://it.m.wikibooks.org/wiki/File:1006_Sliding_Filament_Model_of_Muscle_Contraction.jpg`. Last visited on October 4, 2023.

[6] Facial muscles. Available at: `https://mobilephysiotherapyclinic.net/facial-muscles-anatomy-function/`. Last visited on September 22, 2023.

[7] F.P Kendall, E. K. McCreary, P. G. Provance, M. M. Rodgers, W. A. Romani, "I Muscoli: funzioni e test con postura e dolore". Verduci Editore, 2006. ISBN: 8876207244.

[8] R. Merletti and D. Farina, "Surface electromyography: physiology, engineering and applications". in IEEE Press series in biomedical engineering. Piscataway, NJ: Hoboken, New Jersey: IEEE Press; Wiley, 2016, pp. 54-91. ISBN: 9781118987025.

[9] S.K. Gollapudi, J.J. Michael, and M. Chandra. “Striated Muscle Dynamics”. In: Reference Module in Biomedical Sciences. Elsevier, 2014. ISBN: 9780128012383.

[10] J.C. Calderón, P.Bolaños, C.Caputo. "The excitation–contraction coupling mechanism in skeletal muscle". Biophysical Reviews, 2014. doi: 10.1007/s12551-013-0135-x.

[11] B. Zebian, W. Lam, and R. Aggarwal. "One Stop Doc Musculoskeletal System". One Stop Doc. CRC Press, 2005, pp. 7-8. ISBN: 9781444114386.

[12] Facial Muscles - Anatomy, Origin, Insertion, Function, Exercise. Available at: `https://mobilephysiotherapyclinic.net/facial-muscles-anatomy-function/`. Last visited on September 23, 2023.

[13] Human Muscle System. *Encyclopædia Britannica*. Available at: `https://www.britannica.com/science/human-muscle-system`. Last visited on September 23, 2023.

[14] S. Rampichini, T. M. Vieira, P. Castiglioni, and G. Merati, "Complexity Analysis of Surface Electromyography for Assessing the Myoelectric Manifestation of Muscle Fatigue: A Review," Entropy, vol. 22, no. 5, 2020. doi: 10.3390/e22050529.

[15] L. Shaw and S. Bagha, "ONLINE EMG SIGNAL ANALYSIS FOR DIAGNOSIS OF NEUROMUSCULAR DISEASES BY USING PCA AND PNN," International Journal of Engineering Science and Technology, vol. 4, 2012. doi: 10.1251/bpo115.

[16] C. J. De Luca. "Surface Electromyography: Detection and Recording".DelSys Incorporated, 2012, pp. 1-10.

[17] D. Staudenmann, K. Roeleveld, D. F. Stegeman, and J.H. van Dieën. "Methodological aspects of sEMG recordings for force estimation – a tutorial and review". Journal of Electromyography and Kinesiology, 2010. doi: 10.1016/j.jelekin.2009.08.005.

[18] M. Crepaldi, M. Paleari, A. Bonanno, A. Sanginario, P. Ariano, D. H. Tran, and D.emarchi. " quasi-digital radio system for muscle force transmission based on event-driven ir-uwb". 2012 IEEE Biomedical Circuits and Systems Conference (BioCAS), 2012, pp. 116–119. doi: 10.1109/BioCAS.2012.6418406.

[19] F. Rossi, P. Motto Ros, R. Motto Rosales, and D. Demarchi, "Embedded Bio-Mimetic System for Functional Electrical Stimulation Controlled by Event-Driven sEMG," Sensors, vol. 20, no. 5, 2020, p. 1535. doi: 10.3390/s20051535.

[20] A. Shahshahani, M. Shahshahani, P. Motto Ros, A. Bonanno, M. Crepaldi, M. Martina, D. Demarchi, and G. Masera. " all-digital spike-based ultra-low-power ir-uwb dynamic average threshold crossing scheme for muscle force wireless transmission". 2015 Design, Automation Test in Europe Conference Exhibition (DATE), 2015, pp. 1479-1484. ISBN: 9783981537048.

[21] A. Searle and L. Kirkup, "A direct comparison of wet, dry and insulating bioelectric recording electrodes," Physiol. Meas., vol. 21, no. 2, 2000, pp. 271–283. doi: 10.1088/0967-3334/21/2/307.

[22] C. M. Vidhya, Y. Maithani, and J. P. Singh, "Recent Advances and Challenges in Textile Electrodes for Wearable Biopotential Signal Monitoring: A Comprehensive Review," Biosensors, vol. 13, no. 7, Jun. 2023, p. 679. doi: 10.3390/bios13070679.

[23] T. W. Beck et al., “A comparison of monopolar and bipolar recording techniques for examining the patterns of responses for electromyographic amplitude and mean power frequency versus isometric torque for the vastus lateralis muscle,” Journal of Neuroscience Methods, vol. 166, no. 2, Nov. 2007, pp. 159–167. doi: 10.1016/j.jneumeth.2007.07.002.

[24] G. L. Cerone and M. Gazzoni, “A wireless, minaturized multi-channel sEMG acquisition system for use in dynamic tasks,”. 2017 IEEE Biomedical Circuits and Systems Conference (BioCAS), Torino, Italy: IEEE, Oct. 2017, pp. 1–4. doi: 10.1109/BIOCAS.2017.8325129.

[25] H. Song, Y. Park, H. Kim, and H. Ko, “Fully Integrated Biopotential Acquisition Analog Front-End IC,” Sensors, vol. 15, no. 10, Sep. 2015, pp. 25139–25156. doi: 10.3390/s151025139.

[26] J. Sehgal and M. Kumar, “Biopotential Acquisition Systems: A Comparative Analysis,”. 2022 International Conference on Smart Generation Computing, Communication and Networking (SMART GENCON), Bangalore, India: IEEE, Dec. 2022, pp. 1–6. doi: 10.1109/SMARTGENCON56628.2022.10083829.

[27] J. W. Clark, M. R. Neuman, A. J. Nimunkar, W. H. Olson, R. A. Peura, F. P. Primiano, M. P. Siedband, J. G. Webster, L. A. Wheeler, "Medical Instrumentation: application and design", Wiley, fifth edition, 2020, pp. 268-283. ISBN: 9781119457336.

[28] The Instrumentation Amplifier. *All About Circuits*. Available at: `https://www.allaboutcircuits.com/textbook/semiconductors/chpt-8/the-instrumentation-amplifier/`. Last visited on September 21, 2023.

[29] F. Rossi, A. Mongardi, P. Motto Ros, M. R. Roch, M. Martina, and D. Demarchi, “Tutorial: A Versatile Bio-Inspired System for Processing and Transmission of Muscular Information,” IEEE Sensors J., vol. 21, no. 20, Oct. 2021, pp. 22285–22303. doi: 10.1109/JSEN.2021.3103608.

[30] S. Rathnapriya and V. Manikandan, "Remaining Useful Life Prediction of Analog Circuit Using Improved Unscented Particle Filter," Journal of Electronic Testing, vol. 36, 2020. doi: 10.1007/s10836-020-05870-9.

[31] The Bluetooth Low Energy Protocol Stack: Understanding the layers. Available at: `https://novelbits.io/bluetooth-low-energy-protocol-stack-layers/`. Last visited on May 10, 2023.

[32] Generic Attribute Profile (GATT). Available at: `https://software-dl.ti.com/lprf/sdg-latest/html/ble-stack-3.x/gatt.html`. Last visited on November 24, 2023.

[33] Introduction to Bluetooth Low Energy. Available at: `https://lpccs-docs.renesas.com/UM-B-119_DA14585-DA14531_SW_Platform_Reference/Introduction/Introduction.html`. Last visited on February 20, 2024.

[34] What is Linear Discriminant Analysis (LDA)? *IBM*. Available at: `https:`

//www.ibm.com/topics/linear-discriminant-analysis. Last visited on February 20, 2024.

[35] Deep Convolutional Neural Networks: a guide. Available at: https://www.run.ai/guides/deep-learning-for-computer-vision/deep-convolutional-neural-networks. Last visited on February 20, 2024.

[36] What is Random Forest? *IBM*. Available at: https://www.ibm.com/topics/random-forest. Last visited on February 20, 2024.

[37] O. A. Montesinos López, A. Montesinos López, and J. Crossa, "Fundamentals of Artificial Neural Networks and Deep Learning," in Multivariate Statistical Machine Learning Methods for Genomic Prediction, Cham: Springer International Publishing, 2022, pp. 379–425. doi: 10.1007/978-3-030-89010-0.

[38] F. Bre, J. M. Gimenez, and V. D. Fachinotti, "Prediction of wind pressure coefficients on building surfaces using artificial neural networks," Energy and Buildings, vol. 158, Jan. 2018, pp. 1429–1441. doi: 10.1016/j.enbuild.2017.11.045.

[39] S. Li and W. Deng, "Deep Facial Expression Recognition: A Survey," IEEE Trans. Affective Comput., vol. 13, no. 3, Jul. 2022, pp. 1195–1215. doi: 10.1109/TAFFC.2020.2981446.

[40] H. S. Cha, S. J. Choi and C. H. Im, "Real-Time Recognition of Facial Expressions Using Facial Electromyograms Recorded Around the Eyes for Social Virtual Reality Applications," in IEEE Access, vol. 8, 2020, pp. 62065-62075. doi: 10.1002/2014GC005287.

[41] H. S. Cha and C. H. Im, "Performance enhancement of facial electromyogram-based facial-expression recognition for social virtual reality applications using linear discriminant analysis adaptation," Virtual Reality, vol. 26, no. 1, Mar. 2022, pp. 385–398. doi: 10.1007/s10055-021-00575-6.

[42] H. S. Cha and C. H. Im, "Improvement of robustness against electrode shift for facial electromyogram-based facial expression recognition using domain adaptation in VR-based metaverse applications," Virtual Reality, vol. 27, no. 3, Sep. 2023, pp. 1685–1696. doi: 10.1007/s10055-023-00761-8.

[43] I. Kiprijanovska et al., "Facial Expression Recognition using Facial Mask with EMG Sensors". doi:10.1038/s41598-023-43135-5.

[44] M. Zhuang et al., "Highly Robust and Wearable Facial Expression Recognition via Deep-Learning-Assisted, Soft Epidermal Electronics," Research, vol. 2021/9759601, Jan. 2021. doi: 10.34133/2021/9759601.

[45] S. H. Yeon et al., "Flexible Dry Electrodes for sEMG Acquisition within Lower Extremity Prosthetic Sockets," in 2020 8th IEEE RAS/EMBS International Conference for Biomedical Robotics and Biomechatronics (BioRob), New York City, NY, USA: IEEE, Nov. 2020, pp. 1088–1095. doi: 10.1109/BioRob49111.2020.9224338.

[46] A. Mongardi et al., “Hand Gestures Recognition for Human-Machine Interfaces: A Low-Power Bio-Inspired Armband,” IEEE Trans. Biomed. Circuits Syst., vol. 16, no. 6, Dec. 2022, pp. 1348–1365. doi: 10.1109/TBCAS.2022.3211424.

[47] A. Mongardi, P. Motto Ros, F. Rossi, M. R. Roch, M. Martina, and D. Demarchi, “A Low-Power Embedded System for Real-Time sEMG based Event-Driven Gesture Recognition,” in 2019 26th IEEE International Conference on Electronics, Circuits and Systems (ICECS), Genoa, Italy: IEEE, Nov. 2019, pp. 65–68. doi: 10.1109/ICECS46596.2019.8964944.

[48] L. Giannantoni, "Integration and Validation of an Event-driven sEMG-based Embedded Prototype fo rReal-time Facial Expression Recognition". M.Sc. Thesis, Department of Mechanical and Aerospace Engineering, Politecnico di Torino, Torino, 2023.

[49] How to Improve EMG Signal Quality: The Signal to Noise Ratio (SNR). *Delsys*. Available at: `https://delsys.com/emgworks/signal-quality-monitor/improve/`. Last visited on September 18, 2023.

[50] INA240EVM: High or Low Side Current Sensing Amplifier for PWM Applications Evaluation Module. Available at: `https://www.ti.com/tool/INA240EVM`. Last visited on March 6, 2024.